Characterization of the terminal region RNAs of the West Nile virus genome and their interaction with the small isoform of 2' 5'-oligoadenylate synthetases (OAS)

by

Soumya R. Deo

A thesis submitted to Faculty of Graduate Studies of

The University of Manitoba

in partial fulfillment of the requirements of the degree of

DOCTOR OF PHILOSOPHY

Department of Chemistry

Faculty of Science

University of Manitoba

Winnipeg, Manitoba, Canada

Abstract

2'-5'-oligoadenylate synthetases (OAS) are interferon-stimulated proteins that act in the innate immune response to viral infection. Upon binding to viral double-stranded RNAs, OAS enzymes produce 2'-5'-linked oligoadenylates that stimulate RNase L and ultimately slow viral propagation. Studies have linked mutations in the *OAS1* gene to increased susceptibility to West Nile virus (WNV) infection, highlighting the importance of the OAS1 enzyme. Here I report that the 5'-terminal region (5'-TR) of the WNV genome, comprising both the 5'-untranslated region (5'-UTR) and initial coding region, is capable of OAS1 activation *in vitro*. This region contains three RNA stem loops (SLI, SLII, and SLIII), whose relative contribution to OAS1 binding affinity and activation were investigated using electrophoretic mobility shift assays and enzyme kinetics experiments. Stem loop I (SLI) is dispensable for maximum OAS1 activation, as a construct containing only SLII and SLIII was capable of enzymatic activation. Mutations to the RNA binding site of OAS1 confirmed the specificity of the interaction. Solution conformations of both the 5'-TR RNA of WNV and OAS1 were then elucidated using small-angle x-ray scattering. I also report that the 3' terminal region (3'-TR) is able to mediate specific interaction with and activation of OAS1. Binding and kinetic experiments identified a specific stem loop within the 3'-TR that is sufficient for activation of the enzyme. The solution confirmation of the 3'-terminal region was determined by small angle X-ray scattering, and computational models suggest a conformationally restrained structure comprised of a helix and short stem loop. Structural investigation of the 3'-

TR in complex with OAS1 is also presented. Finally, we show that genome cyclization by base pairing between the 5'- and 3'-TRs, a required step for replication, is not sufficient to protect WNV from OAS1 recognition. The purity, monodispersity and homogeneity of all samples subjected to SAXS analysis were evaluated using dynamic light scattering and/or analytical ultra-centrifuge. These data provide a framework for understanding recognition of the highly structured terminal regions of a flaviviral genome by an innate immune enzyme.

Acknowledgements

I take this opportunity to convey my gratitude and heartfelt thanks to people without whose support the research presented in this thesis wouldn't have been possible. I would like to express my sincere gratitude to my graduate program supervisor Dr. Sean McKenna. Dr. McKenna always encouraged me to perform better and be an effective researcher. The time he invested and the valuable suggestions he gave to make this thesis attain the current form are greatly appreciated. His guidance and the wonderful research environment of the McKenna lab, for which I must thank all the past and present lab members, resulted in several publications leading to successful fellowship and awards.

Although all the past and present lab members of the McKenna lab were great to work with, I would like to particularly thank Edis Dzananovic, Dr. Evan Booy, Dr. Trushar Patel and Hui Meng for their help, guidance and successful collaboration work. Hui Meng helped me with various experiments during my early days as a PhD student. Edis and Trushar helped me with different aspects of SAXS experiments including data collection and analysis. With all the experiments I performed with mammalian cells, Evan provided me with lots of inputs in terms of training and suggestions.

I also would like to thank my advisory committee, Dr. Brian Mark, Dr. Mazdak Khajehpour and Dr. Mario Bieringer for the advice and guidance they have provided over the years. I really appreciate their effort and time spent in reviewing my thesis and offering guidance and suggestions. I also thank Dr. Mazdak Khajehpour for his advice in developing a quantitative enzyme assay for OAS1 activation. I would also like to thank Dr. Eric Jan, the external examiner for reviewing my thesis.

My work has been supported by a Discovery grant from Natural Sciences and Engineering Research Council of Canada (NSERC). I was also funded by fellowships/scholarships from Faculty of Graduate Studies, U of Manitoba (University of Manitoba Graduate Fellowship), Faculty of Science (Faculty of Science award) and Govt. of Manitoba (Manitoba Graduate Scholarship).

Finally, I would like to thank my family for their love and encouragement over the course of my career.

Dedication

I want to dedicate this thesis

to my son Krishang who has given me immense joy of being a father,

to my wife Sasmita, my parents, my brother and sister for their love and support.

Table of Contents

List of Tables

List of Figures

List of copyrighted materials

Licensed content publisher: Plos.org

Licensed content publication: Plos One (open access)

Licensed content title: Activation of 2′ 5′-Oligoadenylate Synthetase by Stem Loops at the 5′-End of the West Nile Virus Genome

Published: March 20, 2014 DOI: 10.1371/journal.pone.0092545

Sections where the licensed materials can be found: 3.2.1.1, 3.2.1.2, 3.2.1.3, 3.2.1.4, 3.2.1.5, 3.2.1.6 and 3.2.2

Licensed content publisher: Elsevier

Licensed content publication: Journal of Structural Biology

Licensed content title: Characterization of the termini of the West Nile virus genome and their interactions with the small isoform of the 2' 5'-oligoadenylate synthetase family

Published: 2015 May;190(2):236-49. doi: 10.1016/j.jsb.2015.04.005. Epub 2015 Apr 11

Sections where the licensed materials can be found: 1.2.5.2, 4.2.1.1, 4.2.1.2, 4.2.1.3, 4.2.1.4, 4.2.1.5, 4.2.1.6 and 4.2.2

As per the copyright holders (Elsevier): 1. “Authors can include their articles in full or in part in a thesis or dissertation for non-commercial purposes”.

2. “Theses and dissertations which contain embedded published journal articles as part of the formal submission can be posted publicly by the awarding institution with DOI links back to the formal publications on ScienceDirect”.

List of Abbreviations

A	adenine
ADAR	adenosine deaminases acting on RNA
AP1	activator protein 1
ATP	adenosine tri-phosphate
bp	base-pair
CS	conserved sequence
DLS	dynamic light scattering
D_{max}	maximum particle dimension
dsRBM	double stranded RNA binding motif
dsRNA	double stranded RNA
E. coli	*Escherichia coli*
eIF-2α	eukaryotic initiation factor 2α
EMSA	electrophoretic mobility shift assay
GTP	guanosine tri-phosphate
IFN	interferon
IFNAR	interferon α/ β receptor
IkB	inhibitor of kB
IRF	interferon regulatory factor
ISG	interferon-stimulated gene
ISG15	interferon-stimulated gene 15
ISGF	interferon stimulatory gene factor
ISRE	interferon stimulated response elements
ITC	isothermal titration calorimetry
JAK/STAT	Janus Kinase/signal transducers and activators of transcription
K_{app}	apparent K_m
Kb	kilo-bases
KEN domain	kinase domain
K_m	Michaelis constant
LGP2	laboratory of genetics and physiology 2

MAVS	mitochondrial antiviral signaling
Mb	mega-bases
MBL	mannose binding lectin
MDA5	melanoma differentiation associated gene 1
MICB	Manitoba institute of cell biology
Mx1	myxovirus resistant protein
MyD88	myeloid differentiation primary response 88
NFkB	nuclear factor kappa-light-chain-enhancer of activated B cells
NOD	nucleotide-binding oligomerization domain
NLR	NOD Like Receptor
NSD	normalized spatial discrepancy
NS protein	non-Structural protein
OAS	2' 5' -oligoadenylate synthetase
OASL	OAS like
ORF	open reading frame
p	phosphate group
PAMP	pathogen associated molecular patterns
PAP	poly A polymerase
PKR	dsRNA-dependent protein kinase
PK domain	protein kinase domain
PPi	pyrophosphate
Poly I:C	polyinosinic-polycytidylic acid
PRR	pattern recognition receptor
RdRp	RNA dependent RNA polymerase
r_G	radius of gyration
r_H	hydrodynamic radius
RIG-I	retinoic acid-inducible gene I
RLR	RIG-I Like Receptor
RNase L	ribonuclease L
SAXS	small angle X-ray scattering
SEC	size exclusion chromatography

SNP	single nucleotide polymorphism
SL	stem-loop or long stem-loop
SS	short stem-loop
ssRNA	single stranded RNA
ssDNA	single stranded DNA
TBK-1	TANK-binding protein kinase 1
TLR	Toll-like receptor
T_m	melting temperature
TNF	tumor necrosis factor
TR	terminal region
TIR	Toll-interleukin-1 receptor
TRIF	TIR-domain containing adaptor inducing interferon (IFN)-β
UAR	upstream initiation AUG region
UTR	untranslated Region

Viruses

DENV	dengue virus
EMCV	encephalomyocarditis virus
HCV	hepatitis C virus
JEV	Japanese encephalitis virus
SV	simian virus
TBEV	tick-borne encephalitis virus
TEV	Tobacco etch virus
WNV	West-Nile virus
YFV	yellow fever virus
XMRV	xenotropic murine leukemia-related virus

CHAPTER 1: INTRODUCTION

1.1 INTRODUCTORY REMARKS

In this thesis, I present my work on 2' 5'-oligoadenylate synthetases (OAS), a family of important innate immune system enzymes. OAS1, the smallest isoform of the OAS family of enzymes, is the focus of my research, as is its antiviral response to West-Nile virus (WNV) infection. A general introduction to antiviral innate immunity will be presented; focusing on the role the interferon (IFN) cascade plays in the process. This will lead into the introduction of cellular viral sensing receptors, to which OAS1 belongs. Details on how OAS enzymes, which play an important role in sensing viral double-stranded RNA (dsRNA), mediate the innate immune response will conclude the introduction.

1.2 INNATE IMMUNITY

The human immune system is composed of numerable, interwoven complex pathways enabling an adequate response against invading pathogens. The immune system can be broadly divided into the innate and the adaptive immune systems. Innate means inborn, and as the name suggests this category of immune system is present and is ready to interact with and mount a response against incoming pathogens [1]. Alternatively, the adaptive immune system has to shape its attack according to antigens present owing to invading pathogens. This results in antibodies being formed specific to the antigens that the host is exposed to [1]. Immune cells responsible for generating antibodies either alter the specificity or are

deleted if they produce autoreactive antibodies that recognize self antigens [2]. OAS1, the focus of this thesis, is a key innate immune response enzyme, which warrants a broader introduction to the process of innate immunity.

Unlike the adaptive immune system that responds by generating antigen specific antibodies, innate immunity is a quick and non-specific response and is the first-line of defense when our body encounters pathogen invasion [3]. It is an evolutionarily conserved mechanism of host defense against infection, evident in lower life forms (including some Arthropods) and predates the adaptive immune system [3]. The co-evolution of host and pathogen over millions of years has resulted in an innate immune system with multiple, intricate pathways entwined to create an effective anti-pathogenic response. In fact, an effective adaptive immune response needs critical input from innate immunity, which demonstrates that these two branches of the immune system are inter-related and inter-dependent [4]. To summarize, the innate immunity takes the center-stage in the fight against pathogens in the initial phase of an infection, which gives the host time to respond with a potent antigen specific adaptive immune response. Many pathogens have very short doubling times that could overwhelm the host cells in the absence of an effective innate immunity.

There are recognition systems in the innate immune response that help to recognize molecules of pathogenic origin and subsequently initiate an adequate response. They can be broadly categorized into the complement system and pattern recognition receptors (PRRs) [5]. The complement system recognizes antigens by utilizing mannose binding lectins (MBL) and Ficolins [5]. The MBL and Ficolins are

lectins (carbohydrate binding proteins); those recognize carbohydrates like mannose, *N*-acetylglucosamine *etc.*, that are part of peptidoglycans found on surfaces of some microbes. The complement system counters the invasion of pathogens indirectly by two ways: binding to them and making them better targets of phagocytosis (opsonization), and chemotactically enhancing the localization of phagocytes at the site of infection and/or complement activation [6]. The direct action of complement system is forming a membrane attack complex on the pathogen leading to the creation of pores or transmembrane channels that compromises the integrity of the cell membrane resulting in lysis of the pathogen [6].

PRRs are so named because they recognize pathogen associated molecular patterns (PAMPs). Most common PAMPs include lipopolysaccharides from gram-negative bacteria, lipoteichoic acid from gram-positive bacteria, double stranded RNA (dsRNA) from viruses, peptidoglycans that are part of bacterial cell wall and glucans from Fungi [5]. The wide variety of PAMPs are recognized by a range of PRRs; these include Toll-like receptors (TLRs), retinoic acid-inducible gene 1 (RIG-I) like receptors (RLRs), nucleotide-binding oligomerization domain (NOD) like receptors (NLRs), the dsRNA-dependent protein kinase (PKR) and OAS [5,7]. The common aspects of PRRs are that they are expressed in a wide range of cell types and their expression is not related to immunological memory and they are vital for the survival of the host [5].

1.2.1 INTERFERON (IFN) CASCADE IN ANTIVIRAL INNATE IMMUNITY

Innate immunity executes its antiviral effect mainly through the IFN cascade. These IFNs are signaling proteins that are named so as they interfere with viral replication [8]. The IFNs are divided into two types: type I and type II IFNs. IFN α and IFN β are the major subclass of type I IFNs and they share significant sequence homology [9]. Initial recognition by PRRs of a small number of PAMPs has the potential to trigger a comprehensive immune response via the IFN cascade [10]. The IFN cascade involves the initial recognition of viral PAMPs, up-regulating IFN production, which

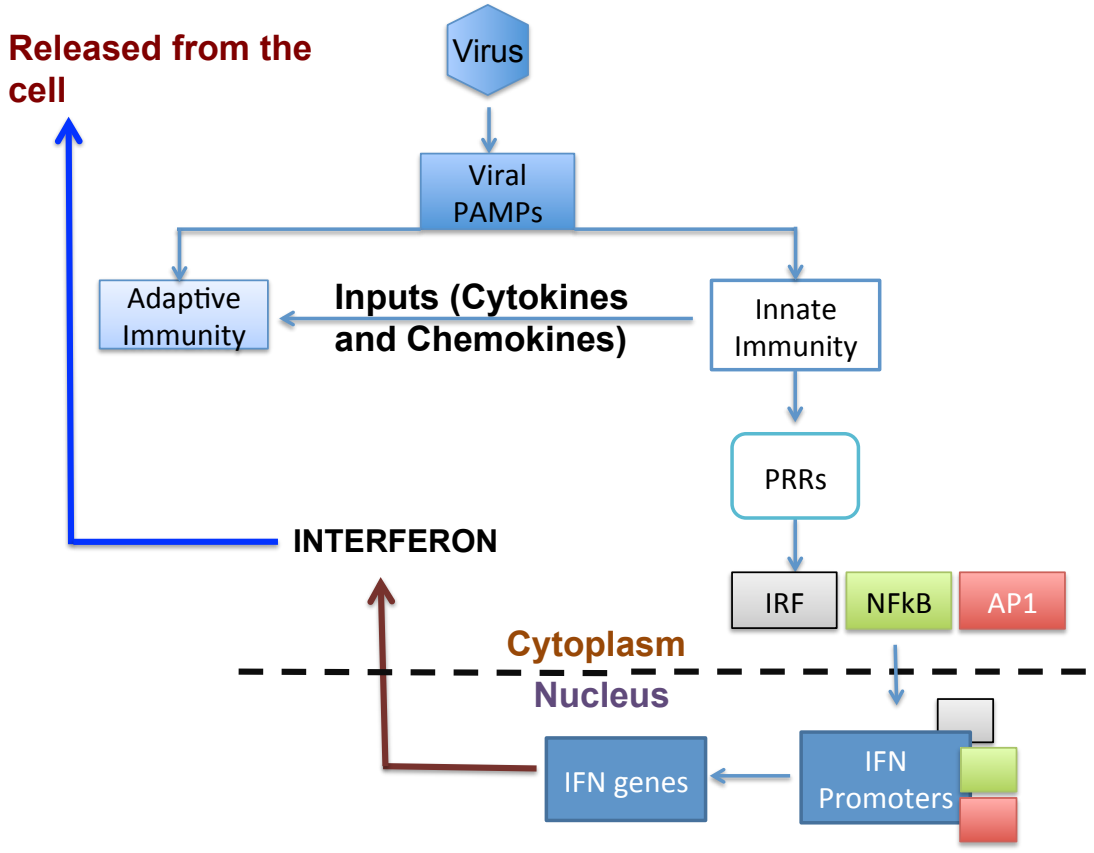

Figure 1.1 Schematic representation of interferon production in response to viral PAMPs. The interferon produced has both an autocrine and paracrine effect on the IFN cascade. Antiviral innate immunity includes the PRRs sensing viral PAMPs and high level of interferon production via activation of complex transcription factors [5,11].

when released initiates downstream antiviral pathways in the neighboring cells for an effective and amplified immune response [10]. IFN induced antiviral response is believed to be evolutionarily conserved in vertebrates only, and the absence of homologous genes to IFN in many invertebrates supports this [12-16]. The interferon cascade is initiated by the PRRs when they bind viral PAMPs leading to downstream signaling pathways. The pattern recognition receptors are conserved in both the invertebrates and the vertebrates [17]. Major downstream IFN response pathways including Janus kinase/signal transducers and activators of transcription (JAK/STAT) are seen in insects including *Drosophila* and *Culex* mosquitoes [18,19]. Focusing on the IFN response in vertebrates here, the most studied sequence of events that results in mounting a successful IFN-mediated innate immune response includes activating phosphorylation, subsequent dimerization, and nuclear translocation of interferon regulatory factor 3 (IRF3) [10]. IRF3, along with nuclear factor kappa-light-chain-enhancer of activated B cells (NFkB) and activator protein 1 (AP-1), recruits multiple transcriptional factors, thereby inducing a high-level interferon β (IFN β) transcription. The NFkB is in an inactive state and could be activated by various stimuli including some PRRs (Toll like receptors), tumor necrosis factor α (TNF- α), interleukin-1β (IL-1β), reactive oxygen species and bacterial lipopolysaccharides [10,20,21]. IFN α production is induced by IFN β [22-

24]. IL-2 and IL-12 produced by the T cells and the large granular lymphocytes (LGL) induce IFN γ production [25].

Figure 1.1 is a schematic representation of the induction of IFN β production [26-31]. Transcription factors that induce IFN β are inactive under basal conditions and have to be converted into active forms. IRF3 is activated by phosphorylation of serine 385 and 386, serine/threonine amino acids between 396 and 405 residues, whereas NFkB needs poly-ubiquitination and subsequent proteasomal degradation of its inhibitor IkB (Inhibitor of kB) [28,32]. These transcription factors eventually effect interferon production. Produced interferon is released from the cells into the extracellular matrix. The mode of action for the interferon is to interact with the IFN α/ β receptor (IFNAR) on the cell surface eventually leading to enhanced transcription of interferon stimulated genes (ISGs) contain interferon stimulated response elements (ISRE) [33]. The interferon released can act upon the cells it was released from (autocrine) or on neighboring cells that it can reach (paracrine) (**Figure 1.2**) [34]. This is materialized through the downstream activating effect of IFN β binding to IFNAR leading to activation of JAK/STAT pathway [35]. The JAK/STAT pathway results in phosphorylation of STAT1 and STAT2 at a conserved C-terminal tyrosine residue and these phosphorylated STATs combine with interferon regulatory factor 9 (IRF9) to form ISGF3, an important regulatory factor for ISGs activation [34,36-38]. These ISGs under the regulation of IFN β induced ISGF3 include the gene that encodes interferon regulatory factor 7 (IRF7), which when expressed binds to the promoter sequence of the IFN α gene thereby triggering the interferon cascade [22-24]. With both IFN α and IFN β executing their

autocrine and paracrine antiviral effect, they stimulate a high-level production of effector proteins encoded by the ISGs [39]. Approximately 900 IFN β induced ISGs including effector proteins are identified using micro-arrays [40]. Some of these antiviral effector proteins are RIG-I, PKR, OAS, adenosine deaminases acting on RNA (ADAR), myxovirus resistant protein

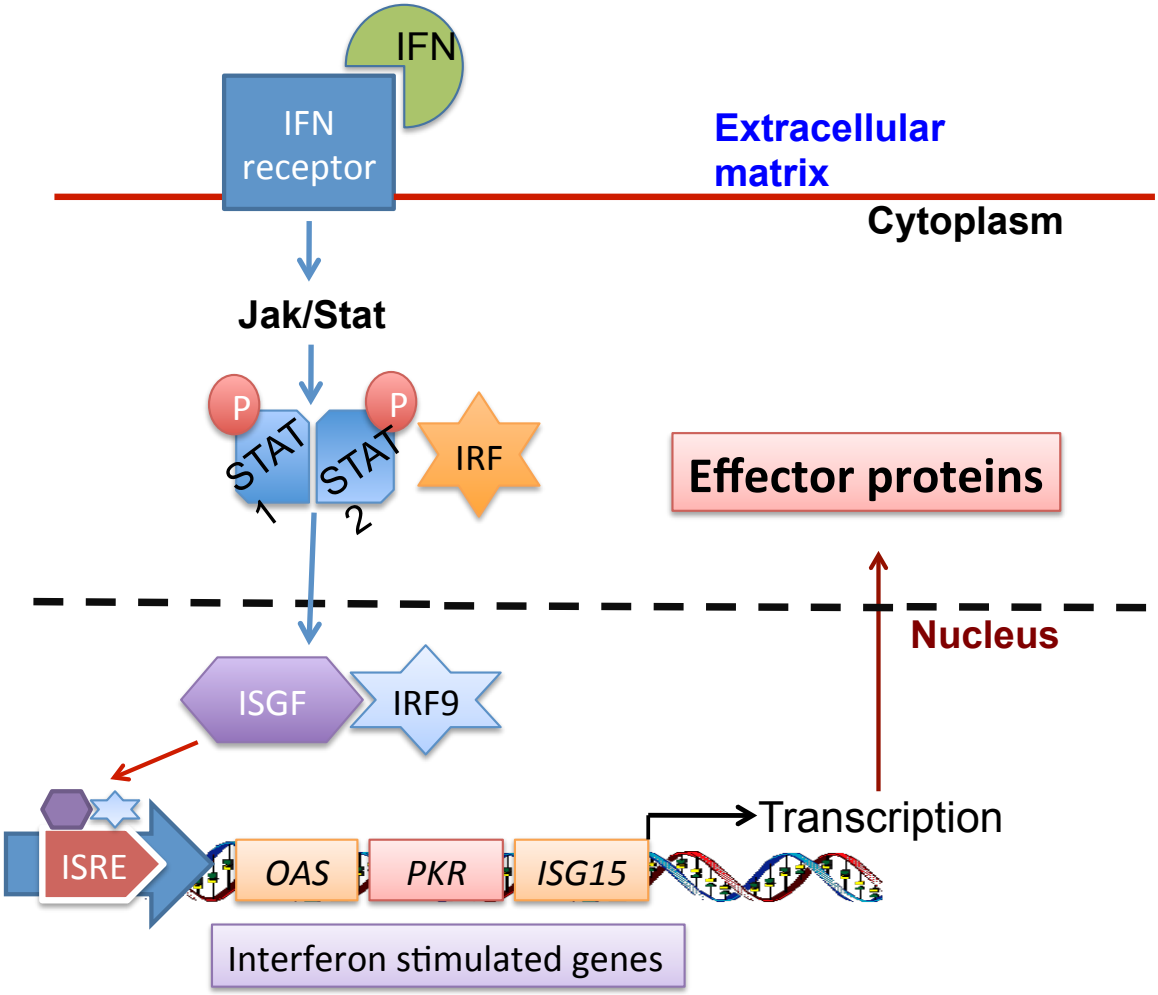

Figure 1.2 Autocrine and paracrine effect of IFNs. The interferon released from the cell will bind to IFN receptors on the cell surface and activate production of a number of antiviral effector proteins and PRRs that are encoded by interferon-stimulated genes (ISGs). The induction of effector proteins production is possible

through intricate pathways where intermediary kinases relay the message from the cell surface receptor into the nucleus. Interferon regulatory factors (IRFs) play a major role and forms interferon stimulates gene factors (ISGF), which binds to interferon stimulated response element (ISRE) in the promoter region of ISGs leading to higher level of transcription these genes. Adapted from [5,33].

(Mx1) and ISG15 [33,41]. These ISGs include PRRs, cytokines and effector proteins that amplify the IFN response in an effort to cohesively prevent viral multiplication inside the host cell and induce antiviral response in neighboring healthy cells [42] .

Although the mechanism is unclear, it has been shown that IRF3 is capable of inducing a subset of ISGs in an IFN independent manner [43,44]. The lack of IFN dependency in these responses could be because of the absence of high enough stimuli to activate NFkB, which has a higher threshold compared to IRF3 [10]. This type of IFN-independent ISG induction by IRF3 has been reported in response to membrane perturbation by viral infections. Other IFN-independent pathways have been reported in the antiviral response against Hepatitis C Virus (HCV), Dengue Virus (DENV) and Chikungunya virus effected through RLRs and TLRs activation (antiviral PRRs) [45-48].

Individuals with a deficiency in one of the important factors in the interferon response are highly susceptible to viral and mycobacterial infections [49]. Some of the known deficiencies include dominant STAT-1 deficiency [50,51], deficiency of IL-12 (key member of IFN- γ inducing cytokine) or its receptor [52-55], and deficiency of IFN- γR1 and IFN- γR2 (receptors of IFN- γ) [56,57] [58,59] .

1.2.2 VIRAL SENSING AND ANTIVIRAL RESPONSE BY PATTERN RECOGNITION RECEPTORS

When viruses invade a cell, viral PAMPs including viral nucleic acids and proteins, are sensed by PRRs. These PRRs are responsible for not only sensing these PAMPs

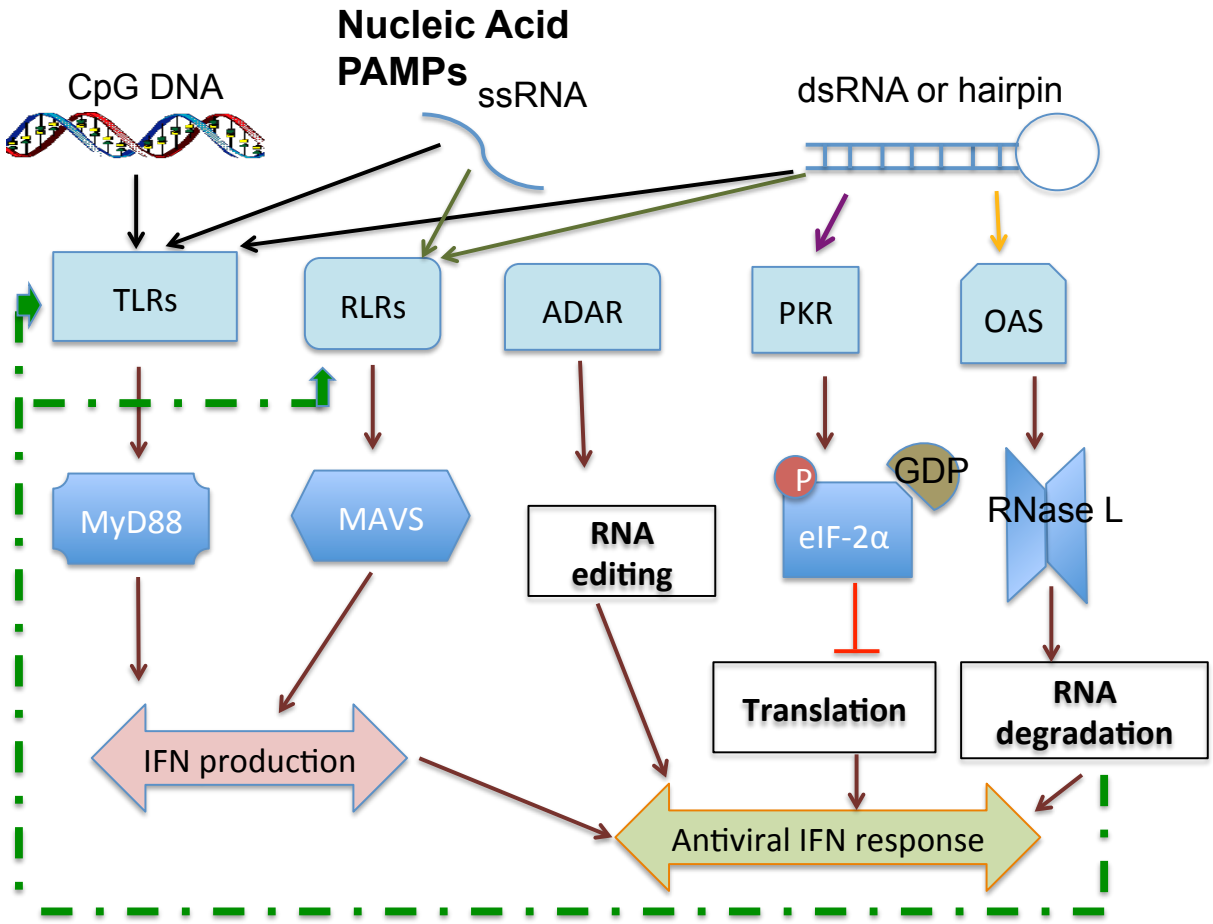

Figure 1.3 Schematic representation of pattern recognition receptors that sense viral nucleic acid PAMPs. Major adaptor proteins like MyD88 and MAVS for TLRs and RLRs respectively have been shown and these PRRs are efficient in inducing IFN production. Antiviral effector properties of ADAR via RNA editing and PKR via translation inhibition are listed here. OAS can activate RNase L leading to RNA degradation and these degraded RNA can act as PAMPs for TLRs and RLRs [60]. The innate immunity transmits signals to adaptive immunity that includes IL-12, IL-4 and IL-6, and also contributes to phagocytosis and antigen presentation necessary

for adaptive immune response [61]. Adapted from [33,62]. Various pathways shown here and the related abbreviations will be discussed in the following sections.

but also for inducing interferon production thereby initiating and amplifying the interferon cascade. Basal levels of PRRs in an uninfected cell are very low but their overexpression is induced via the IFN cascade to mount an appropriate and adequate antiviral response [5]. The focus of this thesis will be on PRRs that recognize viral nucleic acids as PAMPs, including single stranded RNA (ssRNA), and double stranded RNA (dsRNA) or DNA. **Figure 1.3** gives an overview of the established PRRs that detect nucleic acid PAMPs and an overview of how they initiate/amplify the antiviral response. Each of these PRRs will be discussed, ultimately focusing on OAS enzymes, the focus of my research [5,63].

1.2.2.1 Toll-like receptors

TLRs are a large group of PRRs that detect nucleic acid PAMPs, playing a major role in innate immunity by inducing IFN production and ultimately the IFN cascade [64,65]. TLRs are homologous to Toll receptors in *Drosophila* and hence named Toll-like receptors. The Toll receptor was shown to be important in the antifungal immune response in *Drosophila*, and TLRs in mammals play a major role in innate immunity, suggesting that they are functionally evolutionarily conserved PRRs [64,65]. There are 10 TLRs (TLR1 to TLR10) reported in humans [66]. TLRs contain an amino terminal ectodomain with leucine-rich repeats for recognition of PAMPs, a trans-membrane domain and a carboxy-terminal cytoplasmic domain (Toll-interleukin-1 receptor (IL-1R) homology (TIR) domain) enables downstream

signaling to induce the IFN antiviral and anti-inflammatory cytokine responses [67,68]. TLRs localize either on the cell membrane or inside the cell on the membranes of endosomes and lysosomes. TLR1, TLR2, TLR6 and TLR10 are present on the cell membrane and recognize microbial PAMPs including lipoproteins and peptidoglycans. TLR4 and TLR5, also present on the cell membrane, recognize other PAMPs of microbial origin including lipopolysaccharides (LPS), a major component of outer surface membrane of Gram-negative bacteria [66]. TLR2 and TLR4 can sense viral PAMPs including viral structural and non-structural proteins [69-72].

TLR3, TLR7, TLR8 and TLR9 are present in endolysosomal compartments and detect viral genetic material to initiate the innate immune response [66]. TLR3 recognizes dsRNAs; TLR7 and TLR8 recognize ssRNAs, whereas TLR9 binds unmethylated CG rich sites of DNA (cytosine followed by guanine) from viruses and bacteria [73-77]. The interaction of PAMPs with TLRs, which often involve co-receptors, leads to two important signaling pathways named after their respective adaptor proteins, the myeloid differentiation primary response 88 (MyD88), and the Toll-interleukin-1 receptor-domain (TIR-domain) containing adaptor inducing interferon (IFN)-β (TRIF)] [78,79]. The TLRs act via the TRIF dependent pathway with two exceptions: TLR3 signals through the MyD88 dependent pathway and TLR4 that uses both MyD88 and TRIF dependent pathways [62,79,80]. TLRs activate transcription factors including IRF3, IRF7 and NFkB thereby inducing downstream interferon response [66,81-83].

TLRs have shown to be important in our antiviral response through many *in vitro* and *in vivo* studies [84]. Mice lacking either TLR3 or TRIF are highly

susceptible to DNA viruses including mouse cytomegalovirus (MCMV) and herpes simplex virus 2 (HSV 2) [85-87]. Similarly, mice lacking TLR3 show increased viral burden and mortality to infection by a ssRNA virus, encephalomyocarditis virus (EMCV) [88]. TLR3 can also combat HCV and DENV infections (members of family *Flaviviridae*, positive sense ssRNA viruses) [89,90]. Sensing ssRNA viruses and generating an optimal IFN response in plasmacytoid dendritic cells is greatly dependent on TLR7 [91]. Viral PAMPs from ssRNA viruses including Sendai virus, HIV-1 and flaviviruses (hepatitis C virus, dengue virus and West-Nile virus) are effectively countered by an antiviral immune response mediated via TLR7 and TLR8 [76,77,92-95]. TLR9 has been observed to mediate the antiviral response against DNA viruses including MCMV, HSV-1 and HSV-2 [73,84,86,96,97]. For DNA viruses like mouse poxvirus and ectromelia virus, the only PRR that is shown to recognize their PAMPs is TLR9 [97,98]. Antiviral immune responses against DNA viruses (MCMV, RSV and Vaccinia virus) by TLR2 have also been reported. In these antiviral responses TLR2 works either alone or together with TLR6 to execute its action [99].

1.2.2.2 Retinoic acid-inducible gene-1 (RIG-I) like receptors

The RIG-like receptors (RLRs) are a family of PRRs that include RIG-I, melanoma differentiation associated gene 1 (MDA5) and laboratory of genetics and physiology 2 (LGP2) [100]. The RLRs bind nucleic acid PAMPs and activate the interferon cascade [100]. The features of nucleic acid PAMPs recognized by RIG-I are 5'-triphosphate (5' ppp) and stable secondary structures including hairpins of RNA [239,240]. The RLRs are cytoplasmic and not membrane associated [11,100]. The

RLRs are related proteins with a central ATPase containing DExD/H (depicting the sequence of conserved amino acids where 'x' is any amino acid that is not conserved) box helicase domain, but differ in the presence or absence of downstream signal transducer domains and/or a repressor domain (RD) [11]. These C-terminal RDs play a role in auto-regulation by RLRs locking them in a closed, inactive form. Post-transcriptional modifications including phosphorylation and acetylation are important in RLRs regulation. Phosphorylation of key-residues including T770, S854 and S855 by casein kinase II also play an important role in regulation of the resting state in RIG-I [101]. RIG-I and MDA5 contain N-terminal tandem caspase activation and recruitment domains (CARD), which are the functional domains of RLRs, responsible for downstream signaling leading to IFN cascade [11]. These CARDs interact with the CARD motif of downstream adaptors including mitochondrial antiviral signaling (MAVS) [102]. LGP2 lacks a CARD, distinguishing it from other RLRs [11]. The repressor domain is absent in MDA5 but present in RIG-I and LGP2 [100,103]. The absence of a RD in MDA5 leads to high expression of MDA5 but not RIG-I, which may cause the activation of downstream signaling cascade even in the absence of PAMPs [104,105]. Both RIG-I and MDA5 recruit an adaptor protein MAVS, which then signals IFN β production leading to the antiviral interferon cascade through IRF3 and NFkB [100,106]. The MAVS recruitment of IRF3 proceeds through the phosphorylation of MAVS at two specific Ser/Thr clusters (Ser426, 430 and 433; Ser 442, 444, Thr 445, Ser 446) by Ser/Thr protein kinases, TANK-binding protein kinase 1 (TBK-1) and/or inhibition of IkB kinase (IKK), and binding of MAVS to a positive charged surface of IRF3 [107]. The

IRF3 is then phosphorylated/activated by TBK-1 [107].

The antiviral response against many ssRNA viruses (*Orthomyxoviridae*, *Paramyxoviridae* and *Rhabdoviridae*) requires RIG-I. RIG-I is also important in recognition of viral PAMPs from *Flaviviridae* including Hepatitis C Virus (HCV) and Japanese Encephalitis Virus (JEV)[108,109]. Although RIG-I can't recognize DNA viral genomes directly, transcription products generated using the viral genome as the template by RNA polymerase III provides ideal targets to RIG-I [110,111]. MDA5, with its different pattern recognition compared to RIG-I, plays an important role in the IFN mediated antiviral response against members of *Picornaviridae*, for example EMCV, Murine hepatitis virus and Murine norovirus [112,113].

LGP2 lacks the CARD domain and hence was thought be a negative regulator of RLR signaling [101]. However, *in vivo* experiments with LGP2-deficient mice were contradictory to this hypothesis. LGP2 has been shown to be critical to antiviral response by RIG-I and MDA5 against EMCV, an ssRNA virus [114,115]. Although the mechanism is unclear, LGP2 is important in viral RNA recognition by RIG-I and MDA5 making it critical in initiating an IFN antiviral response against members of *Picornaviridae* (ssRNA virus) [116].

1.2.2.3 Nucleotide-binding and oligomerization domain (NOD)-like receptors

Nucleotide-binding and oligomerization domain (NOD)-like receptors (NLRs) are another important antiviral PRR family with major role in both the antibacterial immune response and in chronic inflammatory diseases [117]. These PRRs have an evolutionarily conserved NTPase domain (NACHT domain), whose oligomerization

is thought to be necessary for NLR activation. NOD1 and NOD2 belong to one subfamily called NLRC/X due to the presence of a CARD (functional motifs found on proteins mainly involved in inflammation and apoptosis mediating protein-protein interaction) as their signal transducer domain [118] [102]. The NLRs with a pyrin domain are categorized under NLRP subfamily [119].

NLRP3 has been implicated in the antiviral IFN response against RNA viruses (for example: Sendai virus, Influenza virus and DNA viruses including Adenovirus), whereas NLRX1 has been shown to be important in antiviral response in human cell lines against a variety of RNA viruses [120,121]. Chronic inflammatory diseases are associated with mutations in the genes coding for NLRs highlighting them as an important regulatory component in inflammation and innate immunity. A few of these inflammatory diseases related to a specific NLR mutation are Crohn's disease associated with NOD2, atopic disorder associated with NOD1, and Vitiligo associated with NLRP1 [122,123]. NLRs have also been shown to interact with bacterial PAMPs (including peptidoglycans) and in addition they also recognize environmental hazards like silica and asbestos molecules [117,120].

1.2.2.4 Adenosine deaminase acting on RNA (ADAR)

ADAR is an important ISG-encoded antiviral effector protein that binds dsRNA and enzymatically converts adenosine (A) to inosine (I) [124]. This replaces an A:U base-pair in dsRNA with an I:U mismatch. The RNA editing effected by ADAR impacts the activity of the ribosome, spliceosome and viral RNA dependent RNA polymerases when they read the inosine as guanosine, changing the coding sequence from A to G.

This change in sequence can also be incorporated into the viral RNAs, as RNA viruses have RNA as their genome and viral RNA dependent RNA polymerase is responsible for their replication [125-127]. These mutations are often deleterious to the virus negatively affecting its replication, viral propagation or altering the code for a viral protein thereby affecting the protein function [125,126].

The C-terminal domain of ADAR contains three copies of the dsRNA binding motifs (dsRBMs), the catalytic deaminase domain is centrally located, and the N-terminal domain has a Z-binding domain that binds to both Z-RNA and DNA [128-130]. The large isoform of ADAR1 (p150) is localized in both the cytoplasm and the nucleus, while a smaller isoform (p110) is primarily localized in the nucleus [131-133].

ADAR functions as both an antiviral and a proviral factor. Whether ADAR will be proviral or antiviral depends on both the type of host cell and the virus. The antiviral properties of ADAR have been extensively studied and have been shown to be important against negative strand ssRNA viruses (measles virus, respiratory syncytial virus and influenza virus) and positive strand ssRNA viruses (HCV, retrovirus like human immune- deficiency virus) [134-140]. Similarly, some dsDNA viruses (polyoma virus and Kaposis sarcoma virus) are also controlled by an immune response where ADAR plays important role as an effector antiviral protein [141,142]. Noteworthy proviral properties of ADAR include suppression of PKR (section 1.2.2.5), OAS (section 1.2.3) and IRF3 activation (section 1.2.1), hence stifling amplification of the IFN response [143-146]. Conversely, some of the viruses (for example hepatitis D virus) need mRNA editing by ADAR to ensure proper

translation of viral proteins [147,148]. Cellular RNA editing is another function of this multifaceted protein where it is likely to be affecting RNA stability, and hence impacting RNA function and localization [149]. Some researchers proposed the idea that ADAR may function to curb deleterious immune response against cellular self-molecules. A long duplex cellular RNA, which may have the potential to induce innate immunity, could be edited by ADAR, replacing A:U match by I:C mismatch thereby reducing secondary structures and making it a less likely target of nucleotide-binding PRRs and helping the host to avoid undesirable initiation of innate immunity [149].

1.2.2.5 dsRNA dependent protein kinase (PKR)

Investigating translational inhibition in cell-free systems from IFN-treated cells and virus infected cells led to the discovery of two important dsRNA binding antiviral enzymes: PKR and OAS [150-157]. PKR is an antiviral enzyme activated mainly by viral dsRNA, although it also has protein activators like protein activator of the interferon-induced protein kinase (PACT) and heparin (an anticoagulant) [158,159]. Activated PKR inhibits protein translation inside the host cell thereby inhibiting cellular and viral protein translation [158,159]. The protein has two dsRNA binding motifs (dsRBMs) connected by a short linker at its N-terminus, which enables interactions with the dsRNA, and a Serine/Threonine kinase domain constitutes its C-terminus. The Ser/Thr kinase domain is required for PKR's enzymatic activity of target substrate phosphorylation. The kinase domain is connected to the dsRBMs by an 80 residue flexible linker, thought to enable PKR dimerization [160]. PKR

dimerization enables trans auto-phosphorylation of the kinase domain of inactive monomers, a requirement for enzymatic activation [161]. The Ser/Thr kinase needs phosphorylation at both Thr446 and Thr451 but other phosphorylation sites (for example, Tyr residues at 101, 162 and 293) also regulate enzymatic activity [162-164]. Once activated, PKR phosphorylates the alpha subunit of eukaryotic initiation factor 2 (eIF-2α) at Ser51, locking it in a guanosine diphosphate (GDP) bound state. For the eIF-2α to be in a guanosine triphosphate (GTP) bound state the guanine nucleotide exchange factor (eIF-2β) has to accomplish GDP to GTP exchange but the phosphorylated eIF-2α results in higher-affinity binding of eIF-2β to the eIF-2 [165-168]. As the cellular level of eIF-2β is much lower compared to eIF-2, the phosphorylation of eIF-2α leads to a dearth of free eIF-2β. This results in locking of the eIF-2 in a GDP bound state resulting in translation inhibition [165-167]. As viruses are dependent on their host cells for viral protein translation, inhibition of cellular translation also inhibits viral protein translation [165-167,169]. PKR has been implicated in the antiviral response through not only inhibition of translation but also by affecting integrity of IFN mRNA itself as cells lacking PKR demonstrate shortened poly A tails [170]. PKR is predominantly cytoplasmic and is concentrated at ribosomes upon its activation. PKR is also involved in stress-induced apoptosis where PKR translocates into the nucleus. PKR activation by TLRs, growth receptors and cytokines that includes IFNs, TNF- α and IL-1, has been reported [33].

Transgenic mouse models with defective PKR demonstrated increased susceptibility to viral infections, including influenza virus and bunyawera virus [158,171]. The antiviral effect of PKR against RNA viruses include positive sense

ssRNA viruses (HCV [172], foot and mouth virus [173], EMCV [174], WNV [175]), and negative sense ssRNA viruses (hepatitis D virus [176]). PKR exerts its antiviral effect against dsDNA viruses (Simian virus (SV)) through viral transcription intermediates [33,177,178]. Unlike many other PRRs including TLRs and RLRs that are not antiviral effector proteins, PKR can act as both an effector antiviral protein directly involved in restricting viral propagation by inhibiting translation and also as an important PRR that recognizes viral nucleic acid PAMPs [165-167,169].

1.2.3 2' 5'-OLIGOADENYLATE SYNTHETASES

The OAS enzymes are nucleotide transferases that function as key antiviral pattern recognition receptors, which sense viral dsRNA. Binding of viral dsRNA activates OAS [179]. Activated OAS produce 2'-5'-linked oligoadenylates that stimulate ribonuclease L (RNase L) and ultimately slow viral propagation [179]. The OAS enzymes catalyzes 2'-5'-oligoadenylate chains production using ATP as the substrate with pyrophosphate (PPi) produced as a by-product [180,181]. The interferon cascade induce OAS enzymes [182,183]. Human chromosome 12 houses four related *OAS* genes that are collectively referred to as the OAS family. The four members are *OAS1, OAS2, OAS3* and *OASL* (OAS like) [182,184-186]. The genes for *OAS1, OAS2* and *OAS3* are encoded by a region on chromosome 12 that is 120 mega-bases (Mb) away from the telomeric end, whereas the *OASL* is 129 Mb away from the same end of the chromosome [187,188].

A 346 amino acid stretch, termed the OAS domain, is common to all OAS1 splice variants at their N-terminus. Homologous domains are present in OAS2 and

OAS3. Whereas OAS1 has one OAS domain in it, OAS2 has 2 and OAS3 has 3 homologous OAS domains. The percentage of homology between the OAS domains present in OAS1 to homologous domains present in OAS2 and OAS3 is in the range of 40% to 60% [189,190].

Depending on the OAS family member, their genes contain one or two 3' exons where differential splicing variants are produced in humans. OAS1 has four splice variants identified by the suffix (p) and their molecular weight in kilo-Daltons (p42, p44, p46 and p48); OAS2 has two (p69 and p71); there is only 1 splice variant of OAS3 [189,191-193]. It was demonstrated that the transcription of these genes could be induced by IFN. In the case of OAS2 the differences in the sizes of RNAs to the translated proteins result from different non-coding 3' termini due to alternative polyadenylation sites [189,191,194-197]. Unlike the OAS1, OAS2 and *OAS3* produces a single 7 kb RNA [198]. The N-terminal, 346 amino acids for OAS1 splice variants and the first 683 residues amongst OAS2 splice variants p69 and p71 are identical. The variation in the carboxy-terminal of OAS1 splices variants can be attributed to differential splicing [189,191,194,199]. The *OASL* gene encodes a p59 version with splice variants p56 (OASL a), p43 (OASL d) and p30 (OASL b). The OASL splice variants have an OAS homology domain and a carboxy–terminal domain homologous to a tandem repeat of ubiquitin [190,200,201].

1.2.3.1 Enzyme catalysis and possible oligomerization requirement for enzymatic activity sheds light on the evolution of OAS enzymes

As the name suggests, the OAS enzymes catalyze adenylate chain formation in a 2' to 5' direction. Bioinformatics and homologous modeling study suggested that the ribose sugar on the adenosine monophosphate that attaches to the incoming ATP substrate molecule is oriented in a way that the 2' end is available and catalytically active [202]. OAS enzymes belong to the superfamily of nucleotidyl transferases that include poly A polymerases (PAP) and the class I CCA adding enzyme. This grouping is based on bioinformatics studies that showed the presence of a sequence motif in the active sites of OAS enzymes conserved in the nucleotidyl transferases superfamily (G[G/S]$X_{9\text{-}13}$DX[D/E]) where X is any amino acid [203]. OAS enzymes have the greatest similarity to the eukaryotic PAPs, enzymes that polymerize 3'-5'-linked polyadenylates [202]. The OAS family is also structurally related to other polymerases including the class I CCA adding enzyme. OAS enzymes along with the PAP and class I CCA adding enzymes are categorized as template independent polymerases, and like these enzymes OAS have a palm domain (5-stranded β-sheet domain) and a C-terminal domain comprising of four helixes forming a bundle [202].

Based on the similarity of OAS enzymes and PAP/class I CCA adding polymerase and on the complex enzymatic activity required to build 2'-5'-A chains, it is thought that OAS oligomerization may be required for activity. In support of this theory, gel filtration chromatography experiments on IFN-treated human cells yielded a possible tetramer of OAS1 (180 kDa), dimer of OAS2 (160 kDa), and

monomer of OAS3 (100 kDa) [204]. It is therefore suggested that four OAS domains, a tetramer of OAS1 or a dimer of OAS2, may be required for catalytic activity [205]. Active OAS2 p69 isomer dimers where one subunit is bound to the donor and the other to the acceptor ATP molecule had been reported [206]. Through mutational studies, the presence of a tripeptide motif containing a cysteine, a phenylalanine and a lysine (C331-F332-K333) has been implicated to be important in oligomerization of OAS1 and this motif is found to be conserved in p69 isomer of OAS2 [207]. The absence of a C-F-K motif in OAS3 is consistent with its purification as a monomer [204].

At present there are two general mechanisms proposed for OAS enzyme function, and each is moderately supported by published data. The first mechanism is the dissipative process where after addition of each adenylate to complete one step in the chain extension, the intermediate 2'-5'-A chains are released and recaptured by another active OAS enzyme to carry out the next step of chain extension [208,209]. Experiments to support the dissipative mechanism where the smaller oligoadenylates (dimer and trimer of 2'-5'-A) expended for the formation of larger oligoadenylates were carried out using partially purified rabbit enzyme or recombinant OAS2. The comparatively low affinity of human OAS enzymes towards 2'-5'-A dimers relative to monomers raises doubt over the dissipative mechanism [186]. The other proposed mechanism of 2'-5'-A synthesis is the processive mechanism. In this, it is suggested that the OAS self-association enables cooperation to provide sufficient catalytic sites capable of synthesizing the intended 2'-5'-A chain without releasing it in intermediary state. This model is consistent with suggested

tetramerization of OAS1 and dimerization of OAS2 [210]. A mixture of both the dissipative and processive mechanism may also be possible, but has not been tested experimentally.

In vitro activation assays have shown the optimal pH for enzymatic activity of OAS1, OAS2 and OAS3 falls in the pH range of 6.6 to 7.5 [205,211,212]. Members of the OAS family differ in their affinity to dsRNA. Enzyme kinetics studies performed on recombinant OAS1 showed the K_{app} (apparent $K_{m,}$ a measure of binding affinity) for *in vitro* transcribed viral dsRNA activators to be in the range of 1-2 μM [186,211-213]. Activation studies performed with purified OAS2 and OAS3 from IFN-treated cells showed glaring difference in the affinity of these two 2' 5'-oligoadenylate synthetases to dsRNA activators. OAS3 require RNA an concentration as low as 1 μg/mL compared to 100 μg/mL in case of OAS2 to be fully active at their respective optimal reaction conditions [185,186,210].

With the knowledge that OAS enzymes belong to the family of template independent nucleotidyl transferases, which are found in primitive life forms, investigations are underway to identify homologous proteins to provide insight into the evolution and function of human OAS enzymes. Homologs of OAS enzymes are reported in mammals including horse, pig, cat, cow and dog [214,215]. Enzymatically active OAS enzymes have been identified and investigated in mammals, in a bird, and in sponges [216-219]. Although it was initially believed that larger isoforms like OAS2 and OAS3 are only present in mammals, homologs of larger OAS enzymes have now been reported in primitive life forms like sponges

and metazoan [219-221]. Interestingly fish, sharks and many insect varieties gave don't appear to contain OAS homologs [220].

1.2.3.2 OAS1 structure

To date, high-resolution structures of the smallest isoform, OAS1, have been determined from porcine and human [217,222]. OAS1 adopts an imperfect globular shape containing two domains (bilobal). The catalytic domain (residues 19-154) follows a short chain of 18 residues (1 to 18) at the N-terminus. The C-terminal domain, comprised of residues 185 to 349, is connected to the catalytic domain via a helix-loop-helix linker. Packing of this bilobal OAS1 structure is enabled by the short chain at its N-terminal acting as an anchor to the C-terminal domain. The catalytic domain adopts the palm domain fold and contains five antiparallel β strands punctuated by few α helices (α β β α β β β). This palm domain is conserved in nucleotidyl transferases related to OAS [202,217]. An aspartic acid triad that comprises of D75, D77 and D148 has been suggested as the key catalytic residues in the active site of the enzyme [217,222].

The high-resolution structure revealed the presence of a negatively charged cleft formed between the two domains of OAS1. A combination of data from high-resolution structure and mutational studies on porcine OAS1 hypothesized that the RNA binding region is in a positively charged cavity opposite of the negatively charged cleft [217]. The crystal structure of human OAS1 bound to dsRNA showed that the RNA recognition and binding involved interactions with two minor grooves of the RNA [222]. The two dsRNA-binding sites that interact with the two

consecutive minor grooves are approximately 30 Å apart. The structure of dsRNA with 18 bps bound to OAS1 showed that the terminal 6 base pairs (bp 13-18) had a closer interaction with the N lobe of the OAS1. Base pairs between 2 to 8 are proximal to and interact mainly with the C lobe of protein [222]. Additionally, amino acids including K42, R195, K199, K204 and R210 that were reported previously to be involved in RNA-protein interaction were shown to be part of the RNA-protein interface [202,217,222,223].

Based on structural studies, binding to the dsRNA is hypothesized to cause conformational changes to OAS1 necessary for the placement of the catalytic aspartic acid triad at the optimal position for 2'-5'-oligoadenylate catalysis. Major conformational changes to both the secondary and tertiary structure of OAS1 occur. These changes include residues K66, R195 moving near E233, and the formation of a new helix in the N-terminal region. These changes bring catalytic acid triad (D75, D77 and D148), previously far apart in the proenzyme (OAS1 with no dsRNA activation), together in a compact orientation. This new orientation is crucial for catalytic activity that performs the necessary coordination with two Mg^{2+} ions [222].

1.2.3.3 Localization of OAS and their dsRNA affinity

2' 5'-oligoadenylate synthetases are localized both in the nucleus and cytoplasm. Moreover, they are found in ribosomal, mitochondrial and endoplasmic reticulum subcellular fractions. OAS1 and OAS2 are found in both mitochondrial and endoplasmic reticulum subcellular fractions. OAS2 that is post-translationally modified with myristoylation (addition of lipid, myristoyl group) is associated with

both nuclear and endoplasmic reticulum membranes. OAS3 has been shown to be mainly in the ribosomal fraction, but has also been found in the nucleus [184,185,224].

1.2.3.4 2'-5' Adenylate chain synthesis and subsequent activation of OAS/RNase L pathway

The adenylate chains (2'-5'-A) synthesized by the OAS enzymes activate the RNase L, a single-stranded ribonuclease that mediates the antiviral response by the OAS enzymes (**Figure 1.4**). Specifically, 2'-5'-A chains are the only known cellular activators of RNase L [179]. The 2'-5' phosphodiester bond, and not the 3'-5' phosphodiester bond typically found in polynucleotides, is necessary for activation [186]. Sub-nanomolar concentrations of 2'-5'-A chains are capable of activating RNase L, leading to degradation of ssRNA where the favorable endoribonuclease attack sites are those following UU and UA sequences [180,225]. It is noteworthy that two enzymes, 5'-phosphatase and 2'-phosphodiesterase, play a major role in controlling the OAS/RNase L pathway in resting cells. The 5'-phosphatase inactivates the 2'-5'-A chains by removing 5' phosphate whereas the 2'-phosphodiesterase hydrolyzes phosphodiester bond, thereby preventing the interferon response via the OAS/RNase L pathway in cells that aren't virally infected [226,227].

Focusing on 2'-5'-A chain length of the adenylate chains, the trimeric form of 2'-5'-A is the most common oligoadenylate chain synthesized by OAS family members [227]. OAS1 synthesizes mixture of dimeric, trimeric, tetrameric and even

higher forms, with the trimeric form being predominant. OAS2 synthesizes trimeric adenylate chains as its dominant product [198,222,228]. A recent publication on OAS3 purified from baculovirus reported that it is capable of synthesizing both dimeric, trimeric and even longer adenylate chains [229]. Although the length of the adenylate chain has been suggested to affect the affinity towards RNase L, there is not much difference in RNase L activation potency of trimer, tetramer or pentamer forms of 2'-5'-A chains [180,230]. All these forms of 2'-5'-A resulted in comparable levels of RNA degradation, but the dimeric form was a poor activator [180,230].

1.2.3.5 RNase L, the effector protein: structural insight into its activation and function in OAS/RNase L pathway

RNase L has three domains: ankyrin repeat domain (ANK), a pseudo-kinase domain (PK) and a C-terminal ribonuclease catalytic domain. The PK domain is devoid of catalytic activity [231,232]. Binding of 2'-5'-A chains to the ankyrin repeat domain leads to activation of inactive RNase L. The binding of 2'-5'-A chains to the RNase L also requires the PK domain to meet structural requirements to accommodate the activator adenylate chain [232]. Subsequent activation occurs by coordinated dimerization of inactive monomers to form an active RNase L homodimer. The high-resolution structure of an RNase L dimer shows that the ankyrin repeats of one RNase L molecule is antiparallel with respect to the ankyrin repeat domain of other. The PK domain and ribonuclease domain of one RNAse L molecule in the homodimer are parallel to the same domains of the other molecule (**Figure 1.4**). These two domains (PK and ribinuclease domain) of each of the RNase L molecule

are twisted in a way that resembles a structure where they have been interchanged between the monomers [232]. This homodimerization of RNase L leads to cross-interaction of the KH domain with a characteristic helix αI of the ANK domain [231]. The interaction of N-lobe of KH domain with the αI helix, including the residue R238 mediated contact plays a major role in RNase L activation 2'-5'-A [231].

1.2.3.6 RNase L dependent antiviral and biological function and the relationship to OAS enzymes

A

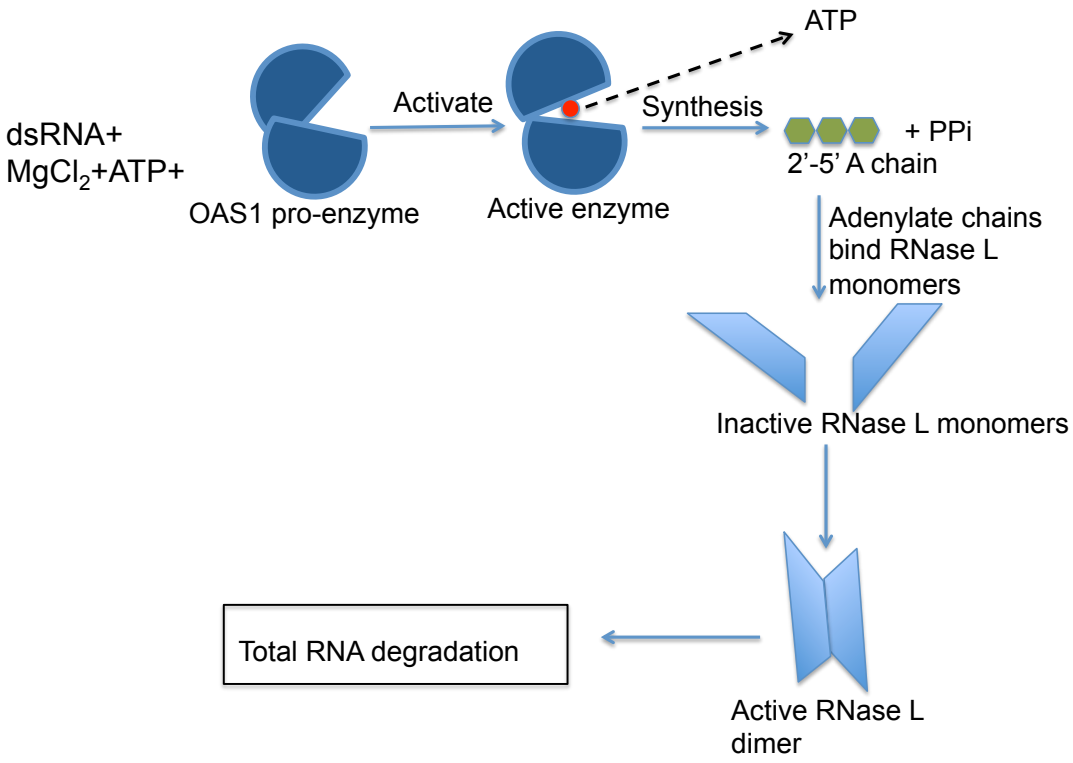

B

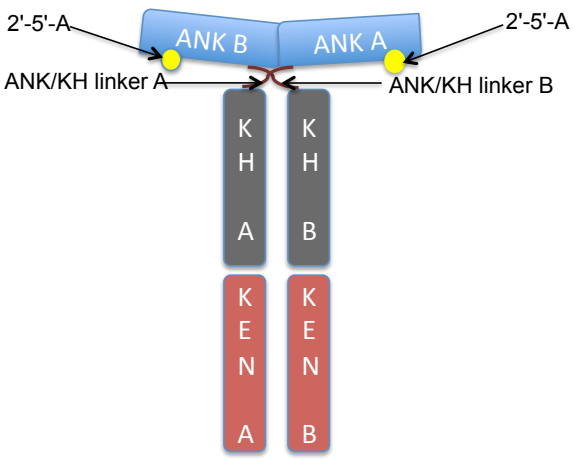

Figure 1.4 Activation of OAS1/RNase L pathway. **(A)** Binding of dsRNA to OAS1 proenzyme results in conformational changes making the enzyme active. These conformational changes make the active site groove narrower and deeper bringing it close to the dsRNA-binding region. The active conformation of OAS1, in the presence of $MgCl_2$ and ATP, synthesize adenylate chains, possibly through oligomerization of the active enzyme. Binding of adenylate chains to inactive RNase L monomers results in active RNase L homodimers. **(B)** Schematic representation of the active RNase L homodimer. The ANK domain of homodimers appears to be exchanged. Active RNase L degrades total RNA (both viral and cellular) leading to apoptosis. Adapted from [33,222,231].

RNase L activated by the 2'-5'-A chains degrade both viral and cellular RNA [180,225]. RNA degradation by RNase L ensures inhibition of viral protein synthesis. Degraded RNA fragments trigger activation of other pattern recognition receptors including RIG-I and TLRs. The OAS/RNase L pathway also induce the type I interferon response via RIG-I, MDA 5 and IPS-1 (**Figure 1.3**) [233].

Initiation of apoptotic pathways follows total viral and cellular RNA degradation by RNase L [234]. Various research groups have reported a strong link between OAS/RNase L pathways to apoptosis [235]. Stable cell lines expressing RNase L resulted to some degree of apoptosis. Addition of 2'- 5'-A chains to cells

overexpressing RNase L also lead to induction of apoptosis [234,236]. RNase L plays a major role in apoptosis as lower levels of apoptosis occur in RNase L negative cell lines [234].

The antiviral response of OAS/RNase L pathway is well established against many RNA viruses, but DNA viruses are also targeted as their transcription products can form dsRNAs through annealing of RNA strands of opposite polarity [237]. The OAS1 and RNase L pathways are activated in cells infected with EMCV (a member of *picornaviridae*), a ssRNA virus [238,239]. Mammalian cells treated with extracellular OAS1 have been shown to have an antiviral effect against EMCV via an unknown pathway where an IFN-I independent manner and there is absence of up-regulation of known ISGs [240]. Both OAS1 and RNase L have been implicated in suppression of Mengovirus (family: *picornaviridae*) replication and against Coxsackievirus infections [241] [237,242]. The OAS/RNase L pathway plays important role in the antiviral response against (family: *picornaviridae*). Coxsackievirus causes diseases including myocarditis and meningitis. Mice deficient in RNase L become highly susceptible to this viral infection [237,242]. Furthermore, antiviral type I IFN response against HIV is negatively affected when RNase L is down-regulation using antisense RNA [243]. As well, two OAS1 isoforms and OAS3 have been implicated in antiviral response against Dengue virus (family: *flaviviridae*, a ssRNA virus) infection [244]. Stimulated OAS enzymatic activity is recorded after trial vaccination against Yellow fever (a flavivirus) [245]. Chronic infection to Hepatitis C virus, another member of the *flaviviridae* family, also highlights a link to OAS1 gene [246].

Amongst other IFN response proteins, high activity of OAS enzymes has been associated with type I diabetes [247]. Prostate cancer patients that have impaired RNase L, show the presence of xenotropic murine leukemia virus-related virus (XMRV) suggesting a strong association of prostate cancer with XMRV [248]. Another critical example is the role played by RNase L in controlling the neurotropic *Corona virus* strain JHM that has a demyelinating effect on the central nervous system of mice. RNase L deficiency in the case of this sub-lethal viral infection shows lethality and faster disease progression [249].

The antibacterial effects of RNase L against *Bacillus anthrasis* (*B. anthrasis*) and *Escherichia coli* (*E. coli*) have been reported [250]. RNase L deficient mice, when compared to wild type mice, demonstrated much lower levels of pro-inflammatory cytokine production, which could explain why these RNase L deficient mice have a higher bacterial titer and mortality when faced with *B. anthrasis* and *E. coli* infection [250]. Expression levels of cathepsin, an important enzyme in lysosomes that plays a major role in lysosomal degradation of macrophage-internalized foreign substances of bacterial and other pathogenic origin, has been shown to be regulated by RNase L [250-252]. An enhanced antibacterial response could be possible through higher RNase L activity via the interaction of OAS2 with NOD2 in the presence of poly I:C (an synthetic dsRNA activator of OAS and IFN response) [253]. The antiviral and antibacterial response of the OAS1/RNase L pathway is not confined to animals only, as transgenic plants expressing OAS and RNase L show higher viral resistance compared to mock transgenic ones [254].

OAS3 has been linked to mRNA splicing [205,255]. There is structural similarity between the 2'- 5' phosphodiester bonds and a lariat branch point that is the end product in splicing. In the presence of target RNA, OAS3 is associated with the 60S spliceosome complex [205,255]. The OAS enzymes are able to utilize GTP as a substrate. In fact GTP can be a potential donor or acceptor in OAS catalyzed 2'- 5'-A formation [210]. In summary, these findings implicate OAS3 to play a role in pre-mRNA splicing [255].

1.2.4 SENSING VIRAL NUCLEIC ACIDS AS PAMPs BY PRRs

The focus of this section will be on the specific PAMP features recognized by PRRs. The 5'-triphosphate (5' ppp) and stable secondary structures including hairpins are key signatures of RNA PAMPs recognized by RIG-I [256,257]. The 5' and 3' untranslated regions of the WNV genome, which are known to have stable secondary structured regions, are capable of activating RIG-I [258]. The positive sense WNV 5'-UTR can be readily recognized by RIG-I and induce a strong antiviral response. RIG-I recognizes the WNV 5'UTR that contains either a 5'ppp or a 5'm7G cap [258]. Activation of RIG-I requires a minimum of 19 bps and ideally devoid of any nucleotide overhangs at its 3' end. Generally, ssRNA are poor substrates to activate RIG-I [259]. However, ssRNA rich in polyuridine motifs (poly U and poly UC) and structured RNAs containing 5' ppp are capable of activating antiviral response via the RIG-I pathway [260]. For example, RNAs purified from HCV genome containing 5' ppp and rich in polyuridine motifs can activate RIG-I. Another interesting exception to RIG-I activation is short ~200 nucleotides RNAs lacking a 5'

ppp, that are a result of RNA degradation by RNase L. Furthermore, these short RNAs are also MDA5 activators [60]. Although the characteristics of PAMPs that are recognized by MDA5 are not fully defined, the length of the RNA has to be greater than a few thousand nucleotides [261,262].

For activation of TLRs, one of the most important families of PRRs for sensing nucleic acid PAMPs, length requirement and nucleic acid structural features vary (including the presence/absence of ssRNA and dsRNA regions). TLR3, which is capable of sensing infection from a wide range of viruses with dsRNA genomes, ssRNA genomes and DNA genomes, has been reported to bind to 40-50 bp dsRNA. dsRNA of 80-100 bp in length purified from HCV infected cells are reported to be good activators of TLR3 [66,263,264]. Although the length requirement has not been established for TLR7 or TLR8, they are able to recognize GU-rich and AU-rich regions of viral ssRNA [77,265]. TLR9 can recognize CpG motifs common in viral and bacterial DNA [74]. Although the characteristic PAMP features have not been ascertained, NLRs bind to both viral dsRNA and bacterial RNAs. [117].

ADAR has been shown to bind to perfectly complementary synthetic dsRNA, independent of its sequence and induce RNA editing. ADAR can also induce site-specific editing. In these cases, ADAR can recognize mismatched dsRNA structures including bulges and loops [266,267]. The solution structure of the individual dsRBMs of ADAR bound to dsRNA showed that the dsRBMs span two minor grooves and a major grove of the dsRNA. This study suggested sequence specificity of dsRBM binding to one of the two minor grooves involved in binding [268].

PKR, which contain its two dsRBMs, requires a minimum of 16 bp of dsRNA for binding. However, a recent study has suggested that the minimum dsRNA length requirement for PKR dimerization and activation is approximately double the length (~ 33 bps). Similar to ADAR, each dsRBM's requires at least 15 bp of dsRNA for their interaction. The binding interaction of each dsRBM of ADAR spans two minor groves and a major groove sandwiched between these minor grooves [268,269]. Imperfect non-canonical structures including bulges and loops in RNA ligands can influence binding to and activation of PKR [270-272]. Moreover, PKR has been shown to differentiate between RNAs based on the presence or absence of 5' ppp and may utilize this feature to discriminate from cellular RNA that are devoid of the 5' ppp [273]. Interestingly, RNA comprising a short stem-loops of ~16 bp with a ~10 nt ssRNA tail at either the 5' or its 3' end is capable of activating PKR, which contradicts to the reported ~ 33 bps requirement for PKR activation [274].

For the OAS family, the vast majority of work has focused on OAS1. The high-resolution structure of OAS1 bound to synthetic dsRNA suggests that an 18 bp region that spans two successive minor grooves is needed to interact with the RNA binding region of the enzyme [222]. The length requirement for high affinity binding was previously reported to be ~ 18 bp and confirmed by the high-resolution structure [222]. Longer dsRNA ligands are better activators of OAS1 compared to shorter dsRNA ligands [275]. The sequence dependency of OAS1 binding has not been fully established. However, a consensus sequences of a dsRNA (NNWWNNNNNNNNNWGN, where W stands for either A or T) separated by 9 bps (1 full turn of dsRNA helix) can activate OAS1 [276]. The same study also reported

that 2'-O methylation of dsRNA ligands can suppress OAS1 activity [276]. Despite these first insights into specificity, there appears to be a much boarder spectrum of RNA that will bind and activate OAS1, including ssRNA aptamers, cellular RNA and viral RNA (mRNA and genomic RNA) [211,213,277,278].

The variable length requirement of the ligands for different PRRs has been suggested as a way our immune system to recognize a wide range of RNA PAMPs (mainly dsRNA but ssRNA in some cases). The general consensus is that the PRRs are unlikely to have sequence specificity. This hypothesis is supported by various studies [262-264], but there are contradicting reports linking binding and activation of PRRs to consensus sequences [268,276]. For example, non-canonical structures like bulge and loops are tolerated and even in some cases preferred by PRRs [149,266,267,270]. For a protein (PRR in our case) to interact with a nucleic acid (dsRNA) in a sequence specific manner, it typically needs access to the major groove, but the dsRNA has deep and narrow major groove, making it difficult to access [279,280]. This property is probably a major reason for the sequence independent interaction that occurs between dsRNA binding proteins to their dsRNA ligands. Furthermore, the A-form helix of dsRNA, which contains shallow minor grooves, may explain the direct interactions with the RNA binding region/domain of proteins, thus highlighting the importance of the 2' hydroxyl exclusive to the ribose sugar of RNA. For example, modifications to the 2'-OH have a negative impact on binding to and activation of the respective PRRs [149,281-283].

General consensus is that the cellular RNAs avoid activating RNA sensing PRRs probably by the following strategies:

1. Nucleoside modifications, which suppresses activation of PRRs, including OAS1 [284,285].
2. 5' modifications including 5'-cap and 5'-OH may suppress OAS1 activation, but 5'-ppp (found mostly on viral RNAs) remains a signature characteristic of recognition by PRRs [104].
3. Interaction of cellular RNAs with ribonucleoproteins may also sequester possible sites, which may otherwise be recognized by PRRs [286].
4. The length and the structure of the cellular RNAs may also avoid/dampen recognition by the PRRs [286].

1.2.5 WEST NILE VIRUS AND THE INNATE IMMUNE RESPONSE TO IT

One of the major arbovirus that causes disease is the West Nile Virus (WNV). West Nile Virus is an 11 Kb positive sense single strand RNA virus, which belongs to the family *Flaviviridae* that includes pathogenic viruses such as Yellow fever (YFV), Dengue (DENV), Japanese encephalitis (JEV) and tick-borne encephalitis (TEV). The normal viral life cycle of WNV involves an infection cycle between mosquitoes and birds but it can also infect mammalian species including humans [287,288]. WNV is a classic example of a virus breaking geo-physical barriers. Once endemic to Africa, it has now established itself in other parts of the world including North America, Europe and India [289]. WNV, being an emerging infectious disease, is a major concern in the province of Manitoba. Since the first human case of WNV in Manitoba was reported in the summer of 2003, it has been reported almost every year since. In 2007 there were 582 reported human cases of WNV infection in the province of

Manitoba [290]. Therefore selecting WNV for my study was relevant especially with its negative impact on human health in Manitoba and other parts of the world.

1.2.5.1 WNV genome and secondary structures in its terminal regions

WNV is single-stranded RNA genome with a single open reading frame (ORF) that encodes a large poly-protein precursor that contains both structural proteins including capsid protein (C), membrane pre-protein/protein (prM/M) and envelope protein (E); and non-structural (NS) proteins including NS1, NS2A, NS2B, NS3, NS4A, NS4B, NS5 (**Figure 1.5**)[291-294]. Highly conserved amongst *Flaviviridae* family members despite the lack of extensive sequence homology are stable secondary structures that are part of the 5' and 3'-untranslated regions (UTRs) [294-297]. In addition to secondary structure predictions, RNase probing of the dengue virus 5'-UTR reveals secondary structures that are present in other *flaviviruses* suggesting a common structural arrangement of the 5' terminal region (5'-TR) [298,299]. The 5'-TR region investigated in this study is of 147 nucleotides length (nucleotides 1 to 146 from the 5' end) (**Figure 1.5**). The 5'-TR includes the 5'-UTR and its immediate downstream region, is comprised of three stem-loops (SLI, SLII, and SLIII), of which SLII contains the translation AUG start codon for polyprotein translation. RNAse probing experiments supported these predicted secondary structures [296]. Furthermore, WNV NS5, a methyltransferase, binds specifically to the 5'-SLI of genomic RNA, which is essential for viral replication [296]. RNAse probing of the dengue virus 5'-UTR demonstrated the presence of a stable secondary structure in SLA that is equivalent to SLI in 5'-TR of WNV,

suggesting a common structural arrangement of the region amongst flavivirus family members [298,299].

The 3' terminal region RNA (3'-TR RNA, nucleotides -1 to -111) is the distal part of the long 3'-UTR of flaviviruses. The 3'-TR RNA are predicted to form two stem loops those comprise its terminal 96 nucleotides (**Figure 1.5**) [300]. The sequence between -1 to -78 forms the terminal longer stem loop (3'-SL) and that from -79 to -96 forms a short stem loop (3'-SS)[296,301]. These predicted secondary structures in WNV and have been supported to partially by RNase probing and NMR data [296,301,302]. Recent work has established that both the 5'-TR and 3'-TR RNA of WNV and other *flaviviruses* is necessary for translation initiation and minus strand RNA synthesis [303-305].

1.2.5.2 Terminal region RNAs are necessary for genome cyclization

Genome cyclization through creation of a panhandle structure in many flavivirus genomes, including WNV, is possible through two regions in 5'-TR that form base pairing with respective complementary region in 3'-TR [296,303-307]. Cyclization is mediated by the 5'-upstream initiation AUG region (5'-UAR) and the 5'-conserved sequence (5'-CS) base pairing with their respective complimentary regions in the 3'-TR (3'-UAR and 3'-CS) (see underlined sequences in **Figure 1.5A and 1.5B**) [296,308,309]. Recruitment of replication factors, including the viral RNA dependent RNA polymerase, required for minus-strand RNA synthesis, is possible through this panhandle formation. Through complementary base pairing between

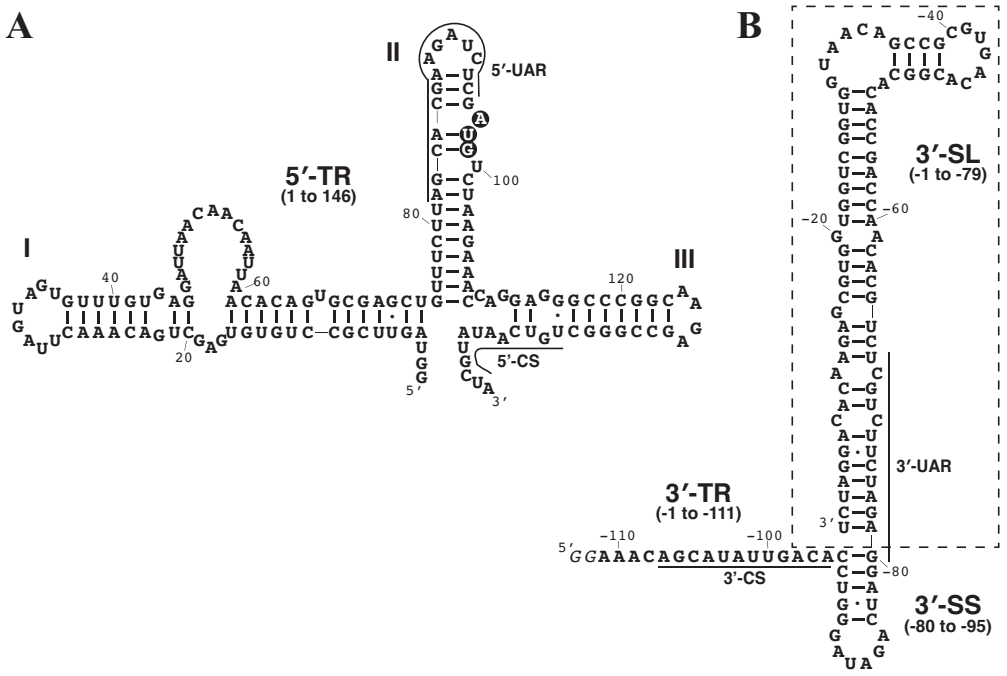

C

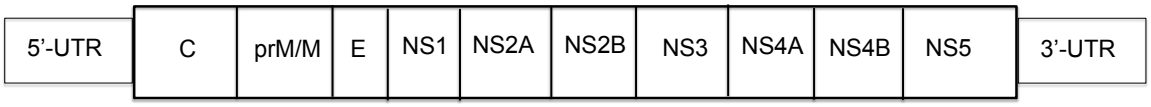

Figure 1.5 Secondary structure of Terminal region RNAs of WNV genome. A. Schematic presentation of the 5' terminal region of WNV (with extra G at the 5' followed by nucleotides 1 to 146 of 5' end of viral genome). **(B)** The 3' terminal regions of WNV (with extra GG at the 5' followed by nucleotides -111 to -1 at the 3' end of the viral genome). The dashed line box shows the part of 3'-TR (nucleotides -111 to -1) that is labeled as 3'-SL (nucleotides -1 to -79). The smaller stem loop 3'-SS is constituted of nucleotides from -80 to -95. The complementary regions in 3' and 5'-TR is underlined. The initiation codon in 5'-TR is represented in bold white alphabets. **(C)** Schematic representation of the WNV genome showing the UTRs and the protein coding regions (coding for the structural: C, prM/M, E and non-structural: NS1, NS2A, NS2B, NS3, NS4A, NS4B and NS5 proteins)[291-294]. Deo, S. et al (2015) J. Structural Biol. doi:10.1016/j.jsb.2015.04.005

the 5' and 3'-TR the genome cyclization, these replication factors forms a functional replication complex [303-305]. The 3'-SL binds to cellular eukaryotic elongation

factor 1A, which co-localizes to replication complexes with the viral non-structural proteins NS3 (a helicase) and NS5 (a RNA dependent RNA polymerase), all of which is important for viral genomic RNA replication [310,311]. The NS5 protein was also previously shown to bind to the SLI of 5'-TR [296]. Other cellular proteins including the poly A binding protein binds to the 3'-SL, whereas the La protein (a ubiquitous eukaryotic protein involved in RNA stabilization) has been shown to interact with both 5' and 3'-TR [312-314]. Therefore, a variety of proteins have been demonstrated to interact with both the folded individual terminal regions of the RNA and the cyclized versions in which these regions are base-paired. The 5' end of WNV genome and other *flavivruses* have a type 1 cap (m^7GpppAmp where m^7 stands for methyl group at *N*-7 position of guanosine triphosphate represented as Gppp where p is a phosphate group, Amp represents an adenosine monophosphate usually methylated at 2'-*O*). This cap along with various cellular and viral protein factors are brought together due to the genome circularization are thought to enable cap dependent negative strand synthesis possible [315].

1.2.6 RATIONALE FOR THE THESIS: LINKING OAS1 WITH WNV

Several PRRs are important antiviral restrictions factors against WNV infections. Mouse models lacking IFN α and β-receptors have demonstrated the importance of IFN response against WNV infection [316]. Mice devoid of active TLR3 and TLR7 are highly susceptible to WNV infection in comparison to the wild type mouse [94,317]. Furthermore, the RIG-I and MDA5-dependent antiviral response against WNV and DENV have been reported [109,318]. PKR plays an important role in innate antiviral

immunity against WNV attenuating viral spread and replication [175]. Having summarized a range of IFN mediated innate immune response against WNV here, its noteworthy that WNV is capable of countering these antiviral activities, which enables its successful invasion of host cells. Although the mechanism has yet to be discovered, the NS2A protein of Kunjin virus (a less pathogenic subtype of WNV) acts as a transcriptional inhibitor of the *IFN-β* gene [319]. Less pathogenic strains of WNV induce effective IFN levels, but highly pathogenic WNV strains evolve to evade the IRF-3 dependent recognition pathway and/or delay recognition by RIG-I, thus giving the virus an advantage in initial phase of its infection [320,321]. The WNV NS1 protein executes its inhibitory effect on transcription of IFN-β and IL-6 (an important pro-inflammatory cytokine) including attenuation of NFkB promoters by inhibiting TLR3 induced translational pathways [322]. Viral dsRNAs can lead to expression of interferon and cytokines like IFN-β and IL-6 and TNF-α. It has been suggested that the viral E protein, rich in mannose carbohydrate, may inhibit the expression of these IFNs and cytokines [323]. These viral countermeasures may explain why there is a small time window for effective treatment with interferon therapy, as mice treated with IFN-α after 2 days of WNV infection fail to respond to the treatment [324,325]. The same study showed that if mice were given IFN-α before they are challenged with WNV, the mice had a better antiviral response and reduced mortality rate [324,325]. HCV, another member of family *Flaviviridae*, counters the host IFN response through the NS5A protein [326]. HCV NS5A binds to OAS and prevents its interaction with dsRNA PAMPs, giving the virus countermeasures to the OAS/RNase L pathway. In addition, IFN-α resistant HCV

strains have less UU and UA di-nucleotides in their mRNA, which may suggest fewer target sites for active RNase L [326,327].

RNase L, the effector protein in OAS/RNase L pathway, plays an important role in the interferon-mediated antiviral response against WNV, as mice with RNase L (−/−) genotype show much higher susceptibility to viral infection [175]. In horses, SNPs in both the *OAS1* gene and *RNase L* gene have been implicated in higher susceptibility to WNV [328]. Recently, an OASL homologue in chicken was reported to impart resistance against WNV [329]. OAS1 and other OAS isoforms are able to reduce flavivirus titers in mouse brain by 99% [330]. The antiviral effect of OAS proteins have also been demonstrated against picornavirus, which has a positive ssRNA genome similar to WNV [241]. Two different single nucleotide polymorphisms (SNPs) in the *OAS1* gene have been reported to be host genetic risk factor in humans in initial phase of infection with WNV [331,332]. Four different SNPs in OAS1 have been implicated in susceptibility and severity of disease progression in hand, foot and mouth disease mostly caused by strains of human enterovirus and coxsackievirus, both of which are ssRNA +ve (sense) strand viruses like WNV [333].

OAS1 has been shown to reduce WNV infection by restricting the ability of WNV to accumulate viral RNA [334]. Human OAS1 isotypes p42 and p46 have been shown in human cell lines to block viral replication of Dengue virus, which belongs to family *Flaviviridae.* Antiviral effects of these OAS1 isotypes are accomplished in an RNase L-dependent manner [244]. Based on these results we hypothesize that in human antiviral response to WNV infection has strong links with the host OAS1.

The 5' and 3'-TR of WNV interacts with viral and cellular proteins including NS5, La protein and eukaryotic elongation factor 1A(eEF1A) [291-296]. These interactions are imparted by the stable secondary structures within these UTRs. Furthermore, these UTRs are recognized by RIG-I thereby enabling induction of antiviral response [258]. OAS1 has been linked to the antiviral response against WNV; however how OAS1 is induced or activated has not been fully elucidated.

Because of the presence of stable secondary structures in the TR RNAs of the WNV genome and the link between OAS1 and WNV infection, I hypothesized that the 5' and 3'-TR of WNV include regions that can bind to and activate OAS1 [294-297,331,332]. I first investigated whether the 5' and 3'-TR RNAs of WNV interact with and activate human p42 OAS1. Using a deletion analysis approach, I found minimal regions within the 5' and 3'-TRs to interact and activate OAS1. As it has been already mentioned that the 5' and 3'-TR regions of WNV can interact to induce cyclization [296,303-307], I investigated the biophysical aspects of this interaction. The interaction between the 5' and 3'-TR is investigated to measure their binding affinity using isothermal titration calorimetry (ITC) and also the stability of the secondary structures represented by its melting temperature is compared with the individual TRs. The results obtained may explain the spontaneity of the interaction between the TR RNAs. Although the importance of the CS region of 3'-TR on the 5'-TR/3'-TR complex formation have previously been reported [303,304], it was reconfirmed with truncated 3'-TR missing the CS region that failed to demonstrate RNA complementary base pairing both on an EMSA and ITC. The absence of any detectable interaction between the 3'-SL with the 5'-TR may be because of changes

in the binding thermodynamics. An OAS1 SNP, S162G, previously reported to be prevalent in WNV infected patients, was also tested to demonstrate any effect of the SNP on OAS1 activation in the presence of dsRNA activators of the WNV genome [335]. To verify whether the interaction of the activating 5'-TR of WNV with OAS1 is through the RNA binding region of the enzyme, two OAS1 mutants were tested, each with a point mutation, mutating either R195 or K199 to glutamic acids. These residues reside in the RNA binding region and their mutation had a deleterious effect of enzyme activation [217,222]. Structural information on the terminal region RNAs including their truncations and RNA-OAS1 complex were obtained, mainly through the use of small angle X-ray scattering (SAXS). We made attempts to confirm these interactions in mammalian cells.

1.2.7 FRAMEWORK OF THE THESIS

In the introductory section, I have focused on outline innate immunity, IFN response, PRRs and their ligand preference. I made an attempt to link WNV infection to OAS1 and rationale why terminal regions of WNV genome are likely candidates to activate OAS1. In Chapter 2, details of materials and methods used during my work on this project are presented. The results obtained are in Chapter 3 and 4, which includes findings published in two peer-reviewed articles and some unpublished preliminary data. The thesis will then proceed with Chapter 5 on discussion and future directions. In this final chapter, an attempt has been made to rationalize the results obtained, highlight contributions made to our knowledge on viral dsRNA ligands of OAS1 in the WNV genome.

CHAPTER 2: MATERIALS AND METHODS

2.1 INTRODUCTION

Investigating how the 5' and 3'-terminal regions of WNV interact with OAS1 (p42 isoform) is the main goal of my research. It is unknown whether the terminal regions are capable of OAS1 activation and the minimal region required for it. The links between susceptibility to WNV infection and OAS1 has been discussed (Chapter 1) [330-332]. I decided to select one of the human OAS1 isoforms and optimize its expression and purification. Amongst all the human OAS1 isoforms (p42, p44, p46, p48 and p52) possible through alternative splicing, we decided to focus our research on p42 as it's the smallest and is an active adenylate synthetase [244,336]. In addition, active p42 could be expressed and purified from bacterial cells, which could not provide required post-translational modifications for larger OAS isoforms (OAS2 and OAS3) [184,185,224,337]. Once a sufficient amount (~ 2 mg/Liter of LB culture) of OAS1 p42 was purified, which is very cost-effective and high-yield, my focus was directed towards production and purification of the 5' and 3'-TR RNAs, as well as logically designed truncations. All RNAs used were produced through *in vitro* transcription and purified using a size-exclusion chromatography (SEC). Although the detailed protocol for this non-denaturing RNA preparation method has been discussed elsewhere, I have included a thorough description of the specific method used in this chapter [338].

The binding affinities of the transcribed RNAs and OAS1 were analyzed using electrophoretic mobility shift assays. Biophysical characterization of the RNAs,

protein, RNA+RNA and protein+RNA complexes were performed using dynamic light scattering (DLS), analytical ultracentrifugation (AUC) and isothermal titration calorimetry (ITC). Solution conformation of these biomolecules and their complexes were investigated using small angle X-ray scattering (SAXS). Enzyme kinetics of OAS1 in presence of terminal region RNAs and their truncations were performed using a non-radioactive, colorimetric assay to quantify the enzyme activity by tracking the amount of pyrophosphate (PPi) produced. Finally, efforts were made to demonstrate, in mammalian cells, the relevance of OAS1+RNA complexes using pull-down assays with biotinylated RNA, real time PCR (RT-PCR) and cross-linking of RNA-OAS1 complexes.

The initial part of this chapter is focused on the expression and purification of samples followed by the methods used in RNA-protein binding and activation/kinetics studies. Next, I discuss major techniques used to validate the quality of samples before investigating the solution conformation using SAXS. SAXS is a major part of this thesis and it was a technique of choice because it doesn't require samples to be in crystal form, which is usually cumbersome and is a solution technique that allows sample flexibility. SAXS was utilized to generate low-resolution three-dimensional structural information on the terminal regions of the WNV genome and its interactions with OAS1, I have included a detailed section on SAXS to include the principles behind it and how different software programs are used in scattering data analysis. The last part of this chapter describes materials and methods in mammalian cell culture and related techniques, which were employed in an attempt to validate the *in vitro* interactions demonstrated in thesis

in mammalian cells.

2.2 REAGENTS

All standard laboratory chemicals of molecular biology grade were obtained from three companies: Sigma-Aldrich (Oakville, ON), Fisher Scientific (Ottawa, ON) and EMD (affiliated with Merck, Gibbstown, NJ, US). Specific chemicals used in any preparation and experimentation has been included in their respective sections. Buffers were prepared using deionized ultra-purified water (MiliQ, EMD Milipore, affiliated to Merck, ON, Canada).

2.3 EXPRESSION AND PURIFICATION OF PROTEIN

2.3.1 EXPRESSION AND PURIFICATION OF OAS1 IN *E. Coli*

We optimized the expression and purification of human OAS1 (isoform p42) in BL21-CodonPlus(DE_3)-RIL *E. coli* cells. *E. Coli* systems have well known advantages of easy handling, shorter time frame and higher yield. To reduce the codon bias effect on target human protein expression, the BL21-CodonPlus (DE_3)-RIL *E. coli* cells express tRNA genes rarely found in *E.coli* cells but used with high frequency in human cells (Agilent technologies, Mississauga, Ontario, Canada). The human *OAS1 tv2* coding sequence (NCBI Reference Sequence: NP_002525.2) was inserted into a non-commercially available modified pET30a(+)-GNSHT vector that encodes a fusion protein containing, from N-terminus to C-terminus, G: the B1 immunoglobulin binding domain (GB1) from protein G of *Streptococcus* [339], N:

transcription termination anti-termination factor (NusA) from *E. coli* [340], a streptavidin tag (S), an 8XHis tag (H), a TEV (tobacco etch virus) protease site (T) followed by the *OAS1 tv2* coding region. The GB1 and NusA protein helps improve the solubility of OAS1, decreasing the chance of inclusion body formation [341]. Although the mechanism of solubility enhancement by GB1 and NusA, is unclear it is hypothesized that they may act as chaperones, promoting folding and preventing aggregation of partially folded proteins, or they form micelle-like structure thereby sequestering misfolded and unfolded proteins from solvent interactions and allowing an outward presentation of soluble domain face [342]. Streptavidin and 8XHis tags allow affinity purification from cell lysate through use of either a biotin or nickel-affinity column. I used a Ni-Nitrilotriacetic acid (Ni-NTA) column (GE Healthcare) with 5 mL column volume in our purification of GNSHT-OAS1 fusion protein [343]. Before a size exclusion chromatography (SEC), the tagged-OAS1 was cleaved by an in-house purified tobacco etch virus (TEV) protease.

Figure 2.1 Schematic representation of OAS1 *tv2* gene sequence with the GNSHT tag.

This protease targets the TEV protease recognition site (E-N-L-Y-F-Q-S), which is present preceding the OAS1 [344]. The yield for purified soluble OAS1 eluted from the SEC column per liter of LB broth is approximately 2.0 mg. Mutant versions of OAS1 (described in section 1.2.6) were also purified following exactly the same

steps as the wild type OAS1. Steps involved in site directed mutagenesis to generate construct for these mutated versions are described in section 2.3.3.

2.3.2 PROCEDURES

The steps involved in the *in vitro* transcription reaction is as follows:

2.3.2.1 Construction of OAS1expression vector (pET30a(+)-GNSHT-OAS1)

The *OAS1 tv2* gene on the plasmid pOTB7 (Open Biosystems) was PCRamplified using the following primers:

1. 5'OAS1-GNSHT:(GCGCGCGCGTCGACATGATGGATCTCAGAAATACCCCAGCCAA
2. 3'OAS1-GNSHT:(GCGCGCGCGCGGCCGCTCAAGCTTCATGGAGAGGGGCAGGGAT GAATGGCAGGGAGGAAGCAGG).

The PCR conditions are as follows:

1. Initial denaturation step at 98°C for 3 min
2. 34 cycles of three sub-steps: (i) 95°C for 30 seconds
   (ii) 55°C annealing temperature for 30 seconds
   (iii) 72°C extension step for 1 minute
3. Final step of 72° C for 5 minutes

The amplified PCR product was ligated into a pET30a(+)-GNSHT vector, a modified version of pET30a(+) plasmid vector that was a gift from Dr. Tinghe Wu, Stanford University. Both the vector pET30a(+)-GNSHT and the PCR amplified insert were treated with NotI and SalI restriction enzymes (RE) from New England Biolabs and the restriction digestion was performed in presence of 1X RE buffer supplied by the manufacturer. The restriction digested inserts were subjected to GeneJET PCR

cleanup kit (Thermo scientific). Then restriction-digested plasmid was run on a 1% agarose gel loaded with the samples and run at 80V, the appropriate bands were visualized under UV light and excised carefully using a clean razor. DNA from the cut bands imbibed in the gel was purified using GeneJET gel purification kit (Thermo scientific). Purified insert (PCR amplified construct) and the vector (pET30a(+)-GNSHT) were mixed in 3:1 molar ratio in a 20 µL reaction (total DNA concentration is kept below 10 µg/mL) along with T4 DNA ligase (New England Biolabs, Whitby, ON, Canada).

2.3.2.2 Expression of GNSHT-OAS1 fusion protein

Transformation of pET30a(+)-GNSHT and *OAS1 tv2* ligation reaction into XL-10 gold competent cells (Stratagene, now Agilent Technologies, Mississauga, ON, Canada) was performed and then cells were plated on Luria–Bertani (LB) agar plate with kanamycin and chloramphenicol at 30 µg/mL and 20 µg/mL concentrations respectively. The competent cells are chloramphenicol resistance and transformation with pET30a (+)-GNSHT vector confers resistance to kanamycin. Individual colonies were picked and grown overnight in LB media with kanamycin (30 µg/mL) and chloramphenicol (20 µg/mL) in an incubation shaker at 200 rpm. Minipreps (GeneJET miniprep kit, Thermo Scientific) plasmid preparation was performed and sent for sequencing at MICB. Once the integrity of the inserted *OAS1 tv2* sequence was confirmed the pET30a(+)-GNSHT-*OAS1 tv2* plasmid was transformed into BL21-CodonPlus(DE_3)-RIL competent *E. coli* cells. A single colony from an LB agar plate containing chloramphenicol and kanamycin at concentrations

mentioned before was inoculated into a starter culture (10 mL of LB liquid broth with concentration of kanamycin at 30 μg/mL and chloramphenicol at 20 μg/mL) and was grown overnight at 37°C in a incubator shaker (200 rpm). After the overnight growth (typically 14-16 hours), 10 mL of the starter culture was added to a 1 liter of LB (in a 4 liter Erlenmeyer flask) supplemented with the same antibiotics and grown at 37°C until optical density at 600 nm (OD600) value reached 0.6-0.8. Once the desired OD is reached the Erlenmeyer flask was cooled on ice for 15 minutes followed by addition of inducing reagent, isopropyl-β-D-thio-galactopyranoside (IPTG) to a final 1 mM. The culture is then incubated in incubator shaker at 200 rpm and the temperature was maintained at 20°C overnight for expression of the fusion protein.

2.3.2.3 Isolation of GNSHT-OAS1 fusion protein

The overnight culture was subjected to centrifugation in a Thermo Scientific™ Sorvall™ centrifuge at 6,000g for 15 min (4°C) and the cell pellet was resuspended in resuspension/lysis buffer (50 mM Tris, 1M NaCl, 1 mM imidazole, 5% glycerol and 1 mM DTT, pH 7.5). The cells were lysed by sonication (20s pulses at 30s intervals for 10 cycles) during which the sonication container was kept on ice. The sonication is followed by centrifugation at 40,000 g for 40 min at 4°C (Thermo Scientific™ Sorvall™ centrifuge). The supernatant was carefully transferred without disturbing the pellet, into dialysis tubing with a 10 kDa cut-off and dialyzed in wash buffer (50 mM Tris, 1 M NaCl, 25 mM imidazole, 5% glycerol and 1 mM DTT, pH 7.5) at 4°C. The supernatant of the cell lysate was then loaded onto a pre-packed Ni–NTA

[5 mL column volume (CV), QiaGen Inc.] that has been equilibrated with wash buffer. Wash buffer (25 CV) was passed through the column to remove the non-specifically bound proteins. GNSHT-OAS1 fusion protein was eluted in 5 mL fractions by using the elution buffer (50 mM Tris, 300 mM NaCl, 200 mM imidazole, 5% glycerol and 1 mM DTT, pH 7.5). The eluate fractions were checked for presence of protein by using Bradford reagent. All fractions that showed presence of protein were checked by 8% sodium dodecyl sulfate polyacrylamide gel electrophoresis (SDS-PAGE). Purified GNSHT-OAS1 protein mainly elutes in first 4 fractions.

2.3.2.4 Cleaving the GNSHT tag and final purification step using SEC

Post affinity chromatography eluate fractions with purified fusion protein (GNSHT-OAS1) were pooled and dialyzed against TEV protease working buffer (50 mM Tris, 50 mM NaCl, 1 mM EDTA, 5% glycerol and 1 mM DTT, pH 7.5) at 4°C. The proteolytic cleavage of the GNSHT tag was performed by overnight (12-14 hours) incubation at room temperature in the dark with the in-house TEV protease. An 8% SDS-PAGE analysis was performed to confirm the cleavage of the GNSHT tag. This is followed by dialysis of the eluate at 4°C against size exclusion chromatography (SEC) buffer (50 mM Tris, 100 mM NaCl and 1 mM DTT, pH 7.5). The SEC system was assembled with a Fac-950 fraction collector and an UNICORN 6 control software (GE Healthcare) as the user interface on a dedicated computer. The SEC (ÄKTA Purifier 10 system) with HiLoad Superdex 200 column (26/60, GE Healthcare) housed in a freeze to keep the temperature at 4°C, is also equilibrated with SEC buffer. After the dialysis of eluate in SEC buffer, the OAS1 eluate injected

A

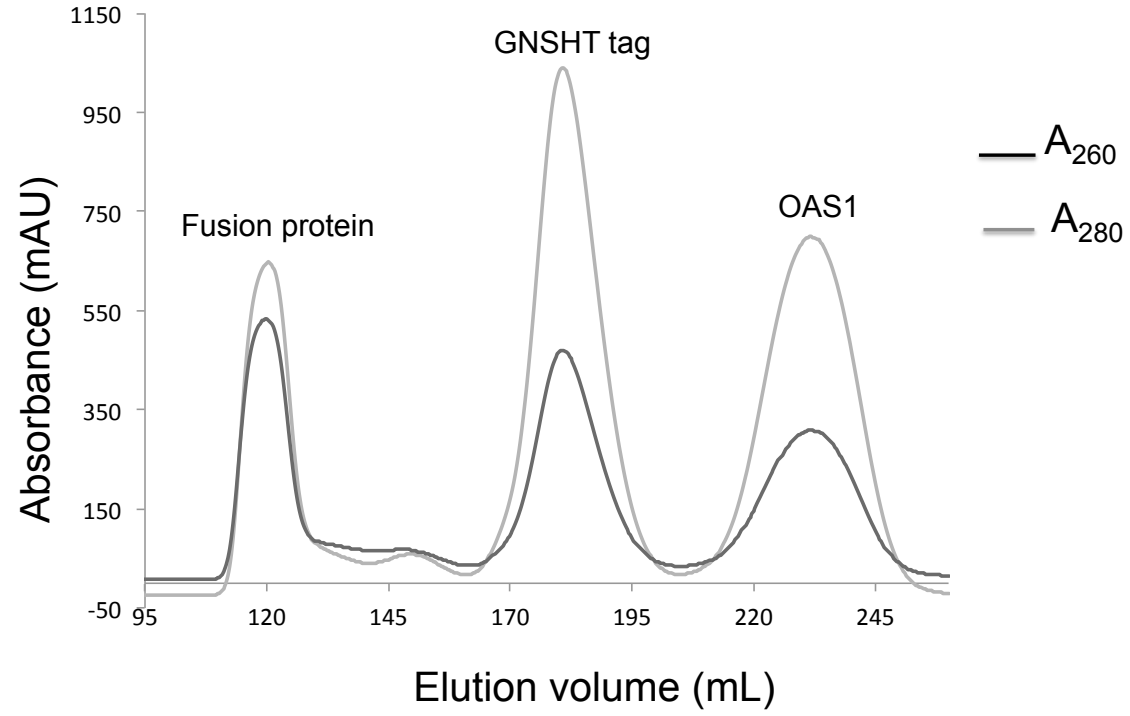

B

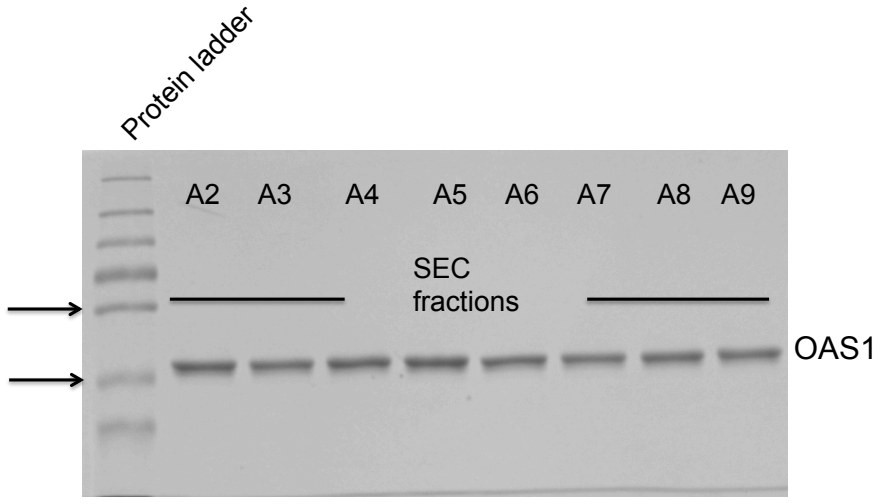

Figure 2.2 Final purification step of OAS1 and visualization of purity. (A) SEC elution profile of GNSHT-OAS1 fusion protein after TEV protease digestion. **(B)** SDS PAGE showing 5 mL OAS1 fractions (A2 to A9) collected from SEC.

onto the SEC column and the chromatography was performed at 2 mL/minute. A typical elution profile of OAS1 is presented in **Figure 2.2A**. The first peak (peaks at 120 mL) corresponds to the RNA bound protein and the fusion protein (GNSHT-OAS1 tv2), the second peak (peak at 165 mL) is the elution of cleaved GNSHT tag and the third peak (peak at 230 mL) is the cleaved OAS1. 5 mL fractions from each peak were collected and subjected to 8% SDS-PAGE to check for purity. **Figure 2.2B** shows pure OAS1 fractions eluted in the third peak. The OAS1 band runs between the bands of protein ladder with molecular weights of 55 kDa and 35 kDa, consistent with its molecular weight of 42 kDa.

2.3.3 SITE DIRECTED MUTAGENESIS OF OAS1

Point mutations were introduced using primers ordered from Integrated DNA technologies (IDT, Coralville, Iowa, US). The primers are listed below.

A484G (sense): 5'-GGGTCAGTTGACTGGCGGCTATAAACCTAACCC-3'

A484G (antisense): 5'-GGGTTAGGTTTATAGCCGCCAGTCAACTGACCC-3'

A583G_G584A (sense): 5'-CTGCTTCACAGAACTACAGGAAGACTTCCTGAAGCAGCGC-3'

A583G_G584A (antisense): 5'-GCGCTGCTTCAGGAAGTCTTCCTGTAGTTCTGTGAAGCAG-3'

A595G_G597A (sense): 5'-CAGAGAGACTTCCTGGAACAGCGCCCCACCAAG-3'

A595G_G597A (antisense): 5'-CTTGGTGGGGCGCTGTTCCAGGAAGTCTCTCTG-3'

These primers incorporated the desired mutations in OAS1 by changing the indicated coding sequence as follows:

A484G: serine162 to glycine

A583G_G584A: arginine195 to glutamic acid

A595G_G597A: lysine199 to glutamic acid

Site directed mutagenesis of pET30a (+)-GNSHT vector was performed using the Quikchange Lightning site-directed mutagenesis kit (Stratagene, now Agilent Technologies, Mississauga, ON, Canada), with minor changes to the manufacturer's protocol. The denaturation time was 3.5 minutes. Following site-directed mutagenesis, the reaction product was transformed into XL10-Gold Cells (chemically competent *E.Coli,* Stratagene). The bacteria were plated onto LB agar plates containing both antibiotics kanamycin at 30 µg/mL and chloramphenicol at 20 µg/mL. Few of the individual colonies on each plate were grown in a 2 mL LB broth with the above-mentioned antibiotics at same concentrations and the plasmids were purified using miniprep kit and confirmed by sequencing at Manitoba Institute of Cell Biology (MICB). The mutated OAS1 proteins were expressed and purified adhering to the protocol optimized for OAS1.

2.4 *IN VITRO* TRANSCRIPTION OF RNA

A schematic flowchart below summarizes major steps involved in *in vitro* transcription (**Figure 2.3**).

2.4.1 PROCEDURE

The steps involved in *in vitro* transcription of RNA is as follows:

2.4.1.1 Plasmid isolation

Based on the amount of plasmid required, four different preparatory kits and respective manufacturer's protocol was followed. Depending on the amount of plasmid required, four different kits were used: Genejet plasmid miniprep kit (#K0503, Thermoscientific, Pittsburg, PA, US), Genejet plasmid midiprep kit (#K0481, Fermentas life sciences, Thermoscientific, Pittsburg, PA, US), Qiagen plasmid maxi kit (# 12162) and Qiagen plasmid Giga kit (# 1291, Toronto, ON, Canada).

2.4.1.2 cDNA amplification

Single-stranded DNA templates (cDNA) (from IDT, US) were designed as follows: (PCR extension)(HindIII)(T7 promoter)(RNA sequence of interest)(BsaI site)(EcoRI site)(PCR extension). The specific nucleotide sequences are as follows: (GCGC) (AAGCTT) (AATACGACTCACTATA) (RNA sequence of interest) (XGAGACC) (GAATTC)(GCGC).

Primer (*Forward*): 3' GCGCAAGCTTAATACGACTCACTATAGG 5'

Primer (*Reverse*): 5' GCGCGAATTCGGTCTCC 3'

The forward primer complementary to the template strand and the reverse primer complementary to the coding strand enable amplification of dsDNA template (insert), which is ligated into suitable plasmid vector. Plasmid constructs for transcription of WNV (strain: NY99iso-1) TR RNAs and their truncation mutants were purchased (IDT). **Figure 2.3** represents (PCR extension)(HindIII)(T7 promoter)(RNA sequence of interest)(BsaI site)(EcoRI site)(PCR extension) sites highlighted in grey boxes. Secondary structures and schematic representation of

these terminal region RNAs and their truncation have been included (section 1.2.5.1, **Figure 1.5A, 1.5B**). The ssCCHF (a randomized ssRNA sequence from Crimean-Congo haemorrhagic fever virus) is an ssRNA transcribed and purified to serve as a negative control to validate that no unintended by-products of the transcription reaction were leading to activation. PCR was performed using the Phusion High-Fidelity DNA Polymerase (Thermo scientific).

5'-TR (includes an additional G at the 5' end for T7 optimization)(nucleotides 1 to 146): GCGCAAGCTTAATACGACTCACTATAGGTAGTTCGCCTGTGTGAGCTGACAAACT TAGTAGTGTTTGTGAGGATTAACAACAATTAACACAGTGCGAGCTGTTTCTTAGCACGA AGATCTCGATGTCTAAGAAACCAGGAGGGCCCGGCAAGAGCCGGGCTGTCAATATGCTA GGAGACCGAATTCGCGC

5'-TR stem loop I (includes an additional G at the 5' end for T7 optimization) (nucleotides 1 to 73): GCGCAAGCTTAATACGACTCACTATAGGTAGTTCGCCTGTGTG AGCTGACAAACTTAG TAGTGTTTGTGAGGATTAACAACAATTAACACAGTGCGAGCTG GAGACCGAATTCGCGC

5'-TR stem loop II (includes an additional G at the 5'end for T7 optimization) (nucleotides 73 to 110): GCGCAAGCTTAATACGACTCACTATAGGTTTCTTAGCACGAA GATCTCGATGTCTAAGA AACCGGAGACCGAATTCGCGC

5'-TR stem loop III (including an additional G at the 5' end for T7 optimization)(nucleotides 111 to 146): CGCAAGCTTAATACGACTCACTATAGGAGGG CCCGGCAAGAGCCGGGCTG TCAATATGCTAGGAGACCGAATTCGCGC

5'-TR stem loop I+II (including an additional G at the 5' end for T7 optimization) (nucleotides 1 to 109): GCGCAAGCTTAATACGACTCACTATAGGTAGTTCGCCTGTGT GAGCTGACAAACTTAGTAGTGTTTGTGAGGATTAACAACAATTAACACAGTGCGAGCT GTTTCTTAGCACGAAGATCTCGATGTCTAAGAAACGGAGACCGAATTCGCGC

5'-TR stem loop II+III (including an additional G at the 5' end for T7 optimization) (nucleotides 73 to 146): GCGCAAGCTTAATACGACTCACTATA GGTTTCTTAGC ACGA AGATCTCGATGTCTAAGAAACCAGGAGGGCCCGGCAAGAGCCGGGCTGTCAATATG CTA GGAGACCGAATTCGCGC

3'-TR includes an additional GG at the 5' end for T7 optimization (nucleotides -1 to -111): GCGCAAGCTTAATACGACTCACTATAGGAAACAGCATATTG ACACCTGGGATAG ACTAGGAGATCTTCTGCTCTGCACAACCAGCCACACGGCACAGTGCGCCGACAATGGTGG CTGGTGGTGCGAGAACACAGGATCTGGAGACCGAATTCGCGC

3'-SL(includes an additional G at the 5' end for T7 optimization)(nucleotides -1 to -78): GCGCAAGCTTAATACGACTCACTATAGGATCTTCTGCTCTGCACAACCAGCCACAC GGCACAGTGCGCCGACAATGGTGGCTGGTGGTGCGAGAACACAGGATCCGGAGACCGAA TTCGCGC

ssCCHF (includes an additional G at the 5' end for T7 optimization): GCGCAAGCTTAATACGACTCACTATA TCTCAAAGAAAC ACGTGCCGCTTACGCCCACAG TGTTCT GGAGACCGAATTCGCGC

Figure 2.3 Sequences of RNAs transcribed. Relevant sites at 5'/3' ends of the RNA sequence of interest (PCR extension sequence, HindIII and T7 promoter sequence at the 5' end; BsaI site, EcoRI site and PCR extension sequence at the 3' end) are shown in grey box.

Each reaction volume was 25 µL and the final primer concentrations were 400 nM. The PCR conditions are described in section 2.3.2.1. PCR reaction was performed on C1000™ Thermocycler (Biorad, Mississauga, ON, Canada). The primers enabled incorporation of desired restriction endonuclease cutting sites for HindIII and EcoRI. These restriction enzymes were used to digest the amplified construct cDNA from the PCR reaction and the pUC119 plasmid (vector). Before the restriction digestion the PCR products were purified with the GeneJET PCR purification kit (Thermo scientific) according to the manufacturer's protocol. The PCR amplified and purified cDNA construct was digested using FastDigest EcoRI and FastDigest HindIII (Thermo scientific). Restriction digestion was performed for 5 minutes at 37°C and the manufacturers protocol were followed to determine relevant amount of enzyme and 10X universal buffer (supplied with the enzyme). The universal

buffer has premixed load dye making it possible to load the digested sample onto a gel much easier. Following digestion, the cut DNA products were separated by agarose gel-electrophoresis. A 1.5% agarose gel loaded with the samples and run at 80V, the appropriate bands were visualized under UV light and excised carefully using a clean razor. DNA from the cut bands imbibed in the gel was purified using GeneJET gel purification kit (Thermo scientific).

2.4.1.3 Plasmid preparation for *in vitro* transcription

For each cloned plasmid, sequencing was performed (MICB, Winnipeg) to ensure integrity and accuracy. MAX Efficiency® DH5α™ Competent Cells (Life Technologies, Invitrogen) were transformed with purified plasmids construct verified by sequencing. Maxiprep or gigaprep protocols were followed to purify large quantity of template DNA required for *in vitro* transcription. Plasmid DNAs were linearized using BsaI restriction enzyme (NEB) at 37°C overnight to ensure complete linearization. To purify the linearized plasmids, phenol/chloroform (1:1) extraction followed by DNA precipitation with 3 M sodium acetate and ethanol precipitation was used. The precipitated DNA was centrifuged at 21000g on a tabletop centrifuge (Thermo scientific) and t pellet formed was washed with 70% ethanol to remove residual salt. DNA pellet was dissolved in HPLC-grade water to a concentration of 500 µg/mL.

2.4.1.4 Trial and large-scale transcription

Trial transcription reactions (50 µL reaction volume) were performed for optimization of reaction conditions before performing a higher yield large-scale

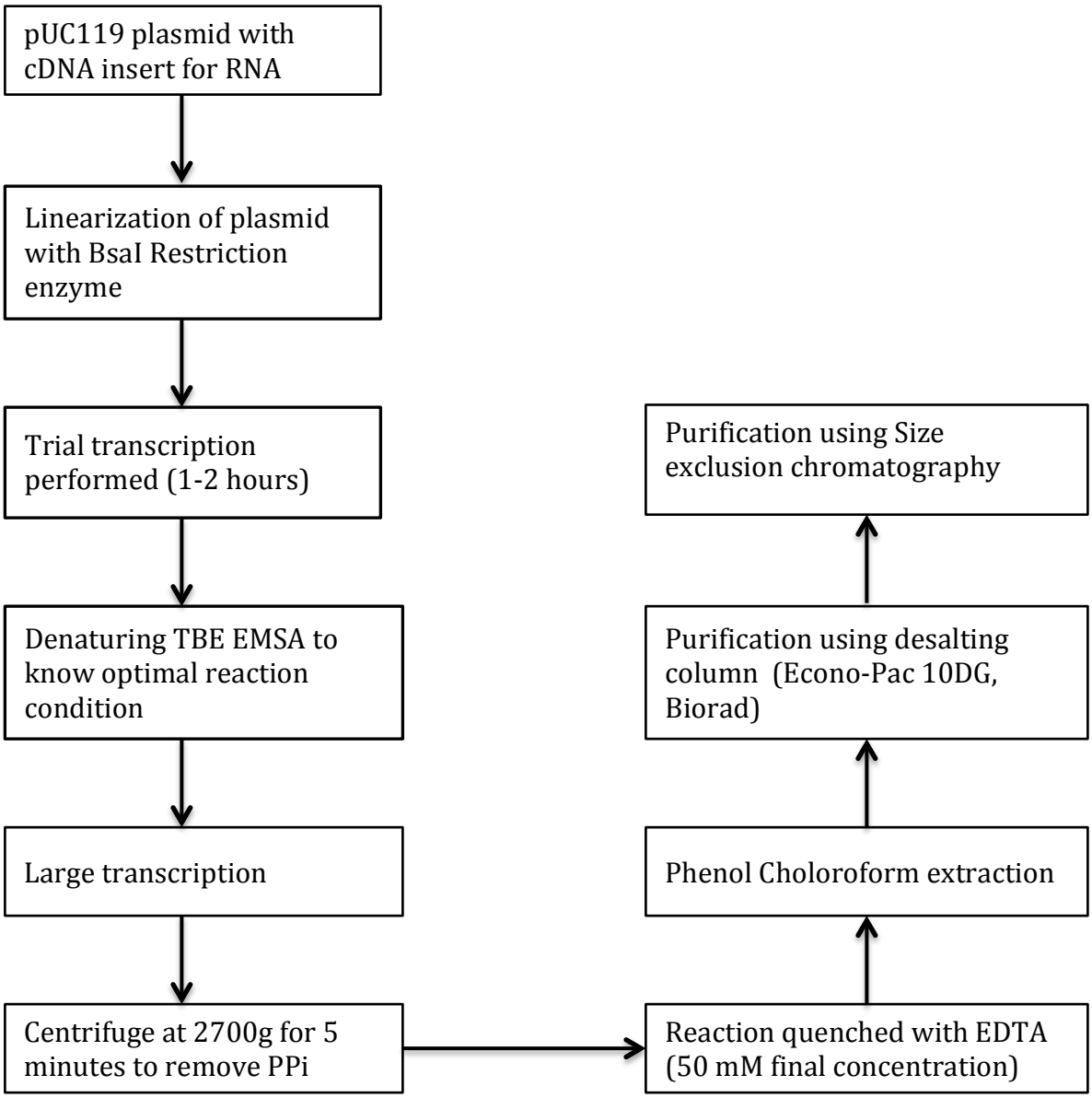

Figure 2.4 Flow chart of major steps involved in *in vitro* transcription.

in vitro transcription reactions. The amount of T7 RNA polymerase (produced in-house) and the relative NTP:$MgCl_2$ concentration was optimized for maximal transcription efficiency. A typical small-scale trial transcription reaction was contains the following:

1. 1x transcription buffer (40 mM Tris, pH 8.1; 1 mM spermidine, 0.001% (wt/vol) Triton X-100, 10 mM DTT in HPLC water),
2. 8 mM NTPs (2 mM each),
3. 2.5 µg linearized DNA template,
4. $MgCl_2$ (between 5 to 20 mM),
5. T7 RNA polymerase (0.5,1.0 or 2.0 µL)

The transcription reaction was analyzed on a denaturing Tris, boric acid, EDTA (TBE)-polyacrylamide gel electrophoresis (PAGE) containing 8M Urea to denature secondary RNA structures. RNA samples were mixed with denaturing loading buffer [0.02% bromophenol blue, 0.01% xylene cyanol FF, 10% glycerol, 8 M Urea in]. The samples with loading dye were heated at 95°C for 5 min before loading them onto the TBE gels and the PAGE was performed at 150V in 1XTBE in a mini-protean 3 cell (Biorad, Mississauga, ON, Canada).

To visualize RNA, the gel was stained in 0.1% toluidine blue solution for at least 5 min and then distained in water with shaking. The optimal trial transcription conditions were scaled up to the desired size and incubated for 2 to 3 hours at 37°C. Pyrophosphate (PPi)-$MgCl_2$ precipitate is produced as a byproduct, which is separated by centrifugation at 2700g for 5 minutes. The transcription reaction supernatant is transferred carefully to a fresh tube leaving the PPi-$MgCl_2$

precipitates undisturbed. The reaction was quenched by chelation of excess Mg^{2+} by

A

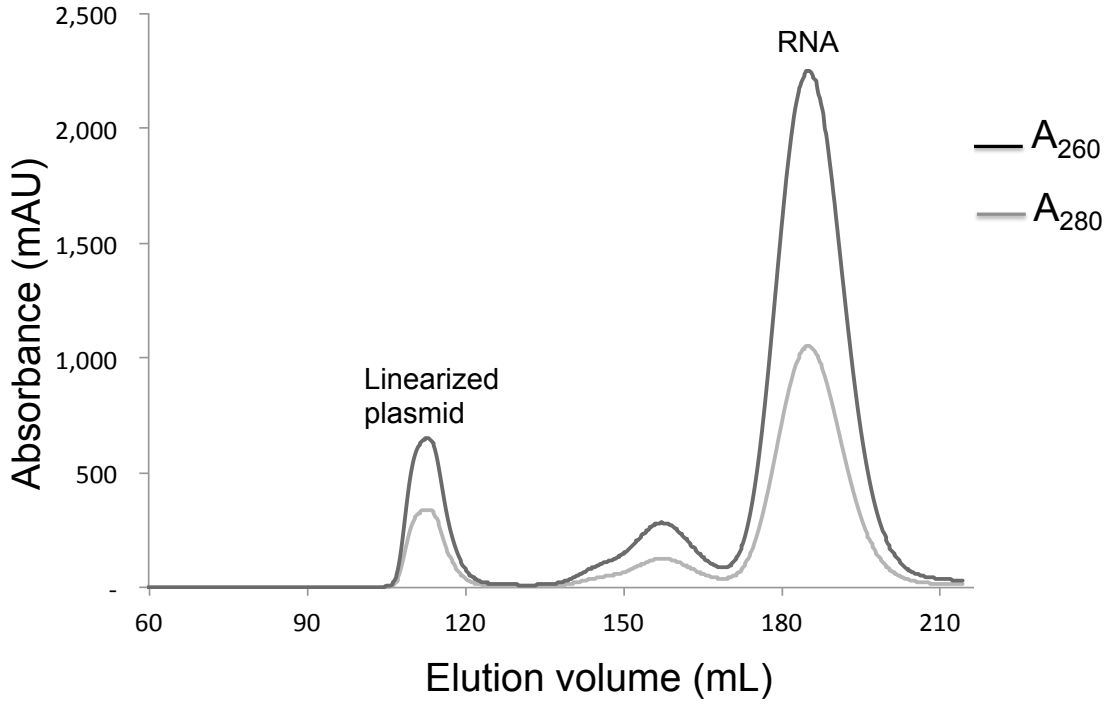

B

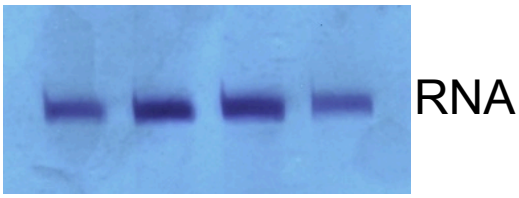

Figure 2.5 SEC purification of RNA and TBE-PAGE to visualize purity (A) SEC elution profile of *in vitro* transcribed RNA purification where linearized plasmid and monomer RNA peaks are labeled here. **(B)** TBE-PAGE of four fractions collected under the monomer RNA peak.

adding EDTA, pH 8.0 (10% of the reaction volume of 500 mM EDTA added) to a final concentration of 50 mM with thorough mixing. The mixture was then subjected to phenol/chloroform/isoamyl alcohol (25:24:1) extraction to denature and remove

T7 RNA polymerase. RNA transcript was next purified using 10-DG desalting column (BioRad) to remove traces of phenol/chloroform and large portion of small molecule contaminants (salts and NTPs). The protocol for 10-DG column purification step involved an equilibration step with 20 mL RNA buffer (50 mM Tris, pH 7.5, 100 mM NaCl). 3 mL of the transcription reaction was then applied to the column and eluted with 5 mL of RNA Buffer (50 mM Tris, 100 mM NaCl, pH 7.0).

Transcribed RNA was then isolated using size exclusion chromatography (SEC). SEC removes residual DNA template, aborted transcripts and excess small molecules thereby allowing high quality pure RNA to be purified as a single peak. The fractions under the peak corresponding to the transcribed RNA were collected and denaturing TBE-PAGE was performed to confirm purity (**Figure 2.5**). The small molecules (mostly unused NTPs) are eluted typically after an elution of volume of 270 mL.

2.5 PURIFICATION OF COMPLEXES

2.5.1 PURIFICATION OF 5'/3'-TR COMPLEX

The 5'/3'-TR complex was formed by mixing equimolar concentrations of 5'-TR and 3'-TR at room temperature (~ 20.0 °C) for 30 minutes, followed by the use of SEC (HiLoad 26/60 Superdex 200 gel filtration column, GE Healthcare Life Sciences) to separate the 5'/3'-TR RNA from the leftover TR RNAs.

2.5.2 PURIFICATION OF OAS1+3'-TR AND OAS1+5'-TR RNA COMPLEX

Purification of complex of OAS1 with either of the TR RNAs (5' and 3'-TR) was a challenge. My efforts to purify OAS1+TR RNA complex by mixing them in ratio of 1.1:1 (RNA:OAS1) in 50 mM Tris, pH 7.5 and 100 mM NaCl, followed by concentrating and performing SEC failed to obtain the complex. As EMSA confirmed the interaction of the TR RNAs with OAS1, I approached the purification of complex using similar buffer condition as in a TBE-PAGE but without boric acid. TR RNA and OAS1 (in 50 mM Tris, 40 mM NaCl, 1 mM EDTA, pH 7.5) were mixed in a ratio of 1.1:1 and incubated at room temperature (~20.0 °C) at RNA concentration of 2 µM (20 mL volume) for 10 minutes, concentrated (Mw cut-off, 10000; Millipore) to a

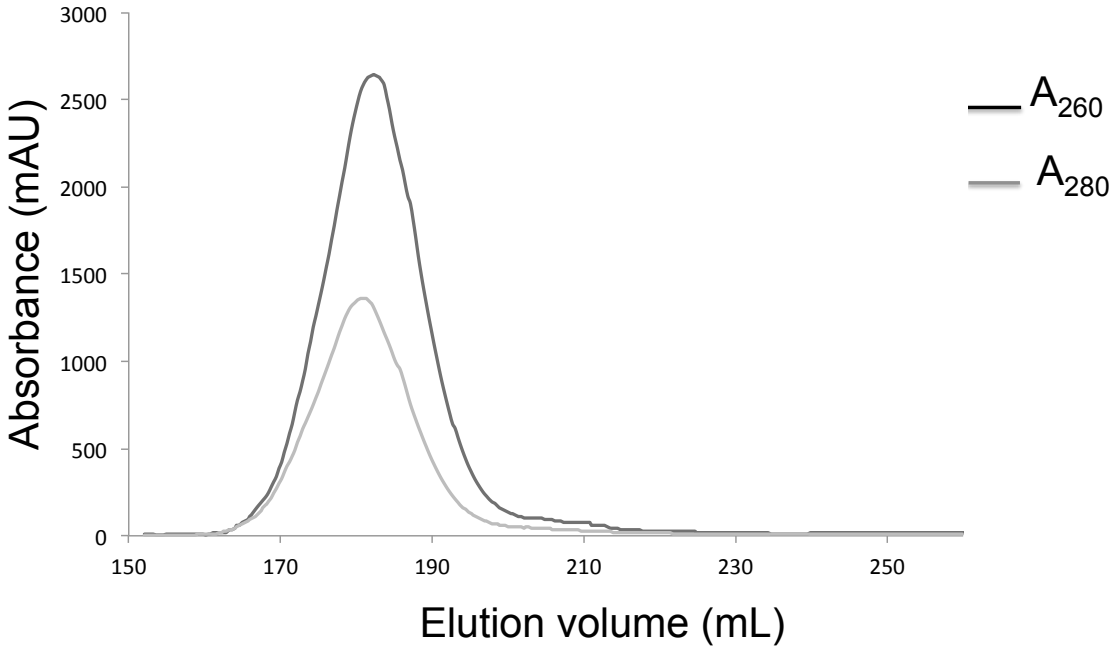

Figure 2.6 SEC profile of OAS1+5'-TR on a HiLoad 26/60 Superdex 200. 3 mL fractions were collected under this peak (peak maxima at ~ 180 mL).

volume ~ 2mL and loaded onto a HiLoad 26/60 Superdex 200 gel filtration column (2.6 Å~ 60 cm, GE Healthcare). The SEC buffer was the same as was used in OAS1+TR RNA-complex formation (50 mM Tris, 40 mM NaCl, 1 mM EDTA, pH 7.5 buffer). The SEC run was performed at 2 mL/minute and 3 mL fractions were collected under the peak area. The presence of the RNA–protein complex in each of these fractions was tested via an in-line spectrophotometer (260/280 nm simultaneously) and was confirmed by native PAGE. Fractions containing RNA–protein complex were pooled and concentrated in 50 mL Millipore concentrators (Mw cut-off, 10000; Millipore). Both the 3'-TR and 5'-TR complex with OAS1 were purified following the same procedure. The SEC profile of purification of OAS1+5'-TR complex was performed as shown in the **Figure 2.6**.

2.6 INSTRUMENTATION AND METHODS

2.6.1 ELECTROPHORETIC MOBILITY SHIFT ASSAY (EMSA)

EMSAs were performed by titrating RNA at 100 nM with increasing concentration of OAS1 in 50 mM Tris, 100 mM NaCl (pH 7.0). The RNA and protein were mixed and incubated at room temperature for 10 minutes (~ 20.0 °C), followed by addition of native load dye (0.02% bromophenol blue, 0.01% xylene cyanol FF, 10% glycerol in1X TBE). The samples were loaded onto native TBE-PAGE gels and electrophoresis was performed at 70V. The electrophoresis system (mini-protean 3 cell, Biorad) and the buffer (0.5X TBE) are kept on ice during for the length of the experiment. The

experiment takes approximately 3-4 hours for sufficient separation. To visualize RNA-containing species, gels were stained with SybrGreen II (Invitrogen Inc.) for 5 minutes and imaged by the FluorChem Q System (ProteinSimple, Inc.).

2.6.2 OAS1 ACTIVATION ASSAY

2.6.2.1 Rationale for the assay

To examine OAS catalytic activity, several approaches have been previously reported. The most common of them is the direct detection of isotope-labeled 2'-5'-A using radioactive (α-^{32}P) ATP as substrate [345]. Different analytical methods are utilized to separate 2'-5'-A chains including thin-layer chromatography (TLC), PAGE, or high performance liquid chromatography (HPLC). These methods are discussed in previous publications [346-350]. Non-radioactive methods are also possible where the pyrophosphate that is generated as a byproduct of the formation of 2'-5'-A chains is quantified either directly or indirectly. Indirect quantification of PPi produced was possible via enzymatic production of an equimolar quantity of NADPH, which has strong fluorescence [213]. Although the strong fluorescence of NADPH makes it convenient to measure using a fluorometer, the complex enzyme coupled reaction involving three different enzymes to obtain NADPH itself is cumbersome, prone to error and costly [213,351]. We have modified and developed a more direct colorimetric assay to measure PPi generated by OAS1 enzymatic activity. This method proceeds through reaction of PPi with ammonium molybdate to form PPi-molybdate complexes in the presence of sulfuric acid. PPi-molybdate

complexes in the presence of thio reagent (β-mercaptoethonal) and a developing reagent (Eikonogen) results in a blue-colored solution with absorbance maximum at 580 nm (**Figure 2.7**) [352]. This relatively simple, non-radioactive method is sensitive to 20 nmoles of PPi present in a 1 mL. While less sensitive than radioactivity this colorimetric assay is quick and cost-effective.

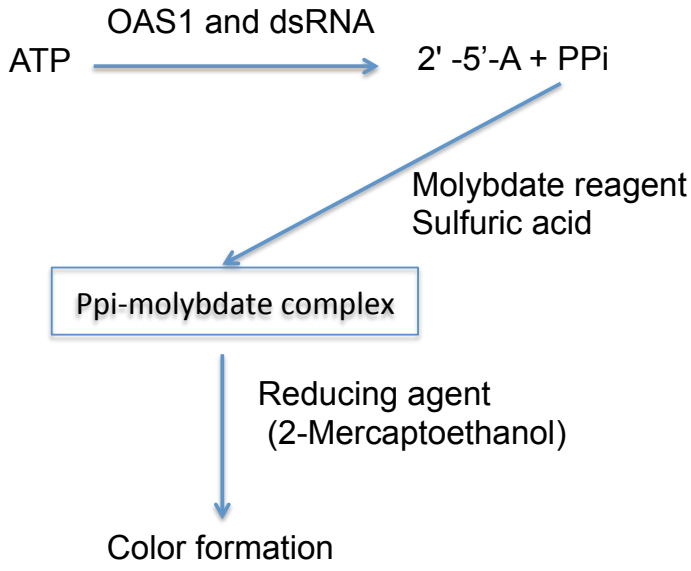

Figure 2.7 Schematic representation of colorimetric assay performed.

2.6.2.2 Experimental Procedure

We have developed a method with slight modification to a previously established colorimetric method to quantitate the amount of PP_i produced as a byproduct to the formation of 2'-5'-A by OAS1 (123, 124). The OAS1 enzymatic reactions were performed in the presence of 20 mM Tris, 5mM $MgCl_2$, 1 mM DTT and 2 mM ATP. To these reactions either *in vitro* transcribed RNA or poly I:C were added and then incubated at 37°C for the enzymatic activity to proceed. The reactions were

quenched at specific time points by the addition of 50 mM EDTA. 100 µL of molybdate reagent (2.5% ammonium molybdate in 2.5 M H_2SO_4) and 100 µL of β -mercaptoethanol (BME) (0.5M) were added to an aliquot of 50 µL of quenched reaction leading to production of molybdophosphoric acid. To this mixture 40 µL of Eikonogen reagent (0.125 g of 1-amino-2-naphthol-4-sulfonic acid, 0.125 g of sodium sulfite and 7.325 g of sodium bisulfite to 100 mL of ddH_2O) was immediately added. The final volume was quickly adjusted to 1 mL with ddH_2O and the resulting molybdenum chromophores (blue in color) were subjected to spectrophotometer analysis (NanoDrop2000c, Thermo Scientific). Absorbance measurements at 580 nm recorded for the reactions were then compared to similar measurements obtained for a PP_i standard curve. The standard curve was generated with PPi standard solutions containing known quantity of pyrophosphate and subjecting them to identical colorimetric analysis. Performing triplicates of identical reaction conditions at multiple RNA concentrations was sufficient data to be used for kinetic analysis. Data analysis was performed as outlined previously, where the reaction velocities (V) were calculated by linear regression of early time points that maintain a statistically accepted linear fit [213]. The statistical acceptance of our studies were judged based on the R^2 value > 0.95. The optimal OAS1 concentration to ensure a response to activating RNA added was determined using Poly I:C as an activator. As in this experiment the concentration of ATP is 2 mM, which is much greater than the enzyme concentration of 400 nM, the reaction can be assumed to be independent of the substrate concentration under this condition. The dsRNA, the OAS1 activator can be considered as a pseudo-substrate and the initial rate of

reactions (V_0) monitored by the formation of the bi-product PP_i shows linear relation to the RNA concentration (there is increase in V_0 with increase in [RNA]) in the lower concentration range [353]. The V_0 is calculated at initial time points, where the product concentration is assumed to be zero at the beginning of the reaction and product formation is linearly related to reaction time. Overall the reaction here can be represented by a first order reaction that follows Michaelis–Menten kinetics. A modified version of the Michaelis–Menten kinetics equation used in my thesis is [353] [354]:

$V = V_{max}[\mathrm{RNA}]/([\mathrm{RNA}]+K_{app})$ (equation 2.1)

Where V is V_0 as we are considering only initial velocity of the activation reactions and K_{app} is the apparent equilibrium constant. This equation could be derived as described as:

$$[E]+[RNA] \underset{}{\overset{K_R}{\rightleftharpoons}} [E_R]+[S] \underset{k_2}{\overset{k_1}{\rightleftharpoons}} [E_{RS}] \underset{k_4}{\overset{k_3}{\rightleftharpoons}} [E_R]+[P]$$

As the enzyme requires being in RNA bound form for it to be activated, I have introduced the RNA as an activator. Assumptions include k_3 to be the rate limiting step and the k_4 to be negligible at early time points.

$V = k_3[E_{RS}]$

E total or $[E_T] = [E] + [E_R] + [E_{RS}]$

$V/[E_T] = k_3[E_{RS}]/[E] + [E_R] + [E_{RS}]$ (equation 2.2)

From the equilibriums above we can get $[E_R] = ([E] + [RNA])/K_R$ (equation 2.3)

Also simplifying the equation with k_1, k_2 and k_3 and expressing them in k_m, I can get

$[E_{RS}] = ([S] + [E_R])/k_m$ (equation 2.4)

Replacing $[E_{RS}]$ in equation 2.2 with values from equation 2.3 and 2.4 we get

$V/[E_T] = ((k_3 [E_R] [S])/ k_m)/([E]+([E][RNA]/ K_R)+([E_R][S]/k_m))$ (equation 2.5)

$V/[E_T] = (k_3 [RNA] [S]/ K_R k_m)/([RNA]/ K_R) + ([S] [RNA]/ K_R k_m)$

$V/[E_T] = ((k_3 [RNA] [S]/ K_R k_m)/(1+[RNA]/ K_R)+ [RNA] [S]/ K_R k_m))$

Dividing both the numerator and denominator by $K_R k_m$ we get

$V= V_{max}/((k_m/[S](1+ K_R/[RNA])+1))$ (equation 2.6)

Multiplying the numerator and the denominator by [RNA] we get

$V= V_{max} [RNA]/(k_m/[S] [RNA]+ K_R k_m/[S]+ [RNA])$ (equation 2.7)

By rearranging the equation 2.6

$V= ((V_{max}/(k_m/[S]+1)/[RNA])/(([RNA]+ K_R k_m/[S]/(k_m/[S]+1))$

At higher [S], $k_m/[S]$ becomes 0. Above equation can be now written as

$V= V_{max} [RNA]/([RNA]+ K_R k_m/[S])$ (equation 2.8)

Now dividing both the numerator and the denominator of the equation 2.8 by [RNA] we have

$V= V_{max} [RNA]/(([RNA]+ K_R k_m/[S]))$

We can say that the $K_{app} = K_R k_m/[S]$

Then the equation 2.8 can be written as $V= V_{max} [RNA]/([RNA]+K_{app})$ [213]

The assumption is at higher [S], the [S] remains unchanged and so it is a constant.

2.6.3 ANALYTICAL ULTRACENTRIFUGATION (AUC)

The sedimentation velocity (SV) experiment for OAS1 was performed using an Optima XL-I analytical ultracentrifuge (Beckman Instruments, Palo Alto, USA) with

an An60-Ti rotor (eight-hole titanium rotor) at 20.0 °C. A fixed volume of reference solvent (400 µL, buffer with 50 mM Tris, 100 mM NaCl with and without 1 mm DTT depending on whether its OAS1 or RNA sample respectively) and sample solutions (380 µL) were injected into the solvent and sample channels of 12 mm carbon filled center-pieces and placed properly on the rotor. Samples were run at 45, 000 rpm and 20 °C as described previously [355]. Standard 12 mm double sector cells were used where OAS1 [0.4, 0.6 and 0.8 mg/mL in 50 mM Tris, 100 mM NaCl and 1 mm DTT (pH 7.5)] and buffer were loaded in appropriate channels. SV data were collected at 7-minute intervals at 280 nm and 45,000 rpm using an absorption optical system. Data analysis were performed using the SEDFIT program [356,357], to obtain the sedimentation coefficients at each concentration ($s_{20,b}$), which were then corrected to standard solvent conditions ($s_{20,w}$) using the algorithm SEDNTERP [358]. The $s_{20,w}$ (S) values for individual concentrations were then extrapolated to infinite dilution to obtain $s^0_{20,w}$ (S). Dr. Trushar Patel had access to the AUC instrument through our collaborator (Dr. Stephen E. Harding at the National Centre for Macromolecular Hydrodynamics, University of Nottingham, Sutton Bonington, United Kingdom), and he performed the AUC on samples provided by me.

2.6.4 RNA THERMAL DENATURATION

Buffered RNA samples (1 mL at 400 nM in 50 mM Tris pH 7.0, 100 mM NaCl) were analyzed in an Evolution 260 BIO UV-Vis spectrophotometer (Thermoscientific, Weltham, MA, USA) equipped with a single cell (1 cm path length) Peltier system for

temperature control. Spectra (200 nm to 400 nm) were collected for each sample in at least triplicate every 5 °C between 20 and 85 °C, and the absorption change at 260 nm relative to the 20 °C measurement was plotted versus temperature. The midpoint on the linear transition region of the melting curve was used to estimate melting temperature (T_m) using a method outlined previously [359].

2.6.5 DYNAMIC LIGHT SCATTERING (DLS)

Dynamic light scattering (DLS) is a technique used to determine macromolecule size distribution in solution and is used in my study to ensure monodispersity of a sample over a concentration range [360]. The macromolecular size determined from DLS is its hydrodynamic radius (r_H), which is dependent on both the size/shape of the molecule and its interaction with the solvent. DLS data were collected using a Zetasizer Nano S system (Malvern instruments Ltd, Malvern, UK) as described previously [361]. A scattering angle of 173° was employed. Wild type OAS1 (20 µL) in 50 mM Tris (pH 7.5), 100 mM NaCl and 1 mM DTT was filtered using a 0.1 µm syringe filter (Millipore, USA) and subjected to DLS measurements at 20.0 °C at 3 different concentrations. Similarly, the DLS data for the WNV 5'-TR (SLI/II/III) was collected at a single concentration in 50 mM Tris (pH 7.0), 100 mM NaCl. The molecular weight of OAS1 was calculated using a version of the Svedberg equation adjusted to include the equivalent hydrodynamic radius r_H in place of the translational diffusion coefficient:

$$Mw = \frac{6\pi\eta_0 r_H s^0_{20,w}}{1 - \bar{v}\rho_0} \qquad \text{(equation 2.9)}$$

where $\bar{\nu}$ is the partial specific volume (specific volume of the macromolecule with its hydration shell), $s^0_{20,w}$ is sedimentation coefficient in water at 20°C, η_o is the solvent viscosity, ρ_o is the solvent density and N is the Avogadro's number. 3'-TR (1.5-2.8 mg/mL), 3'-SL (2.0-4.5 mg/mL), 5'/3'-TR complex (2.2-3.0 mg/mL) and a second set of 5'-TR measurements (1.5-2.1 mg/mL), were measured in 50 mM Tris (pH 7.0), 100 mM NaCl. The DLS data was acquired for OAS1+5'-TR (4.5-6 mg/mL), OAS1+3'-TR (3.5-6 mg/mL), 5'-TR (1.5-3.5 mg/mL) and 3'-TR (1.2-2.4 mg/mL) in 50 mM Tris (pH 7.5), 40 mM NaCl and 1 mM EDTA.

2.6.6 SMALL ANGLE X-RAY SCATTERING

2.6.6.1 Principle and underlying theory

Small angle X-ray scattering (SAXS) is a scattering technique where the X-ray interacts with electrons in the molecule resulting in scattering [362,363]. The scattering data generate information on average size and shape of the sample particle. As SAXS is a solution technique, key assumptions are made to analyze the data. The first assumption is that the system under consideration is isotropic, which means the sample is uniform in all orientation. The isotropic nature could be attributed to rotation of particles in solution. The second assumption is that there is no correlation between two scattering centers (electrons) present in two different molecules [363].

Figure 2.8 is a schematic representation of the major steps involved in SAXS data collection and processing; and *ab initio* model generation all of which will be discussed in this section. X-rays are electromagnetic waves with high-energy. When an X-ray hits an electron, the electron resonates with the frequency of the X-ray and emits coherent secondary waves. If these secondary waves (scattered waves) have the same wavelength (λ) as the original X-ray, it is referred to as elastic scattering [363,364]. In SAXS the elastic scattering contributes to the scattering data almost entirely. Inelastic scattering is ignored, as it is too weak and does not interfere with the elastic scattering. If we consider a case where there are two electrons and two scattered rays from them reach the detector, at the time of the arrival if these two rays are in phase then its known as constructive interference and if they are out of phase it is deconstructive interference [364]. The electrons basically act as the source of a secondary X-ray wave [363]. The pattern on the detector encodes information on the distance between the two electrons under consideration because the intensity of the spot on the detector contains information on amplitude. The amplitude will have information on the phase difference of the two secondary waves under consideration, which in-turn depend on the path difference of the two rays. If the path distances (the distances between the spot recorded on the detector and the secondary wave sources or a pair of electrons) are very large compared to the path difference between them, then the sources are considered parallel to the detector [363,365]. The software program PRIMUS [366] is used to convert this scattering pattern into a SAXS scattering curve, both of which are in reciprocal space. This

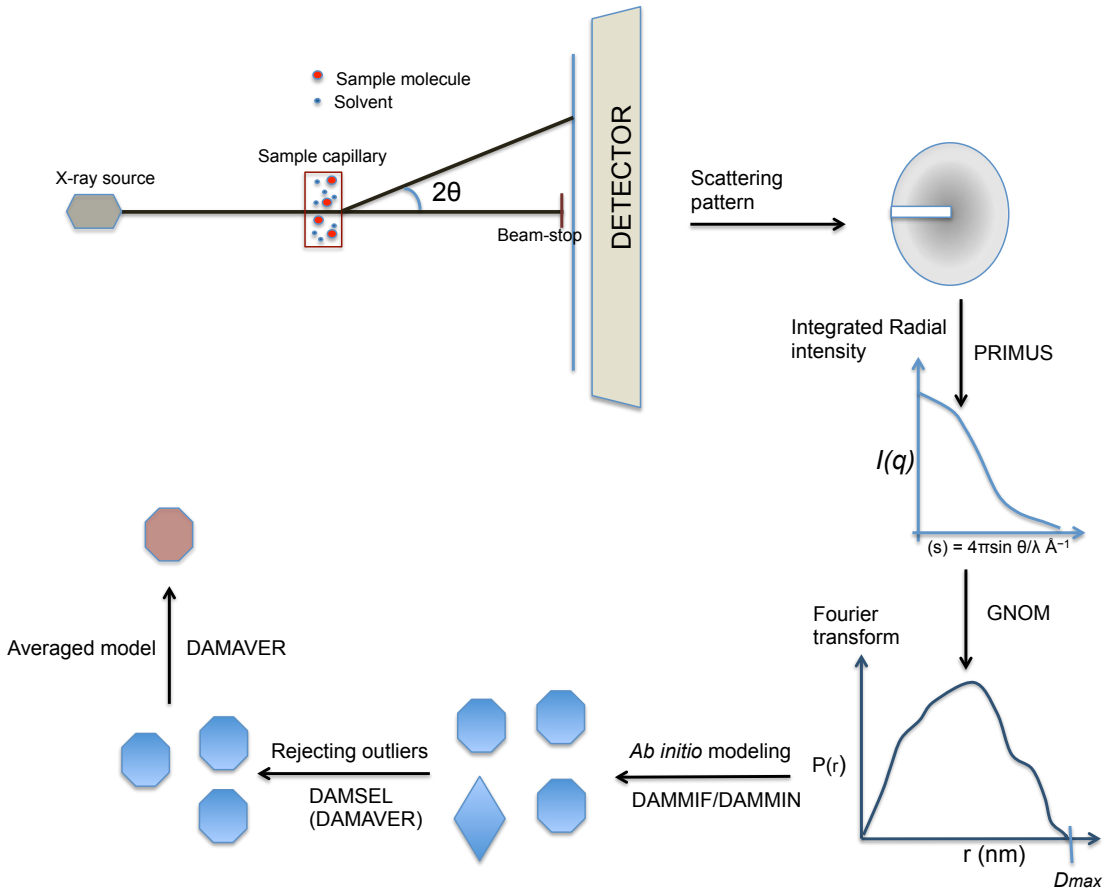

Figure 2.8 Schematic representation of Small angle X-ray scattering and its data analysis. The sample scatter collimated X-ray beams (Cu Kα radiation) that are registered on the detector as a circular scattering pattern that is in reciprocal space. Integrating the radial intensity of this circular scattering pattern generates the SAXS scattering curve where the momentum transfer (s) is plotted against log of intensity *I(q).* This scattering curve is converted to a pair distribution function curve *P(r)* that is in real space. Maximum particle dimension (*Dmax*) is marked on the X-axis and radius of gyration (r_G) is calculated in this step. From the *P(r)* plot we proceed towards building a number of *ab initio* models. In the succeeding steps outlier models are rejected and an averaged model is obtained. All the programs used in the data analysis and model-building steps are in capital letters [362,367].

curve has the log of intensity *I(q)* plotted against the momentum transfer denoted by

(s) [367]

$(s) = 4\pi \sin\theta/\lambda$ (equation 2.10)

Here θ is the scattering angle and λ is the wavelength of the X-ray radiation. At larger scattering angles (θ) destructive interference (resulting from secondary waves emitted from all electrons that include waves in all possible phases) will lead to no scattering with directionality of θ. But at smaller scattering angles the phase difference between the scattered waves will be smaller, limiting destructive interference, and enabling scattering in the direction of the small angle to be recorded on the detector. Ideally we would have no interference at zero angle but we don't obtain data at that angle, as the beam-stop is present there to protect the detector from direct exposure to X-ray [363,368].

The scattering data obtained in reciprocal space is converted to real space data in form of the pair distribution function *P(r).* As the name suggests it is a distribution of distances between all pairs of particles (source of secondary waves) in a molecule based on its electron density. In other words, it is a histogram of all distances between electrons in a pair of electrons [369]. This curve is generated by inverse Fourier transform that de-convolutes distance information on electron pairs and is performed by the software program GNOM [369,370]. Using the schematic representation of an electron pair in the figure (**Figure 2.9**), it can be said that the: $\gamma_0(r_{ij})$ is the probability of finding (j) at a distance (r) from point (i), the number of possible i is directly proportional to the volume (V) of the molecule, where the number of possible (j) is directly proportional to r_{ij}^2. The number of electron pairs (i,j) with a distance r_{ij} between them is directly proportional to $\rho^2\ \gamma_0(r_{ij})\ Vr^2$. The pair distribution is given by [367]

$$P(r)= r^2\ \gamma_0(r)V\ \rho^2= r^2\gamma(r) \qquad \text{(equation 2.11)}$$

Hydrodynamic parameters including maximum particle dimension (D_{max}), which spans the distance on the X-axis from the origin to the end-point where the curve meets the X-axis again, and radius of gyration (r_G), are also obtained using GNOM. The GNOM uses a Guinier plot to obtain the r_G where the slope of the curve is the negative value of the square of r_G over 3 [371].

Slope = $- r_G^2/3$ (equation 2.12)

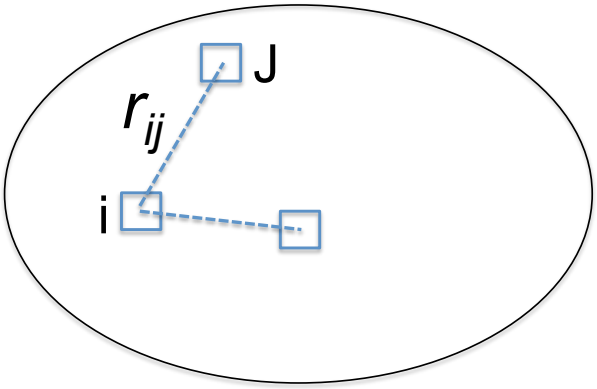

Figure 2.9 Schematic representation of an electron pair in an effort to explain pair distribution function curve. The electron j at a distance *r* from reference electron 'i' is in a molecule with volume *V*. The density of electrons in this molecule is given by ρ [367].

The r_G is a model independent parameter (no information on shape/structure) given by the root mean square distance of points in a molecule from the center of mass and is measure of how the mass of that molecule is distributed around its center [371]. The r_G value is the square root of r_G^2 given by the formula:

$$r_G^2 = \frac{\int_{Vr} \Delta\rho(r)\ r^2\, dVr}{\int_{Vr} \Delta\rho(r)\, dVr}$$

(equation 2.13)

Where V is the volume of the particle or sample, $\Delta\rho(r)$ the contrast in electron density between sample and solvent, r is the distance from the reference point (i) to a particle or electron at another point (j), r^2 is the square of distance between an electron pair [367].

The *ab initio* modeling with the scattering data obtained begins with finding a particle (usually a sphere) that has the closest X-ray scattering pattern to that of the sample and the D_{max} of the particle affects the size of the selected sphere [341]. This sphere (assume its radius as R) is then filled with N number of densely packed small spheres (dummy atoms) of radius r. The number of dummy atoms (N) is usually close to 1000. Then the connectivity, which is denoted by the number of non-solvent atoms, an atom under consideration is in contact with, for which each dummy atom is defined. This approach to *ab initio* modeling was discussed previously and the software programs are called bead-modeling programs [368,372]. These programs employ energy minimization through a simulated annealing protocol [373]. The use of the simulated annealing protocol in this context can be explained as heating the system, allowing a random modification and slowly cooling-down the system and verifying whether this modification results in decreasing the energy of the system. *Ab initio* modeling software, including DAMMIF and DAMMIN use the r_G and D_{max}, which provide the constraints for the models generated [368,372]. The predicted scattering of the model molecule after every energy minimization step is calculated and compared with the experimental scattering profile of the sample to check for conformity, which is given by parameter Chi (χ). The level of agreement of the filtered model generated by DAMAVER to the

individual *ab intio* models is given by normalized spatial discrepancy (NSD). So, NSD is the quantitative measurement of alignment between two models where each model is represented by a collection of dummy atoms, and a smaller NSD value demonstrates better agreement between these models [374]. The simulated annealing protocol employs high temperature in the beginning of the energy minimization steps and the changes are almost random, which may generate both high and low energy configurations, but towards the end of the protocol the temperature is much lower, and a configuration with nearly minimum energy is reached [368,372]. The major drawbacks of SAXS are the loss of actual phase of the X-ray because the sample being in solution and the usability confined to only one/two phase systems. It is also important to include the assumptions made for SAXS analysis including the monodispersity of sample and its infinite dilution (no effect on the sample behavior because of change in sample concentration) [365,371].

2.6.6.2 Sample concentrations and experimental specifications

SAXS data for proteins (wild type and mutant versions of OAS1), RNAs including WNV 5'-TR, 3'-TR and 3'-SL RNA were collected using an in-house Rigaku instrument as described previously [272] . This in-house Rigaku S-MAX3000 is equipped with a Rigaku MicroMax+002 microfocus sealed tube (Cu Kα radiation at 1.54 Å) and a Confocal Max-Flux (CMF) optics system operating at 40 W (Rigaku). It has a 200-mm multiwire two-dimensional detector to record generated scattering

data. The data for all RNA and protein samples and buffer were collected for 3 hours for each sample within the range of $0.008 \leq s \leq 0.26$ Å^{-1} and processed according to the method previously described, where momentum transfer (s) = $4\pi\sin\theta/\lambda$. Here the θ is the scattering angle and λ is the wavelength of the X-ray radiation. SAXS data for wild type OAS1, R195E and K199E mutants were collected at multiple concentrations (wild type: 3.1, 3.8, 4.5 and 5.2 mg/mL; R195E: 2.2, 2.6, 3.0 and 3.4 mg/mL; K199E: 2.3, 2.7, 3.1 and 3.5 mg/mL) in 50 mM Tris, 100 mM NaCl and 1 mM DTT at pH 7.5. SAXS data for the 5'-TR (in 50 mM Tris, 100 mM NaCl and 20 mM $MgCl_2$ at pH 7.0) were also collected at multiple concentrations (0.8 mg/mL, 1.6 mg/mL and 2.0 mg/mL). SAXS data were collected at multiple concentrations for 3'-TR RNA (1.5, 2.0 and 2.9 mg/mL), 5'-TR RNA (2.5 and 3.5 mg/mL), OAS1+3'-TR RNA complex (3.0, 4.0 and 5.0 mg/mL) and OAS1+5'-TR RNA complex (3.0, 4.0 and 5.0 mg/mL) in 50 mM Tris, 40 mM NaCl and 1 mM EDTA at pH 7.5. Scattering data were also collected in 50 mM Tris, 100 mM NaCl, pH 7.0 buffer at multiple concentrations for 3'-SL (1.6, 2.0 and 2.2 mg/mL), 5'/3'-TR RNAs (2.0, 2.5, 3.0, 3.5, 4.0 and 4.5 mg/mL) and 3'-TR RNA (1.5, 2.0, 2.5 and 3.0 mg/mL). Primary data analysis was performed using program PRIMUS [366], followed by estimation of the root mean square radius of gyration (r_G) and the maximum particle dimension (D_{max}) using the program GNOM [370].

Ab initio shape reconstruction of OAS1 WT was performed using the program DAMMIF, that utilizes simulated annealing [372]. In addition to the *ab initio* shape determination, the high-resolution structure of the porcine OAS1 homolog (PDB code: 1PX5 [217]) was used to reconstruct the solution conformation of OAS1 using the program BUNCH [375] as described elsewhere [376]. Twelve models using DAMMIF and ten models using BUNCH were generated which were then rotated, aligned and averaged using DAMAVER [377]. The program HYDROPRO [378] was employed to calculate solution properties such as hydrodynamic radius, radius of gyration and maximal particle dimension for each model calculated using SAXS data following a similar approach as outlined previously [379]. The input parameters included the density (1.0038 g/mL) and viscosity (0.01026 Poise) for buffer (50mM Tris, 100mM NaCl) as well as partial specific volume of OAS1 (0.7424 mL/g), obtained from the program SEDNTERP [380]. The molecular weight of OAS1 was calculated from its amino-acid sequence using the protparam utility on Expasy server [381].

The *ab initio* models for RNA and OAS1+RNA complexes were generated using DAMMIF. For the 5'-TR twelve *ab initio* models were generated using DAMMIF, which then are rotated and aligned using DAMAVER [377]. The same software for modeling and model alignment was used for 5′/3′-TR complex, where

fifteen *ab initio* models were generated. With the exception to the 5'-TR (twelve models) and the 5′/3′-TR complex (fifteen models), twenty models were generated for all other samples (RNA and OAS1+RNA complex), which were then rotated, aligned and averaged using DAMAVER [377]. The program HYDROPRO [378] was then employed to calculate solution hydrodynamic properties averaged-filtered model following a similar approach as outlined previously [272]. The input parameters included the density and viscosity of buffer (1.0038 g/mL and 0.01026 Poise pH 7.0 for buffer containing 50mM Tris, 100mM NaCl; 1.002 g/mL and 0.01023 Poise for buffer containing 50mM Tris, 40mM NaCl, 1mM EDTA, pH 7.5) as well as partial specific volume of OAS1 (0.7424 mL/g) [211], 3′-SL (0.5698 mL/g), 3′-TR RNA (0.567 mL/g), 5′-TR RNA (0.569 mL/g), OAS1+3′-TR RNA complex (0.660 mL/g) and OAS1+5′-TR RNA complex (0.649 mL/g) obtained from the program SEDNTERP [380]. The molecular weight of OAS1 was calculated from its amino-acid sequence using the protparam utility on Expasy server [381]. Sample quality was verified for each sample pre and post SAXS data collection by both gel electrophoresis and DLS measurements. Superposition of the high-resolution structure of human OAS1 (PDB code: 4IG8 [222]) SAXS envelopes was performed manually.

2.6.7 COMPUTATIONAL RNA STRUCTURE DETERMINATION

Tertiary structures of 3'-SL and 3'-TR were computationally determined through SimRNA software using SAXS data as restraints. SimRNA is a method for RNA folding simulations by the Monte Carlo approach that uses a coarse-grained

representation and a statistical potential (developed in the Bujnicki laboratory, manuscript submitted; http://genesilico.pl/software/stand-alone/simrna). Predicted secondary structures were used to restrain canonical base pairing. First, a series of Replica Exchange Monte Carlo simulations were carried out, starting from extended RNA sequences, and 20019 low-energy folded structures (decoys) were collected. Decoys with geometrical similarity were clustered together and the central member of the largest cluster was selected as a representative model. For these models, full-atom representations were generated using a routine from the SimRNA toolkit, and their local geometry (bond lengths, angles, and steric interactions) was refined using phenix.refine [382].

The models were initially positioned into the corresponding SAXS *ab initio* reconstructions using PyRy3D (under development in the Bujnicki laboratory; http://genesilico.pl/pyry3d/). First, *ab initio* reconstructions of the 3'-SL and 3'-TR were converted into pseudo EM-maps with the sfall and fft software programs from the CCP4 suite [383]. The model of 3'-SL was fitted to the reconstruction without any modifications. The 3'-TR model was divided into two rigid regions restrained at the junction of stem at the 5' end of the structure (nucleotides from -113 to -106) and rest of the RNA. The rigid components were allowed to move, aiming to maximize the volume inside the SAXS reconstructions, minimize the volume outside of the reconstruction, minimize the violation of restraints used from SAXS data (provided by us) and partial secondary structure data [296,301,302], and minimize steric conflicts between individual components. During the fitting simulation the following values were specifically minimized: (i) the number of steric clashes

between atoms of individual model components; (ii) the volume inside the pseudo-electron density map that was unfilled by the model and volume occupied by the model outside the electron density map contour. For modeling of the 3'-TR complex with OAS1, the experimentally determined structure of the protein component (PDB code: 4IG8) and refined model of the 3'-TR RNA were treated as rigid bodies. During the fitting procedure additional restraints were used to keep OAS1 residues implicated in protein-RNA interactions close to the RNA chain (**Figure 4.8**). Our collaborators (Bujnicki Lab, Laboratory of Bioinformatics and Protein Engineering, International Institute of Molecular and Cell Biology, ul. Ks. Trojden, Warsaw, Poland) performed the computational RNA structure determination.

2.7 MAMMALIAN CELL CULTURE AND RELATED METHODS

2.7.1 CELL CULTURE AND PASSAGING

The human embryonic kidney (HEK) 293T cell line was a gift from Dr. Thomas Klonisch (University of Manitoba) and the HeLa cell line was a gift from Dr. Spencer Gibson (University of Manitoba). Cells were grown in T-75 flasks (Fisher Scientific), maintained in Dulbecco's Modified Eagle's Medium (Invitrogen, Burlington, ON, Canada) supplemented with 10% fetal calf serum (Invitrogen), 100 U/mL penicillin and 100µg/mL streptomycin (Invitrogen). A humidified incubator at 37°C with 5% CO_2 was used for cell maintenance and passaged every 3 days. Cells were grown to confluence and either passaged or used for experiment. Passaging of cell line was performed by removing cell culture media by aspiration and rinsing the cells with

10 mL sterile pre-warmed phosphate buffered saline (PBS). For HeLa cells, post removal of the PBS, 3 mL of pre-warmed 0.025% trypsin with 0.01% ethylene diamine tetraacetic acid (trypsin-EDTA) (Invitrogen) was added to facilitate cell detachment. Cells were incubated at room temperature in the trypsin-EDTA solution for 1-2 minutes for complete detachment to occur. HEK 293T cells were detached mechanically using a disposable scraper. Following detachment, 12 mL of pre-warmed cell culture media was added to the flask, mixed slowly by pipetting and the total volume was carefully transferred to a 15 mL conical centrifuge tube (Thermo Scientific). The cells were pelleted by centrifugation of the cell suspension at 1000g for 5 minutes in an SORVALL ST40R (Thermo scientific) fitted with a swing-bucket rotor following which the supernatant was aspirated. The cell pellet was resuspended in cell culture media and then split at a ratio of 1:5 for both HEK 293T and HeLa cells. A haemocytometer was always used to calculate and start with an approximately equal number of cells appropriate for the dish size. Ideally we attempted to attain ~70% confluence for the day of experimentation (typically transfection). For both the cell lines used, the doubling time was ~20 hours and that is taken into account while estimating plating time.

2.7.2 BIOTINYLATION OF RNA

RNAs was biotinylated at their 3' end by attachment of a biotin linker (Integrated DNA technologies, Coralville, Iowa, US). The biotinylation reaction was performed in 1X T4 RNA ligase buffer (50mM Tris pH 7.5, 10mM $MgCl_2$,

10mM DTT, 1mM ATP), 0.1 mg/mL of Bovine serum albumin (BSA), 1 unit of T4 RNA ligase enzyme per 3 picomoles of RNA, 10% Polyethylene glycol (PEG), and 15 µM biotin linker. The T4 RNA ligase (catalogue number EL0021), 10x T4 RNA ligase buffer, BSA (1mg/mL) were purchased from Thermoscientific, Pittsburg, PA, US. The PEG (catalogue # V3011) was procured from Promega, Madison, WI, US. After biotinylation, the RNA was isolated using Genejet RNA

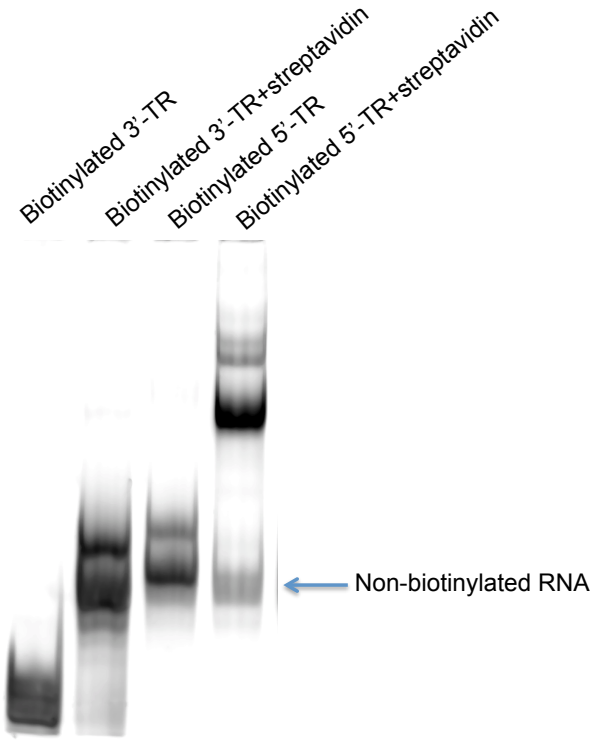

Figure 2.10 EMSA performed on a TBE gel to check biotinylation efficiency. A shifted band represents a higher molecular weight species (biotinylated RNA+streptavidin complex). The non-biotinylated RNA fraction is labeled and intensity of this RNA band is compared with the intensity of biotinylated RNA band to measure the efficiency of biotinylation. The amount of RNA to be added in a reaction is calculated based on the efficiency of biotinylation. To visualize RNA, the gel was stained with Sybr® Gold.

clean-up kit (K0731, Thermo scientific). EMSA on biotinylated RNA (100 nM) with streptavidin (1 μM) were performed on a TBE determined the success of biotinylation efficiency. The biotinylation efficiency was calculated by comparing the amount of non-biotinylated RNA remaining (**Figure 2.10**) in the lane with streptavidin against the biotinylated RNA alone lane.

2.7.3 TRANSFECTION OF PLASMID DNA AND RNA

For over-expression of OAS1 in HEK 293T cells, pcDNA3 (Invitrogen, Burlington, ON, Canada) plasmid DNA containing the OAS1 p42 cDNA was transfected using TurboFect Transfection reagent (Fisher scientific) according to the manufacturers protocol. Transfection of biotinylated 5'-terminal region RNA into the same HEK 293T cells was performed using the Lipofectamine® RNAiMAX transfection reagent (Life technologies, Invitrogen, Burlington, ON, Canada) and the manufacturer's protocol were followed.

2.7.4 CELL LYSIS

Whole-cell lysates for subsequent experiments were prepared with two ice-cold lysis buffers used in succession: Cytoplasmic lysis buffer (25 mM HEPES at pH 7.9, 5 mM KCl, 0.5 mM $MgCl_2$, 0.5% NP-40 IGEPAL a nonionic surfactant) and nuclear buffer (25 mM HEPES at pH 7.9, 10% w/v sucrose, 350 mM NaCl, 0.01% NP50 a nonionic surfactant) were used, with both buffers supplemented with Halt® protease inhibitor cocktail for single use (Thermo scientific). The media from

confluent 150mm (6-well) dishes were replaced with cold PBS buffer. Cells from a dish were detached with a cell scraper and transferred to a 2 mL snap cap tube and were pelleted by centrifugation at 3000 rpm for 5 minutes. Then the supernatant removed by slow pipetting. To the pellet, 350 µL of cytoplasmic lysis buffer supplemented with protease inhibitor. The tube was subjected to vortexing for 10-15 seconds to ensure that the cell pellet was resuspended. A second centrifugation at 5000 rpm for 5 minutes was performed and the supernatant was removed and the pellet stored in a 2 mL tube on ice. The pellet was resuspended in nuclear lysis buffer, vortexed 3 x 10 seconds, and supernatant from the previous step was added to it. Cell debris from this combined fraction (containing cytoplasmic and nuclear lysis buffer lysate) was eliminated by centrifugation at maximum speed for 10 minutes, with the retained supernatant transferred to a fresh 2 mL snap cap tube. All centrifugations were performed using a standard tabletop micro-centrifuge at 4°C (Thermo scientific).

2.7.5 STREPTAVIDIN PULL-DOWN ASSAY OF BIOTINYLATED RNA

An equal volume of 2X binding buffer (50 mM Tris acetate pH 7.8, 100 mM KCl, 10 mM NaCl, 3mM MgCl2, 70 mM glycine, 10% glycerol) was added to the lysate. The lysate was split into a number of tubes depending on the RNA probes and control pull-downs to be performed. RiboLock RNase inhibitor (Thermo scientific) was added to the split fractions to which biotinylated RNA will be added. The biotinylated probes were added to a final concentration of ~400 nM based on the

estimated biotinylation efficiency. Binding reactions were incubated for 30 min at room temperature on a LabQuake rotating shaker (Thermo scientific). 50 µL of streptavidin magnetic beads were added for each binding reactions. Prior to adding the beads, the beads were equilibrated involving 3 cycles of resuspension (resuspension buffer is 1:1 mix of cytoplasmic and nuclear lysis buffers) and placing the tube on a magnetic rack, which separates the beads leaving a clear solution to be pipetted out. Following additional 60 minutes incubation at room temperature using the rotating shaker, the tubes were placed on the magnetic rack and the beads were separated from the solution. The beads were subjected to 9 washes (3 times with 1:1 mix of cytoplasmic and nuclear lysis buffers, 3 times with cytoplasmic lysis buffer and finally 3 times with nuclear lysis buffer). After washing, beads were resuspended in 60 µL 1X SDS loading dye (see section 2.7.6 for components of the loading dye), boiled for 5 minutes, spun on a tabletop centrifuge at high speed for a minute and the isolated proteins (supernatant) were separated by SDS/PAGE.

2.7.6 SDS/PAGE AND WESTERN BLOTTING

Equal amounts of protein were resolved by SDS/PAGE. The protein concentration was calculated using a Bradford assay. Total protein concentration was determined by performing the Bradford assay using known amounts of BSA as a Bradford standard curve [384]. Specifically, 200 µL Bradford reagent (Biorad, Mississauga, ON, Canada) and 10 µL of protein lysate were pre-diluted 10 and 20-fold respectively in ddH_2O. The standard curve was prepared with 0.1-1 µg/µL BSA with

25 µL of protein sample added to 975 µL of diluted Bradford reagent. Absorbance was measured in triplicate for each standard and sample at 595 nm. 5x SDS loading dye (0.313 M Tris pH 6.8, 50% glycerol, 10% SDS 0.05% bromophenol blue) was added to the protein samples to obtain the loading dye concentration of 1X, and loaded onto the stacking gel. Protein was separated on a 10% polyacrylamide resolving and the gel electrophoresis was performed in 1x Tris-Glycine SDS running buffer (3.03g Tris, 14.4g Glycine, 1g SDS brought to 1 L) in a mini-protean 3 cell (Biorad). Gels were run at 100V (constant voltage) for protein migration through the stacking gel and at 175V while migrating through the separating gel (10% acrylamide). After protein separation by the SDS/PAGE, the proteins were transferred to polyvinyl difluoride (PVDF) membranes (Hybond P, GE Healthcare, Piscataway, NJ, US). A wet transfer apparatus (Biorad) was used and the transfer was done at a constant voltage of 100V for 1 hour at ~4°C keeping the current below 350 mAmp. Membranes were blocked with 5% skim milk powder dissolved in Tris buffered saline containing 0.1% Tween-20 (TBS-T) for 1 hour at room temperature on a shaker. The amount of primary antibody required was calculated based on the manufacturers guideline, dissolved in 5% milk TBS-T. Primary antibody was incubated with the membrane at room temperature for an hour. The primary antibodies used were anti-6XHis Tag antibody (mouse, ab18184, Abcam, Toronto, ON, Canada with 1:4000 dilution), anti-OAS1 monoclonal antibody (rabbit, 89017912, Abnova, Walnut, CA, US with 1:2000 dilution) and house keeping gene mouse-α–tubulin (T6074, Sigma-Aldrich, Oakville, ON, Canada with 1:10000 dilution). Following incubation with primary antibody the membrane was washed

in TSB-T (3 X 5 minutes washes) and then incubated for an hour with appropriate horseradish peroxidase (HRP) conjugated secondary antibody (anti-mouse secondary antibody when 6X His or mouse-α–tubulin primary antibody was used and anti-rabbit secondary antibody when anti-OAS1 antibody was used both antibodies diluted 1:10000 in 5% milk TBS-T). The membrane was washed (3 X 10 minutes) and then 2 mL of Luminata™ Forte Western HRP substrate (Milipore) was applied directly on it. The chemiluminiscence generated by the HRP (conjugated to the secondary antibody) was visualized using FluorChem Q System (ProteinSimple, Inc.).

2.7.7 OAS1 IMMUNOPRECIPITATION AND RNA IDENTIFICATION

The interaction of OAS1 with the 5'TR was determined by an immunoprecipitation approach. Specifically, cells overexpressing OAS1-6XHA tag were lysed. Cell lysate was obtained as described in **2.7.4.** RiboLock RNase inhibitor (Thermo scientific) was added and the lysate (total volume of 450 µL) was split into three fractions (aliquots of binding reaction) in snap cap tubes. 5'-TR RNA was added to a final RNA concentration in the reaction to a final concentration of 500 nM in two of these three fractions. All three binding reactions were incubated for 30 minutes at room temperature on a LabQuake rotating shaker following which 10 µL of specific antibodies (anti-6X His antibody from Thermo scientific, isotype control or mouse IgG1 negative control from Millipore, Toronto, Canada, and anti-α–tubulin antibody Sigma-Aldrich, Oakville, ON, Canada) were added to two of these tubes. The isotype

control fraction and the fraction with the anti-α–tubulin antibody are the negative controls in the RT-PCR experiments. After this step, 50 µL of protein AG magnetic beads (Pierce, Thermo scientific, US), which was prepared in the same way as described previously (section 2.7.5), were added to each reaction mixture. Protein AG beads are coated with a recombinant fusion protein containing IgG binding domains of both protein A and protein G (surface proteins found on cell walls of *Staphylococcus aureus* and some *Streptococcus* respectively)[385]. The reaction mixtures with the protein AG beads were incubated for 30 min at room temperature on a rotating shaker. Tubes were placed on the magnetic rack and the beads were separated from the solution. The beads were subjected to 12 washes (4 times with 1:1 mix of cytoplasmic and nuclear lysis buffers, 4 times with cytoplasmic lysis buffer and finally 4 times with nuclear lysis buffer). The beads were resuspended in 50 µL of RNAse free water (Thermo scientific). Total RNA was isolated using the Genejet RNA cleanup kit (K0731, Thermo scientific) according to the manufacturer's protocol, and RNA concentrations were quantified by absorbance at 260 nm with a NanoDrop2000c spectrophotometer (Thermo scientific, US). Same amount of (2 µL or ~20 ng) of total RNA was used as template for the real-time polymerase chain reaction (RT-PCR), to generate data that could be compared with each other. One-step RT-PCR was performed by directly using purified RNA with the iScript One-step RT-PCR kit (Biorad), and cycling and data collection was performed on an iCycler thermal cycler (Biorad) using the supplied software (iCycler IQ version 3.1, Biorad). Two sets of primers used for all RT-PCR experiments are indicated below:

<u>Set 1: Product length is 88</u>

Forward: CCTGTGTGAGCTGACAAACTTA (Sense), T_m 63°C complementary to sequence from 10 to 31 (in 5' to 3' direction).

Reverse: CGAGATCTTCGTGCTAAGAAACA (Antisense), T_m 63°C complementary to sequence from 52 to 74 (in 3' to 5' direction).

Set 2: Product length is 118

Forward: GGTAGTTCGCCTGTGTGAG (Sense), T_m 62°C complementary to sequence from 1 to 19 (in 5' to 3' direction).

Reverse: CCTCCTGGTTTCTTAGACATCG (Antisense), T_m 62°C complementary to sequence from 32 to 53 (in 3' to 5' direction).

Primers were added to a final concentration of 200nM for all reactions. Two sets of primers are used to select the set of primers that produces superior (higher and specific) amplification. Prior to thermal cycling, a cDNA synthesis step was performed for 10 minutes at 50°C. Following cDNA synthesis the following cycling conditions were used: 95°C for 5 min, then 40 cycles of 95°C for 10 seconds followed by the specific T_m indicated for the specific primer set. Primer specificity was confirmed by visualizing DNA on an agarose gel following PCR. Data analysis was done according to the comparative C_t method [386].

2.7.8 CROSS-LINKING

Attempts were made at cross-linking biotinylated 5'-TR with OAS1 present in the cell lysate using formaldehyde as the fixative. Biotinylated RNA probes and obtaining cell lysis were performed as described in previous sections (section 2.6.1 and 2.5 respectively). Biotinylated 5'-TR at ~400 nM was added to cell lysate followed by

addition of PBS containing 1% formaldehyde and incubated for 5 minutes with shaking at room temperature. The cross-linking reaction was stopped by the addition of 1.25 M glycine to a final concentration of 125 mM with constant shaking for 5 minutes at room temperature. As described previously, 50 µL of streptavidin magnetic beads were added for each cross-linking reactions. Following additional 60 minutes incubation at room temperature using the rotating shaker, the tubes were placed on the magnetic rack and the beads were separated from the solution. The beads were subjected to 9 washes (3 times with 1:1 mix of cytoplasmic and nuclear lysis buffers, 3 times with cytoplasmic lysis buffer and finally 3 times with nuclear lysis buffer). Beads were resuspended in 60 µL 1X SDS Loading dye, boiled for 5 min, spun in a tabletop centrifuge at high speed for a minute and the isolated proteins (supernatant) were separated by SDS/PAGE. A Western blot was performed to visualize binding of OAS1 to the biotinylated 5'-TR RNA in comparison with OAS1 cross-linked to ssCCHF (negative control single strand RNA mentioned in section 2.4.1.2). The Western blot was probed using primary antibodies for OAS1 and subsequently with the house-keeping protein α-tubulin as described previously in section 2.7.6. Similar cross-linking experiments were performed with cell lysate from HEK 293T cells that were transiently transfected with an OAS1-pcDNA3 vector (Invitrogen). pcDNA3 plasmid is an excellent mammalian expression vector with cytomegalovirus (CMV) enhancer and promoter enabling high-level constitutive expression of protein of interest. For the OAS1 *tv2* sequence to be inserted into the pcDNA3 plasmid, a set of primers was ordered to incorporate appropriate restriction sites and His tag. The primers are given below:

Forward: (**GGATCC**TACTACCTAGAGTCTTTATGGGGTCGGTTT with BamHI site in bold)

Reverse: (**GAATTC**TCA*GTGGTGATGGTGATGATG*AGCTTCATGGAGAGGGGCAGGGATG AA with ECoRI site in bold and reverse complement for sequence coding for 6X His is in italics).

Steps involved PCR amplification, insert and vector preparation, ligation, transformation, plasmid amplification and conformation of the presence of insert via sequencing was done as described previously in section 2.3.3.

CHAPTER 3: PART I OF RESULTS- ACTIVATION OF OAS1 BY STEM LOOPS AT THE 5′-TERMINAL REGION OF THE WEST NILE VIRUS GENOME

The results presented here include some unpublished data, but the majority of the results were published in a peer-reviewed journal: Deo S, Patel TR, Dzananovic E, Booy EP, Zeid K, McEleney K, Harding SE and McKenna SA (2014) Activation of 2' 5'-oligoadenylate synthetase by stem loops at the 5'-end of the West Nile virus genome. PLoS One 9: e92545.

3.1 INTRODUCTION

OAS proteins from a range of mammals and birds are shown to have effect on their antiviral response to WNV [328,329]. In humans, two different single nucleotide polymorphisms (SNPs) in the *OAS1* gene have been reported to be host genetic risk factor in the initial phase of infection with WNV [331,332]. The antiviral effects of OAS proteins have also been demonstrated against picornavirus, enterovirus and coxsackievirus, which have positive single stranded RNA genome similar to WNV [241,333]. Furthermore, human OAS1 isotypes p42 and p46 have been shown in human cell lines to block viral replication of Dengue virus and that to in an RNase L dependent manner [244]. With the information on the strong relation between OAS1 and WNV susceptibility, we focused on identifying probable viral ligands of OAS1 from WNV.

The structure of 18 bps dsRNA bound to OAS1 was solved [222], yet our knowledge of the interaction of viral or any natural RNA ligand with OAS1 is very restricted. Other previously performed studies showed the interaction of OAS1 with Poly I:C a known activator of OAS1 as well as IFN response and RNA aptamers [213]. This study also highlighted that base pairing is not the only criteria to be a dsRNA ligand of OAS1; and there is no direct correlation between the binding affinity and activation potential of RNA ligands that were in interaction with OAS1 [213]. The untranslated regions of WNV genome were most logical choices to find dsRNA ligands of OAS1. The terminal regions of UTRs of WNV are rich in double stranded regions and most protein-coding region lacks similar structural features. Secondary structure predictions supported by RNase probing of the dengue virus 5'-TR, suggest a stable secondary structure thought to be present in other *flaviviruses* suggesting a common structural arrangement of the 5' terminal region (5'-TR) amongst flaviviral family members [298,299]. Similarly the secondary structure of the WNV 3'-TR have been predicted computationally and supported by RNase probing and NMR data [296,301,302]. Together, the presence of stable secondary structures that may be highly conserved amongst *Flaviviridae* members, are an attractive targets as potential OAS1 ligands. These 5'-TR and 3'-TR RNA of WNV were previously been shown to interact with viral and cellular proteins making them stronger candidates to be being RNA ligands of OAS1 [296,312,313,315]. Biophysical and structural aspects related to genome cyclization, requiring complementary base pairing between the complementary regions in 5'-TR and 3'-TR RNA of WNV, have also been investigated [303-305].

In our effort to study the interaction of 5'-TR and 3'-TR of WNV with OAS1, we prepared all the necessary materials required as described in materials and methods (Chapter 2). The materials and methods chapter also described various experimental procedures and instrumentation used to investigate the terminal regions and OAS1 interaction. This chapter will outline the interaction of OAS1 with the 5'-TR, specifically through binding/activation and enzyme kinetics studies, and include solution conformation of the OAS1 and 5'-TR. The effect of SNPs (discussed in the introduction: section 1.2.6) on OAS1 activation potential in the presence of activating dsRNAs were also investigated. The results presented here are published in Deo, S. *et al.* (2014) PLoS One 9: e92545 [211].

3.2 RESULTS AND DISCUSSION

3.2.1 RESULTS

3.2.1.1 Solution conformation of recombinant human OAS1

In order to study the regulation of OAS1 activity by the SLI/II/III of the WNV genome, we first characterized the solution properties of the human recombinant protein to ensure homogeneity. Sedimentation velocity experiments using an analytical ultracentrifuge on purified OAS1 WT produced a single peak with a sedimentation coefficient value of 3.26±0.05 S (Svedberg units, S = 10^{-13} sec) and as the 'S' is dependent on both size and shape of the molecules affecting its sedimentation rate, this suggests that the protein is homogenous in mass and conformation (**Figure 3.1A**). The homogeneity of OAS1 was further studied using

DLS at multiple concentrations that provided the hydrodynamic radius (r_H) of 3.0±0.3 nm for OAS1 (**Figure 3.2B**). By taking the advantage of AUC and DLS data, an average molecular weight of 43.0 kDa was calculated for OAS1 that agrees well with the calculated molecular weight of 41.2 kDa. The results support the observation that OAS1 (p42 isotype) synthesized by cell free translation has been previous reported as monomeric [195]. A summary of all hydrodynamic properties for OAS1 is presented in **Table 3.1**.

Table 3.1 Experimental and predicted hydrodynamic parameters of OAS1 and 5'-TR of WNV (error shown in parentheses). The 5'-TR is represented as SLI/II/III. Published: Deo, S. *et al.* (2014) PLoS One 9: e92545 [211].

	OAS1				SLI/II/III	
		HYDROPRORO				HYDROPRO
Parameter	Experimental	DAMMIF	BUNCH	4IG8[f]	Experimental	DAMMIF
r_H (nm)[a]	3.0 (0.3)	3.13 (0.02)	3.05 (0.04)	2.90	5.1 (0.2)	5.00 (0.02)
$S^{\circ}_{20,w}$ (S)[b]	3.26 (0.05)	3.13 (0.01)	3.23 (0.02)	3.16	ND	ND
r_G (nm)[c]	2.28 (0.02)[d]	2.40 (0.01)	2.23 (0.01)	2.22	5.1 (0.1)	5.10 (0.01)
D_{max} (nm)[c]	7.1[e]	6.90 (0.04)	6.80 (0.04)	6.6	16.0	16.8 (0.01)
χ	-	0.9	1.0	-	-	1.0
NSD	-	0.52 (0.02)	0.36 (0.03)	-	-	1.10 (0.06)

[a]experimentally determined from DLS data.
[b]from AUC-SV data.
[c]from SAXS data.
[d]the r_G values for R195E and K199E are 2.43 (0.11) nm and 2.40 (0.13) nm respectively.
[e]the D_{max} values for R195E and K199E are 6.9 nm and 7.0 nm respectively.
[f]based on homology with high-resolution structure of human OAS1.
doi:10.1371/journal.pone.0092545.t001

Next, the solution conformation of recombinant human OAS1 was determined. SAXS data were collected at multiple concentrations and merged to obtain a single output file (inset **Figure 3.1C**). A maximum particle dimension (D_{max})

of 7.1 nm and a radius of gyration (r_G) of 2.28±0.02 nm were obtained for OAS1 from the pair distribution function analysis (**Figure 3.1C**). The *ab initio* shape

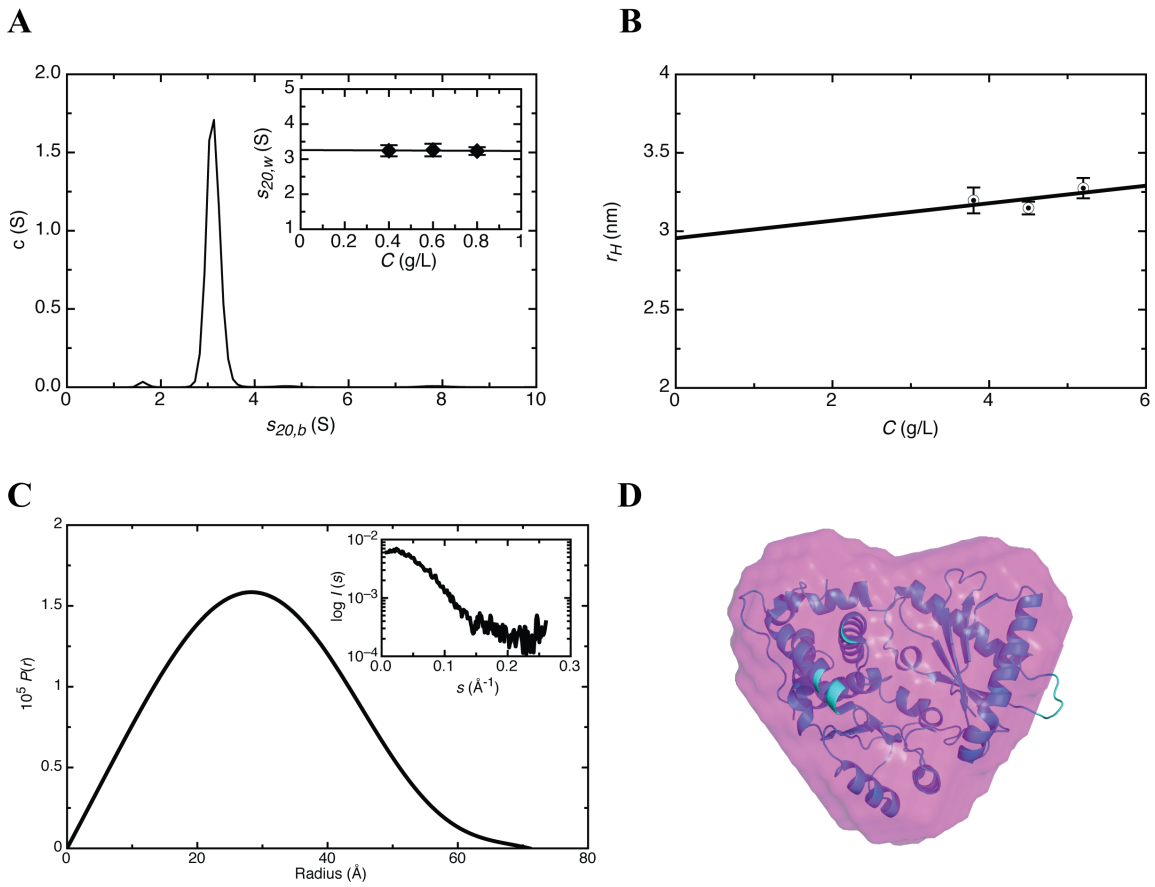

Figure 3.1 Recombinant human OAS1 adopts a globular fold. (A) Sedimentation velocity (SV) distribution analysis in terms of *c*(S) at 0.4 mg/mL. In-set is the resultant concentration dependence of the SV distribution. **(B)** Concentration dependence of hydrodynamic radius obtained from DLS measurements. **(C)** The pair distribution function versus particle radius obtained from the GNOM analysis. In-set is the merged scattering data obtained from multiple concentrations. **(D)** Superimposition of the human OAS1 (PDB 4IG8) high-resolution structure [222] on the *ab initio* model generated using DAMMIF on the data obtained from SAXS experiments on human OAS1. Published: Deo, S. *et al.* (2014) PLoS One 9: e92545 [211].

reconstruction of OAS1 was performed and the goodness of fit parameter (χ value) of ~0.9 was obtained for each individual model, signifying excellent agreement between the experimental scattering data and the calculated scattering data. The superimposed *ab initio* models provided an averaged model that was highly similar to each individual model in terms of shape as evidenced by normalized spatial discrepancy (NSD) parameter of 0.52±0.02 (**Figure 3.1D**). The recently determined high-resolution structure of human OAS1 superimposed almost perfectly on the averaged *ab initio* model of OAS1 [222] (**Figure 3.1D**). We additionally validated our *ab initio* modeling approach using the program BUNCH, that generated solution conformations of OAS1 based on existing high-resolution structural information that compared favorably with the *ab initio* models (**Table 3.1**). Although BUNCH could be used to generate solution conformations using partial high-resolution structure of a biomolecule, in this case the BUNCH was used to generate models from the complete high-resolution structure. The models obtained from BUNCH supported the *ab initio* models generated from SAXS. Furthermore, excellent agreement was observed between the experimentally determined hydrodynamic parameters from AUC, DLS and SAXS and the parameters calculated from *ab initio* and BUNCH models of solution conformations using the program HYDROPRO (**Table 3.1**). Hydrodynamic parameters calculated based on the previously published high-resolution structure of OAS1 are also in good agreement with the SAXS-derived models.

3.2.1.2 Solution conformation of the SLI/II/III of 5'-TR of WNV genome

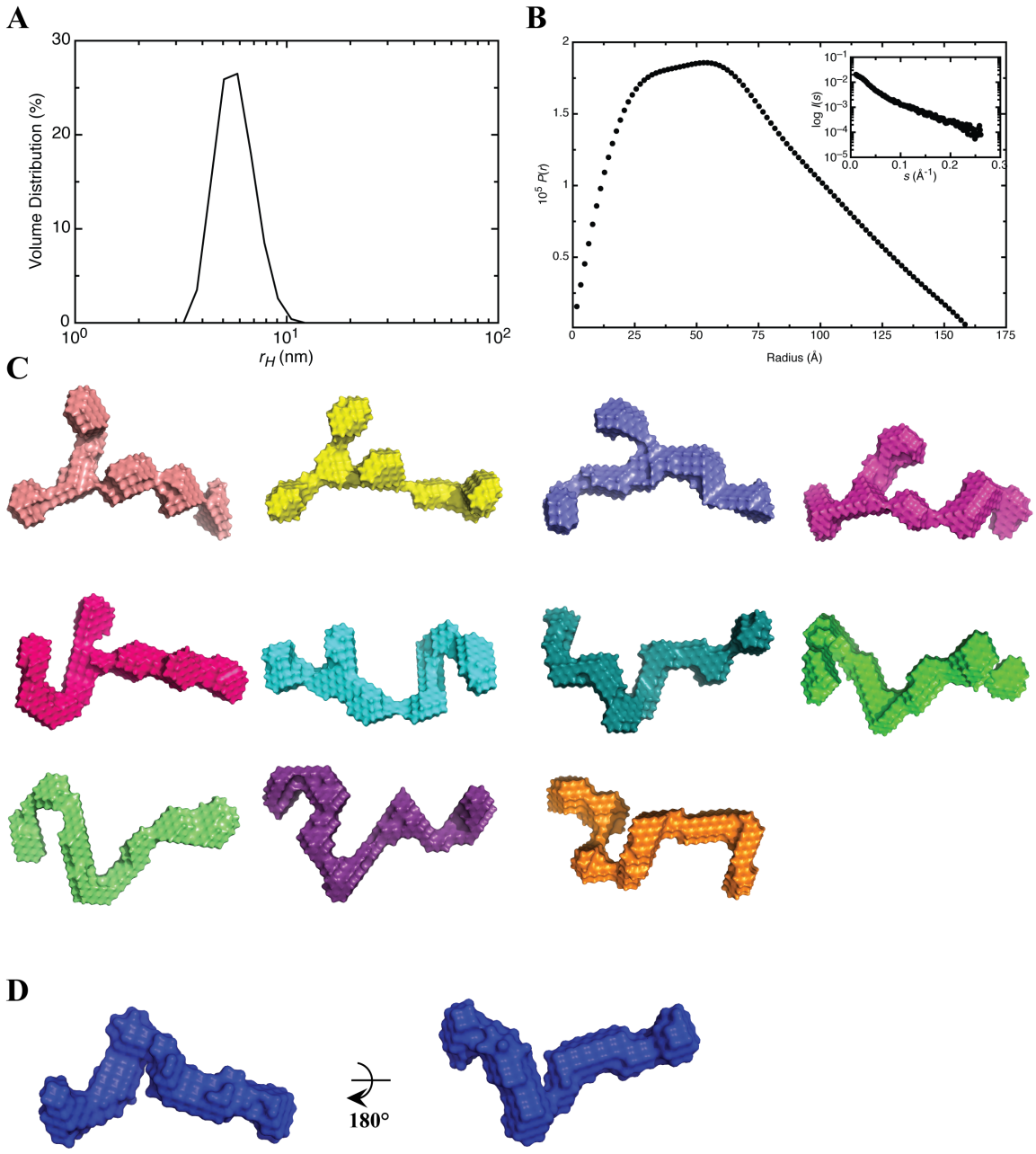

Figure 3.2 Solution conformations of the WNV 5'-TR from SAXS. (A) Dynamic light scattering profile of 5'-TR at 2 mg/mL. **(B)** Pair distribution function of 5'-TR obtained from merged data of multiple concentrations. In-set is the merged SAXS data obtained from multiple concentrations. **(C)** Individual *ab initio* models calculated from the SAXS data using DAMMIF program demonstrating two distinct subpopulations of the RNA molecule. (**D**) Averaged model of 5'-TR obtained from

individual models presented in **Figure 3.2C.** Published: Deo, S. *et al.* (2014) PLoS One 9: e92545 [211].

While RNAse probing experiments are consistent with the predicted secondary structure for the 5'-TR (SLI/II/III) of WNV, the three-dimensional structure of this RNA region is not known. We therefore *in vitro* transcribed WNV 5'-TR (nucleotides 1–146, including the 5′-UTR and initial coding region) for the purpose of determining the solution structure by SAXS. Denaturing gel electrophoresis demonstrated a single band of appropriate size (data not shown), and DLS analysis confirmed that the sample was monodisperse with an r_H of 5.1±0.2 nm (**Figure 3.2A**). Raw SAXS data acquired at multiple concentrations were merged (**inset Figure 3.2B**) and the pair distribution function analysis yielded D_{max} of 16 nm and r_G of 5.1±0.1 nm (**Figure 3.2B, Table 3.1**). Interestingly, a number of alternative conformations of the 5'-TR in solution were observed from the *ab initio* analysis of SAXS data with identical D_{max} and r_G values (**Figure 3.2C**). This observation can likely be attributed to the underlying flexibility of the RNA molecule in solution. In a number of the determined solution conformations, three distinct protrusions are observed which may correspond to the three stem-loops SLI SLII, and SLIII. **Figure 3.2D** presents the averaged model obtained from superimposing the individual *ab initio* models calculated for 5'-TR. Calculated hydrodynamic properties (r_H, r_G and D_{max}) of the 5'-TR were determined based on the *ab initio* models, and excellent agreement was found with the experimentally determined hydrodynamic properties (**Table 3.1**).

3.2.1.3 The 5'-TR of WNV interacts with and activates OAS1 *in vitro*

The 5'-TR of the WNV genome is comprised of three double-stranded stem loops. We sought to determine whether this region of the genome could bind to and activate OAS1 *in vitro*. EMSA experiments of the 5'-TR under non-denaturing conditions demonstrated that the RNA interacts with human OAS1 (**Figure 3.3A**).

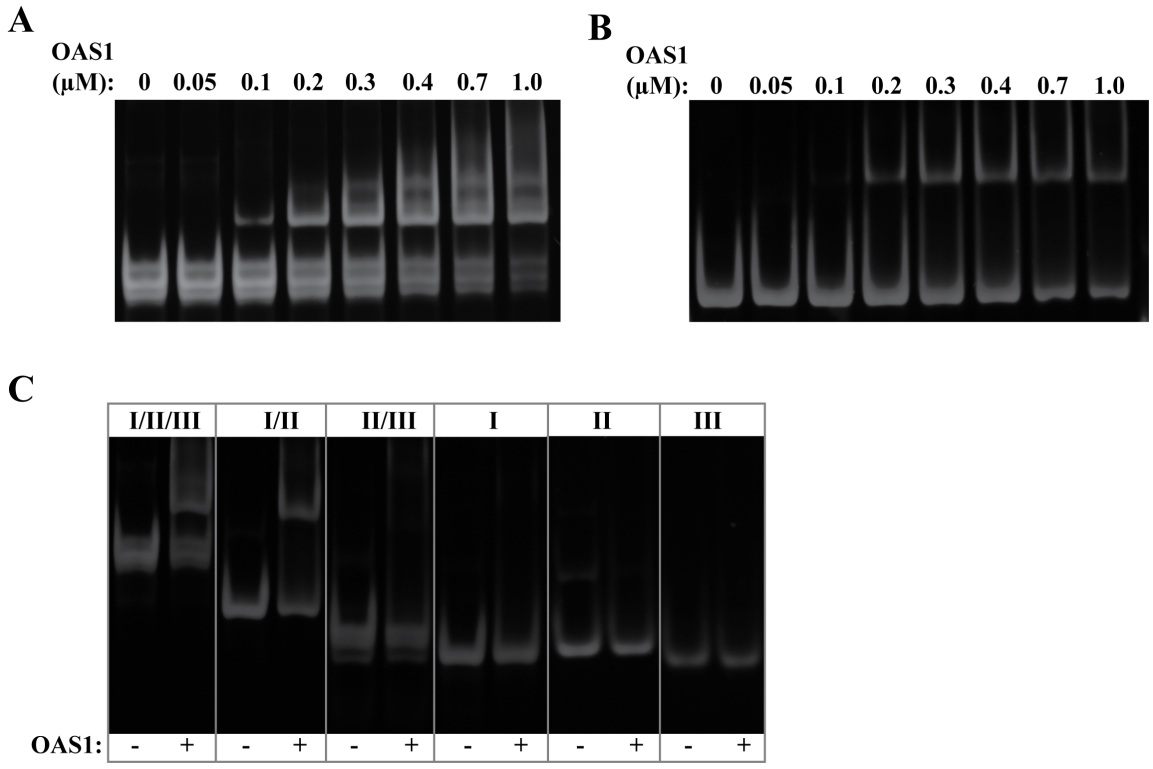

Figure 3.3 The WNV 5'-TR forms a direct interaction with human OAS1. (A) EMSA for OAS1 (100 nM) binding to the 5'-TR (nucleotides 1-146) under non-denaturing conditions. **(B)** EMSA for OAS1 (100 nM) binding to SLII+III under non-denaturing conditions. **(C)** Non-denaturing gel electrophoresis of 5'-TR truncations (100 nM) in the presence or absence of OAS1 (400 nM). In all cases, 8% native TBE gels were used and stained with Sybr® Gold (Invitrogen, USA) to visualize RNA-containing species. Published: Deo, S. *et al.* (2014) PLoS One 9: e92545 [211].

With increasing concentrations of OAS1, the 5'-TR is shifted into a higher molecular

weight complex of increasing intensity. Interestingly, unbound 5'-TR (**Figure 3.3A,** lane 1) displays heterogeneity under native conditions consistent with the subspecies observed by SAXS. This heterogeneity is not observed on a denaturing TBE gel (data not shown). To identify the specific region(s) within the 5'-TR that interacts with OAS1, we generated five different RNA molecules in addition to the 5'-TR region that represent either two stem loops in combination (SLI/II, SLII/III) or individual stem loops (SLI, SLII and SLIII). We believe this truncation approach is feasible based on the predicted secondary structure and our observed solution conformation of the 5'-TR (SLI/II/III). Complex formation with increasing OAS1 concentration was then performed for each RNA molecule in order to determine which secondary structural elements mediated the interaction. We observed significant complex formation that appeared as a high molecular weight species in the EMSA of SLI/II with OAS1 (**Figure 3.3B).** At a constant RNA concentration of 100 nM, no detectable complex formation was observed with any individual stem loop (SLI, SLII, or SLIII or with the pairwise combination of SLII/III in the concentration range of 0 to 1 μM of OAS1 (**Figure 3.3C).**

Upon establishing a direct interaction between the 5'-TR of WNV and OAS1 *in vitro*, we were further interested to investigate whether this interaction leads to activation of OAS1 catalytic activity. A colorimetric assay was performed which correlates the detection of pyrophosphate (PPi) with the production of 2′-5′(A) chains. We prepared buffered reactions containing OAS1, ATP, and Mg^{2+} in the presence of 5'-TR, polyinosinic-polycytidylic acid (poly I:C, a positive control synthetic dsRNA activator of OAS1), or a single-stranded RNA (ssRNA) negative

control. The experiments were performed over a 120-minute period, followed by progressive measurement of PPi production (**Figure 3.4A**). As expected, ssRNA negative control demonstrated no significant stimulation of OAS1 activity. The 5'-TR activates OAS1 to a level that is approximately 60% of that achieved by poly I:C at all time points observed (on a per mass basis). However, direct quantitative comparison to the poly I:C control should be treated with caution given the extremely large size and heterogeneity of poly I:C (~90 to 1400 kDa) relative to the WNV RNAs examined. Taken together, the structured 5'-TR (SLI/II/III) of the WNV genome interacts with and activates OAS1 *in vitro*.

3.2.1.4 SLI of 5'-TR is dispensable for maximal OAS1 activation

To compare the ability of the stem loop regions of the 5'-TR (SLI/II/III) to activate OAS1, time courses monitoring of PPi production were performed and compared with the full-length5'-TR, poly I:C (positive control) and ssRNA (negative control). Remarkably, of all the 5'-TR truncations, only SLII/III is capable of achieving activation level comparable to the full length 5'-TR (**Figure 3.4A**). Basal levels of PPi production, comparable to the negative control, were observed for SLI/II and each of the individual stem loops (SLI, SLII, and SLIII). Interestingly, the SLI/II construct that demonstrated high affinity complex formation with OAS1 did not stimulate catalytic activity, while SLII/III demonstrated potent activation despite a lack of detectable complex formation. Due to the observed discrepancy between binding and activation, detailed dose-response experiments in which initial reaction velocities of OAS1-catalyzed PPi production were performed under increasing RNA

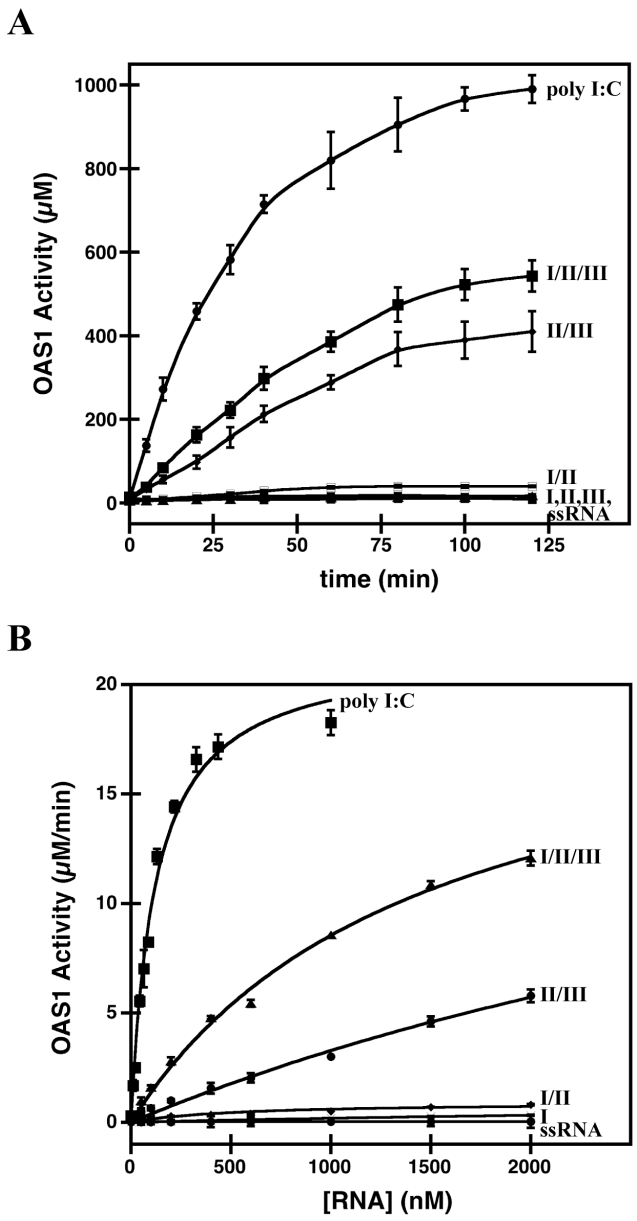

Figure 3.4 Catalytic activation of OAS1 by the 5'-TR and its truncations. (A) Purified OAS1 (300 nM) and RNA (300 nM) were incubated in the presence of ATP (2 mM) and $MgCl_2$ (5 mM) at 37 °C, quenched at time points from 0-180 minutes, and 2-5(A) chain formation quantitated by PP_i detection. In all cases, errors represent the standard deviation from at least 3 replicates, and ssRNA represents a single-stranded negative control. **(B)** Enzymatic activity of OAS1 (400 nM) shown as a function of RNA concentration. Linear regression analysis of the initial velocity was used to determine OAS1 activity and the error in the analysis represented as error bars. Published: Deo, S. *et al.* (2014) PLoS One 9: e92545 [211].

concentrations for each of the 5'-TR constructs (**Figure 3.4B**). This approach allowed estimation of both the apparent dissociation constant (K_{app}), a measure of affinity, and the maximum reaction velocity (V_{max}), a measure of catalysis. **Table 3.2** summarizes the determined kinetic parameters for each RNA molecule, and includes a measure of the quality of the fit to the data (R_{fit}). The 5'-TR and SLII/III demonstrate potent stimulation of OAS1 activity (~200-fold enhancement relative to the ssRNA negative control for both) despite the 4-fold higher affinity for OAS1 shown by 5'-TR compared to the SLII/III. Despite having a V_{max} value approaching that of the negative control, the SLI/II RNA demonstrated a nearly 3-fold increase in affinity relative to the 5'-TR.

Table 3.2 Comparison of kinetic parameters (K_{app} and V_{max}) of enzymatic activity of wild type OAS1 when activated by 5'-TR WNV and its truncations.
Published: Deo, S. *et al.* (2014) PLoS One 9: e92545 [211].

RNA	K_{app} (nM)	V_{max} (μM/min)	R_{fit}
I/II/III	1453±199	21±2	0.997
I/II	528±96	0.9±0.2	0.994
II/III	5775±452	22±2	0.995
I	5832±387	1.3±0.3	0.997
II	NA	NA	NA
III	NA	NA	NA
ssRNA	83±65	0.1±0.1	0.347
Poly I:C*	121±13	21.6±0.8	0.995

doi:10.1371/journal.pone.0092545.t002

None of the individual stem loop structures reveals appreciable stimulation of OAS1 catalytic activity, and only SLI demonstrates detectable affinity (4-fold lower affinity than the 5'-TR). Together, the kinetic analysis supports a model where SLII/III is the minimal construct capable of OAS1 activation despite having a weak binding affinity for the enzyme.

3.2.1.5 Mutations to the dsRNA binding site disrupt activation of OAS1 by the 5'-TR

To confirm that OAS1 activation is an RNA-mediated effect, the binding affinity and catalytic activity of two point mutants of human OAS1 (R195E and K199E) were investigated. Based on the human OAS1 structure, these mutations are in the positively charged dsRNA-binding groove on the enzyme face distal to the active site [222]. To verify that the mutations did not disrupt the native protein conformation, we performed SAXS experiments on OAS1 R195E and K199E. The resultant pair distribution function plots for wild type and mutants were nearly identical (**Figure 3.5A**), and the determined r_G and D_{max} values were within error of the wild type results (data not shown). Therefore, we conclude that these mutations do not affect the solution conformation of OAS1.

As expected, higher molecular weight RNA-protein complexes were not observed in EMSAs of 5'-TR with increasing concentrations of R195E or K199E OAS1 (**Figure 3.5B**). We next investigated whether this loss of interaction had a similar impact on activation of OAS1 catalytic activity in the presence of 5'-TR. Time course experiments following 2′-5′(A) synthesis by the mutants in the presence of

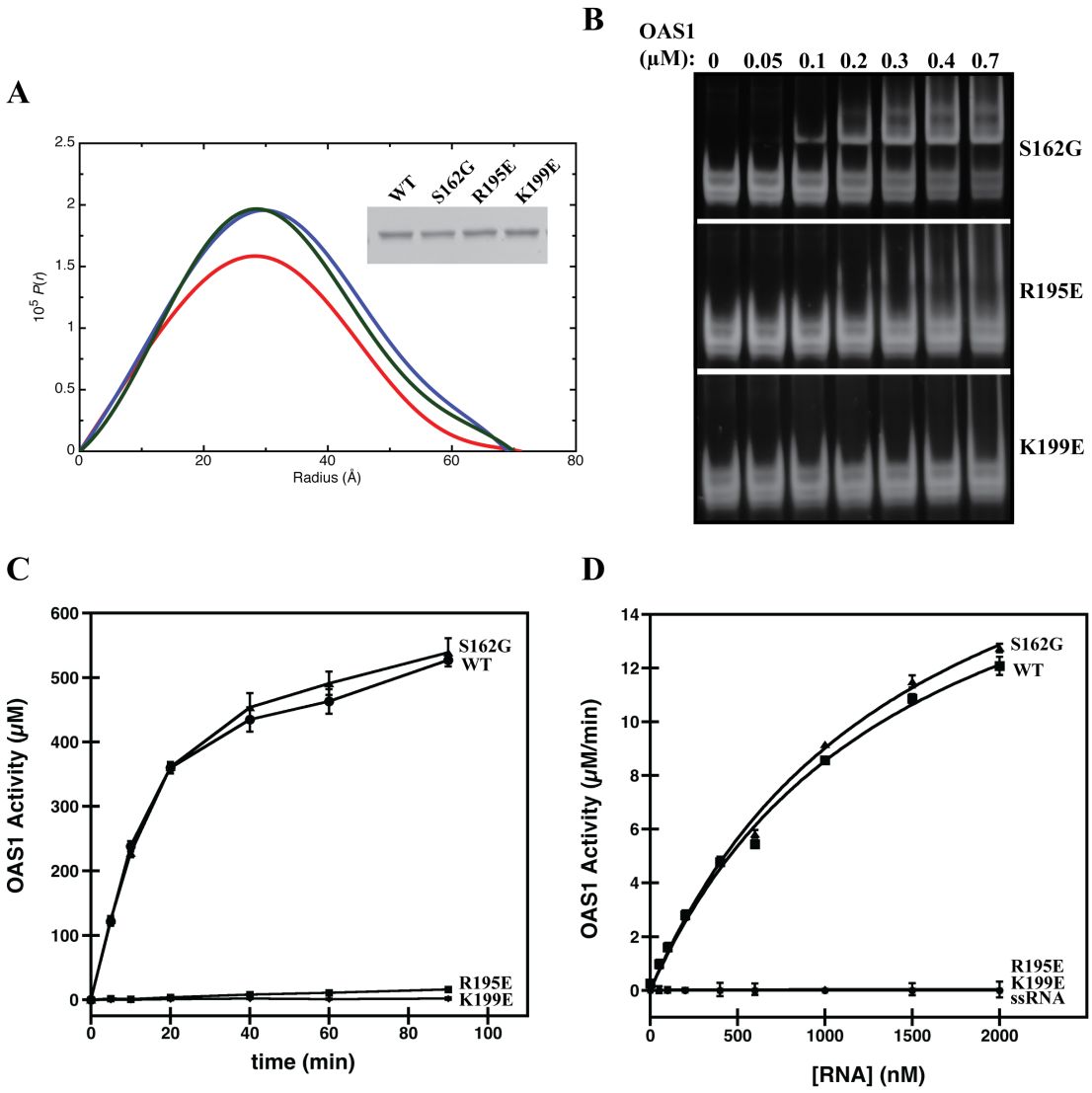

Figure 3.5 Analysis of OAS1 mutants. (A) Pair distribution function versus particle radius obtained from GNOM analysis for wild-type OAS1 (red), R195E (blue) and K199E (green). Inset, is a SDS-polyacrylamide gel presenting wild type and mutant OAS1s that suggests that all constructs have similar molecular weight. **(B)** EMSA for OAS1 and mutants (100 nM) binding to WNV 5'-UTR under non-denaturing conditions. **(C)** Reactions containing purified OAS1 or OAS1 mutants (300 nM) and RNA (300 nM) quenched at time points from 0-180 minutes followed by quantification of PP_i production. In all cases, errors represent the standard deviation from at least 3 replicates, and ssRNA represents a single-stranded negative control. **(D)** Enzymatic activity of OAS1 or OAS1 mutants (400 nM) shown as a function of RNA concentration. Linear regression analysis of the initial velocity was used to determine OAS1 activity and the error in the analysis represented as error bars. Published: Deo, S. *et al.* (2014) PLoS One 9: e92545 [211].

5'-TR (**Figure 3.5C**), SLII/III (data not shown), or poly I:C (data not shown) confirmed the expected attenuation of catalytic activity. For example, at the 90-minute time point, the R195E and K199E mutants demonstrated 3% and 0.4% of wild type activity respectively, in the presence of 5'-TR. In an attempt to quantitate the impact, initial reaction velocities for wild type, R195E and K199E OAS1 were determined in a dsRNA dose response experiment using 5'-TR as the activator (**Figure 3.5D**). The low levels of catalytic activity demonstrated by the R195E and K199E mutants made accurate parameter determination impossible (**Table 3.3**). Therefore, we conclude that the 5'-TR of WNV is mediating its effects through interaction with the previously reported dsRNA-binding site on OAS1 [222].

Table 3.3 Comparison of kinetic parameters (K_{app} and V_{max}) of enzymatic activity of wild type and mutant OAS1s when activated by the WNV 5'-TR.
Published: Deo, S. *et al.* (2014) PLoS One 9: e92545 [211].

OAS1	K_{app} (nM)	V_{max} (μM/min)	R_{fit}
WT	1453±199	21±2	0.997
S162G	1490±188	22±2	0.998
R195E	NA	NA	NA
K199E	NA	NA	NA

doi:10.1371/journal.pone.0092545.t003

3.2.1.6 Single nucleotide polymorphism in the OAS1 gene does not impede activation by dsRNA

The S162G mutation has been reported in a previous study as a very common single nucleotide polymorphism (SNP) in the OAS1 gene, and is more prevalent in WNV-susceptible individuals [335]. We therefore purified the mutant version of the protein, and investigated its ability to bind to and be activated by the 5'-TR of WNV. Overall, no significant differences were observed for this mutant in terms of solution conformation (**Figure 3.5A**), affinity for 5'-TR (**Figure 3.5B**), or ability to perform catalysis in the presence of dsRNA (**Figure 3.5C, 3.5D**). These results are not surprising as this SNP is located on the face opposite the active site aspartic acids and does not mediate interactions with dsRNA [222,335]. A comparison of the determined kinetic parameters is shown in **Table 3.3.**

3.2.1.7 Attempts at validation of 5'-TR interaction with OAS1 in mammalian cells

The EMSAs showed that the OAS1 interacts with 5'-TR, which was also supported by kinetic studies. We also purified OAS1+5'-TR complex using a size exclusion chromatography. As an effort to validate the *in vitro* results, we next attempted to demonstrate the interaction in a cellular context. While we did not investigate the interaction in WNV-infected cells due to safety concerns, we did attempt to confirm interactions of OAS1 and 5'TR in human tissue culture cells. We performed pull-

down assays using biotinylated 5'-TR in HEK 293T human cell lysates where OAS1 was overexpressed. For both the pull-down and the cross-linking experiments, the 5'-TR and the control RNAs (BC200 and ssCCHF respectively) were biotinylated (at their 3' end) and the biotinylation efficiency was calculated by comparing the amount of free RNA on an EMSA in the presence of streptavidin, outlined in materials and methods (Section 2.7.2, **Figure 2.8**). The

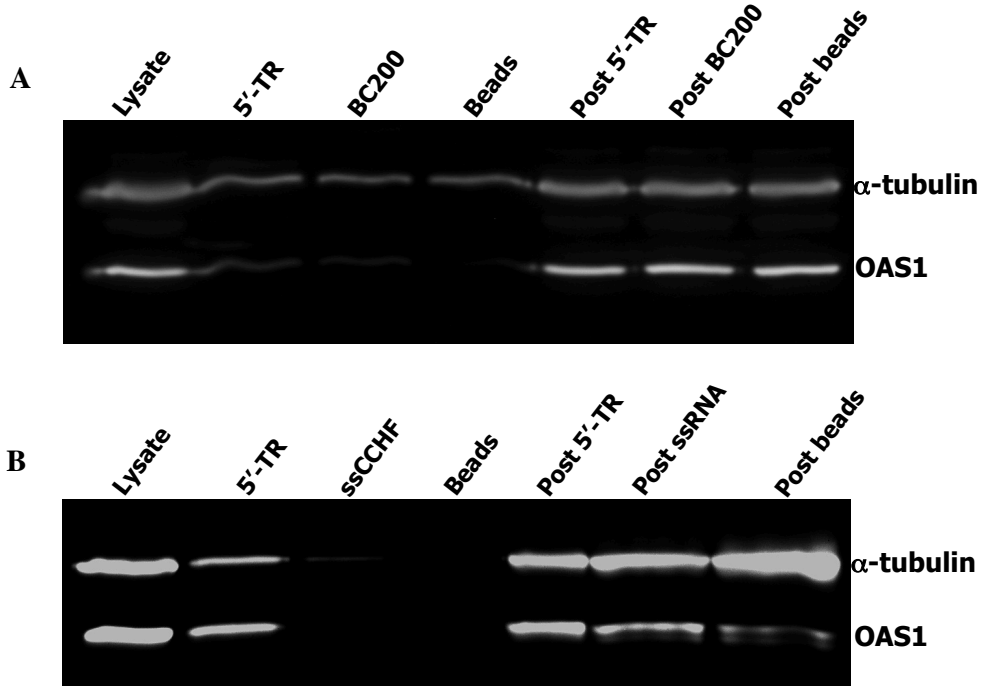

Figure 3.6 Attempts at validating interaction of 5'-TR and OAS1 in human cells. **(A)** Western blot of OAS1 pull-down assays performed with biotinylated 5'-TR, control RNA (BC200) and beads alone from HEK 293T cell lysate, where OAS1 has been over expressed. The western blot performed was also probed for α-tubulin. **(B)** Western blot of OAS1 performed on formaldehyde cross-linking experiments with OAS1 and biotinylated 5'-TR, ssCCHF (control) and beads alone. The western blot performed was also probed for α-tubulin.

amount of RNA used in the experiments was adjusted based on the biotinylation efficiency to keep the concentration of actual biotinylated RNA similar. The binding of 5'-TR to OAS1 was demonstrated (**Figure 3.6A**, lane 2), but there was a clear lack of preferential binding of the 5'-TR to OAS1 when compared to its binding to α-tubulin (negative control). The pull-down experiments were performed with

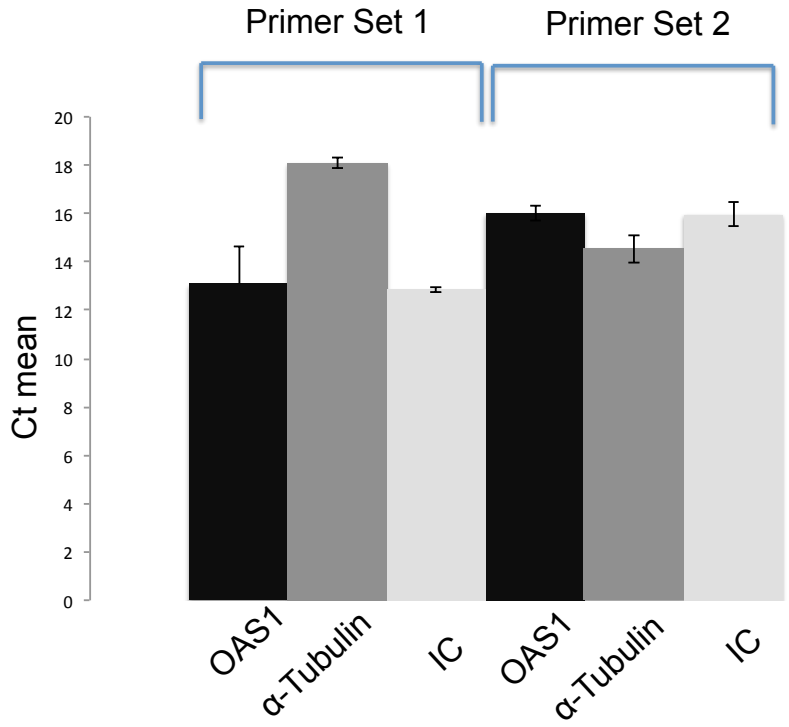

Figure 3.7 Co-immunoprecipitation of 5'-TR by OAS1 and RT-PCR performed. Two sets of primers used (set 1 and set 2 as described in section 2.7.7) didn't demonstrate preferential co-IP of 5'-TR compared to either the isotype control (IC) or the anti-α-tubulin antibody (negative control). As the controls didn't show consistent and significant difference, the Y-axis here is mean cycle threshold (Ct mean) instead of fold enrichment. Shown here is the average from three independent experiments and the standard deviation is represented as error bar.

adequate controls including BC200 (a 200 nucleotide human non-translated RNA) used as the negative control along with beads alone. BC200 showed marginally lower binding to OAS1 compared to the 5'-TR (**Figure 3.6A**, lane 2 and 3), which raises more doubt on the preferential binding of the TR RNA with OAS1.

The interaction of 5'-TR with OAS1 in the cellular context was also investigated using formaldehyde as a cross-linking reagent (**Figure 3.6B**). Samples from cross-linking experiments of OAS1 with biotinylated 5'-TR and subsequent pull-down using streptavidin magnetic beads was successful, however it was comparable to the cross-linking efficiency to α-tubulin (negative control). The negative control RNA (BC200) showed little cross-linking to both OAS1 and α-tubulin. Lack of specificity may be a result of higher RNA concentration used in the cross-linking experiments to overcome the weak affinity (in μM) of OAS1 for the TR RNAs.

We also performed RT-PCR to investigate preferential binding of 5'-TR with OAS1 by immunoprecipitation using cells that overexpress OAS1-6XHA tag protein. Similar immunoprecipitation experiments were performed for isotype control and anti-α-tubulin antibody. Our results showed no clear enrichment of 5'-TR RNA in the samples from anti-6X His antibody specific for OAS1 compared to samples from isotype control and the negative control (anti-α-tubulin antibody) (**Figure 3.7**). The PCR prodcuts were subjected to agarose gel electrophoresis to ensure specificity of the reaction.

3.2.2 DISCUSSION

OAS1 and other OAS isoforms play an important role in the recognition of viral dsRNA and subsequent amplification of the initial interferon-mediated innate immune response [186,387-389]. Previous studies have linked SNPs in the OAS1 gene to susceptibility to WNV infection [331,332]. The p42 isotype of OAS1 used our studies has been previously implicated to combat Dengue virus infection via an RNase L dependent pathway [244]. No direct enzymatic activation studies of OAS1 by regions of the WNV genome had been previously performed. We therefore sought to investigate whether the WNV RNA genome served as a source for OAS1 activation. Our initial investigations focused on the 5'-TR, based on its secondary structure that is conserved amongst *Flaviviridae* family members. We conclude that a direct interaction between the 5'-TR of the WNV and OAS1 occurs *in vitro*, and therefore warrants further investigation in a cellular context. We wanted to show these interactions in cellular context but our attempts to pull-down OAS1 from HEK 293T cell lysate using biotinylated 5'-TR RNA failed to show preferential binding of the OAS1 to the 5'-TR compared to a house keeping gene product. Experiments to quantify preferential binding of 5'-TR RNA to the OAS1 by RT-PCR was inconclusive as there was no difference in the RNA enrichment with anti-6X His antibody specific for OAS1 over expressed in mammalian cells compared to controls (isotype and anti-α–tubulin antibody).

Our study found that the 5'-TR (SLI/II/III) of WNV is a potent activator of OAS1 *in vitro*. The affinity of OAS1 for the 5'-TR (K_{app} of 1453±199 nM) is consistent

with affinities for other short viral RNAs [212], and the maximum catalytic activity (V_{max} of 21±2 μM/min) is within error of the positive control (synthetic poly I:C) (**Table 3.2**). Examination of various 5'-TR truncations enabled a comprehensive analysis of RNA binding and activation potential to narrow down sufficient region(s). In tandem SLII/III are necessary for catalytic activation of OAS1 despite the requirement of SLI in conjunction with SLII for the highest affinity interaction. Stem loops SLII/III has a higher K_{app} that shows weaker binding, which is supported by absence of any higher species in its EMSA in presence of OAS1 but also has a high V_{max} comparable to poly I:C and 5'-TR of WNV. This result supports previous observations that indicate that binding affinity does not necessarily correlate with the ability of an RNA molecule to stimulate the synthetase activity of OAS1; instead balance between sufficient affinity and stimulatory potential is the key [212,213]. Overall, the 5'-TR appears to achieve the best balance, but the construct lacking SLI is capable of achieving a similar maximum catalytic output to the full length 5'-TR at higher RNA concentrations (**Table 3.2**).

Western blots performed on OAS1 pull-down assays using biotinylated 5'-TR, from HEK 293T cell lysate (OAS1 overexpressed), with and without cross-linking, resulted in similar observations, where the 5'-TR failed to show preferential interaction with OAS1 in comparison to α-tubulin. We also performed RT-PCR to investigate preferential binding of 5'-TR with OAS1 by immunoprecipitation of the 6X His tagged overexpressed OAS1. Our result showed no clear enrichment of 5'-TR RNA in the samples from anti-6X His antibody specific for OAS1 compared to those from isotype control or anti-α-tubulin antibody (negative control) (**Figure 3.7**). As

the level of OAS1 in HEK 293T is barely detectable using anti-OAS1 antibody we had to overexpress the protein. Selection of a cell line where OAS1 is expressed at a higher level may be useful in showing the interaction between 5'-TR and the OAS1. UV cross-linking could be attempted as an alternative to formaldehyde cross-linking to validate the interaction between 5'-TR and the OAS1. It will be better to validate the interaction by performing pull-down assays with biotinylated 5'-TR and cell lysate from WNV infected cells. Alternatively, biotinylated 5'-TR could be transfected into WNV infected cells, followed by cell lysis and pull-down assays performed. The visualization of the interaction would be performed using Western blotting. The ideal approach will be to transfect WNV infected cells with 5'-TR, performing a Co-IP with anti-OAS1 antibody followed by RT-PCR to show preferential enrichment of the 5'-TR in comparison to Co-IP with isotype control antibody and anti- α-tubulin antibody (negative control).

We studied two point mutations in OAS1 within the RNA binding domain on the basic tract opposite to the active site [217,222]. These mutations did not impact the overall structure of OAS1 as determined by SAXS experiments (**Figure 3.5A**). As expected, these mutants show no detectable affinity for WNV 5'-TR, nor do they activate the catalytic activity of OAS1 (**Table 3.3**). This finding supports a previous study highlighting the importance of R195 and K199 residues in the proposed dsRNA binding site of OAS1 and confirms that dsRNA binding via these basic residues is crucial to the impact of WNV RNA on OAS1 activation [217]. Furthermore, this result highlights that while the RNA-protein interaction observed is in the μM range for the 5'-TR, this affinity is more than sufficient for a dsRNA

activator to activate OAS1.

Genome cyclization has been established as necessary for WNV genomic RNA replication, and involves a panhandle structure comprising long-range base pairing interactions between nucleotides in the 5'-TR (5′-UAR in SLII and 5'-CS in SLIII and their complimentary nucleotides in 3'-UTR [303-305]. For genome cyclization to occur, both SLII and SLIII in the 5'-TR unwind to form their new interactions. RNAse probing experiments have shown that while SLII and SLIII do adopt these long-range interactions, SLI of the 5'-TR remains intact upon cyclization [296]. Our observations that the RNA construct comprising SLII/III is sufficient for maximum catalytic activation of OAS1 is particularly interesting in this context, as we hypothesized that the replication-competent conformation of the 5'-TR could potentially evade the OAS1-mediated innate immune response. In chapter IV a detailed biophysical characterization of the panhandle (5'/3'-TR) formation and the interaction of this 5'/3'-TR complex with the OAS1 is presented.

Although SAXS represents a low-resolution approach, the results presented are the first direct structural observation of the 5'-TR from the WNV genome. The determined SAXS models of the 5'-TR RNA suggest an inherently flexible molecule in solution. One subset of these conformations presented three distinct protrusions (that likely correspond to SLI, SLII, and SLIII respectively), whereas the remaining models lack domain resolution (**Figure 3.2C**). The averaged solution conformation (**Figure 3.2D**) has a relatively low NSD value (1.10±0.06), suggesting that these conformations are closely related to each other structurally. The most

straightforward interpretation of these data is that a dynamic equilibrium between these conformations exists, and this idea is supported qualitatively by native gel electrophoresis where at least two distinct RNA conformations are observed. Given that genome cyclization with complimentary regions in the 3'-TR would require unwinding of both SLII and SLIII in the 5'-TR, it is enticing to speculate that our observed conformations represent the “structured” and “partially unwound” 5'-TR conformations. As the structural features of the WNV 5'-TR RNA appear conserved amongst other *Flaviviridae* family members at the secondary structural level [296,298,299], the stem-loop recognition at the 5'-end observed in this study by OAS1 may possibly represent a general feature of OAS enzymes.

CHAPTER 4: PART II OF RESULTS- CHARACTERIZATION OF THE TERMINI OF THE WEST-NILE VIRUS GENOME AND THEIR INTERACTIONS WITH OAS1

The results presented here are in press to be published in a peer-reviewed journal: Deo S, Patel TR, Chojnowski G, Koul A, Dzananovic E, McEleney K, Bujnicki JM and McKenna SA (2015) Characterization of the termini of the West Nile virus genome and their interactions with the small isoform of the 2′ 5′-oligoadenylate synthetase family. J. Structural Biol. doi:10.1016/j.jsb.2015.04.005

4.1 INTRODUCTION

OAS are interferon-stimulated proteins that act in the innate immune response to viral infection. Upon binding viral double-stranded RNA, OAS enzymes produce 2'-5'-A chains that stimulate RNase L and ultimately slow viral propagation. Truncations/mutations in the smallest human OAS isoform, OAS1, results in susceptibility to West Nile virus (WNV). We have demonstrated (section 3.2.1.3) the interaction between OAS1 the 5'-TR of the WNV RNA genome [211]. Here we report that the 3'-terminal region is also able to mediate specific interaction with and activation of OAS1. Binding and kinetic experiments identified a specific stem loop within the 3'-TR that is sufficient for activation of the enzyme. The solution confirmation of the 3'-terminal region was determined by small angle X-ray scattering, and computational models suggest a conformationally restrained structure comprised of two stacked helices. Structural investigation of the 3'-

terminal region in complex with OAS1 is also presented. Finally, we show that genome cyclization by base pairing between the 5'- and 3'-TR, a required step for replication, is not sufficient to protect WNV from OAS1 recognition. The biophysical characterization of interaction between the 5'-TR and 3'-TR were also undertaken. We will be focusing on the 5'-TR and its interaction with OAS1 followed by studies performed on 3'-TR and 5'/3'-TR.

These data provide a framework for understanding recognition of the highly structured terminal regions of a flaviviral genome by an innate immune enzyme.

4.2 RESULTS AND DISCUSSION

4.2.1 RESULTS

4.2.1.1 5' and 3' terminal regions of the WNV genome form a stable base paired structure

Genome cyclization through creation of a panhandle structure between the 5'- and 3'- terminal regions is needed for negative strand synthesis, and this requirement has been reported for many flavivirus genomes, including WNV [296,302,303,305-307]. To characterize the conformational change that occurs to the terminal regions of the WNV genome upon panhandle formation, we *in vitro* transcribed and purified both the 5'-TR (nt 1 to 146) and 3'-TR (nt -1 to -111). In a previous study we have reported that the 5'-TR adopts two distinct conformations in solution [211]. Unlike the 5'-TR, the 3'-TR adopts a compact single band on the native TBE gel (**Figure 4.1A**, lane 2). To study 5'/3'-TR complex formation, increasing concentrations of 5′-

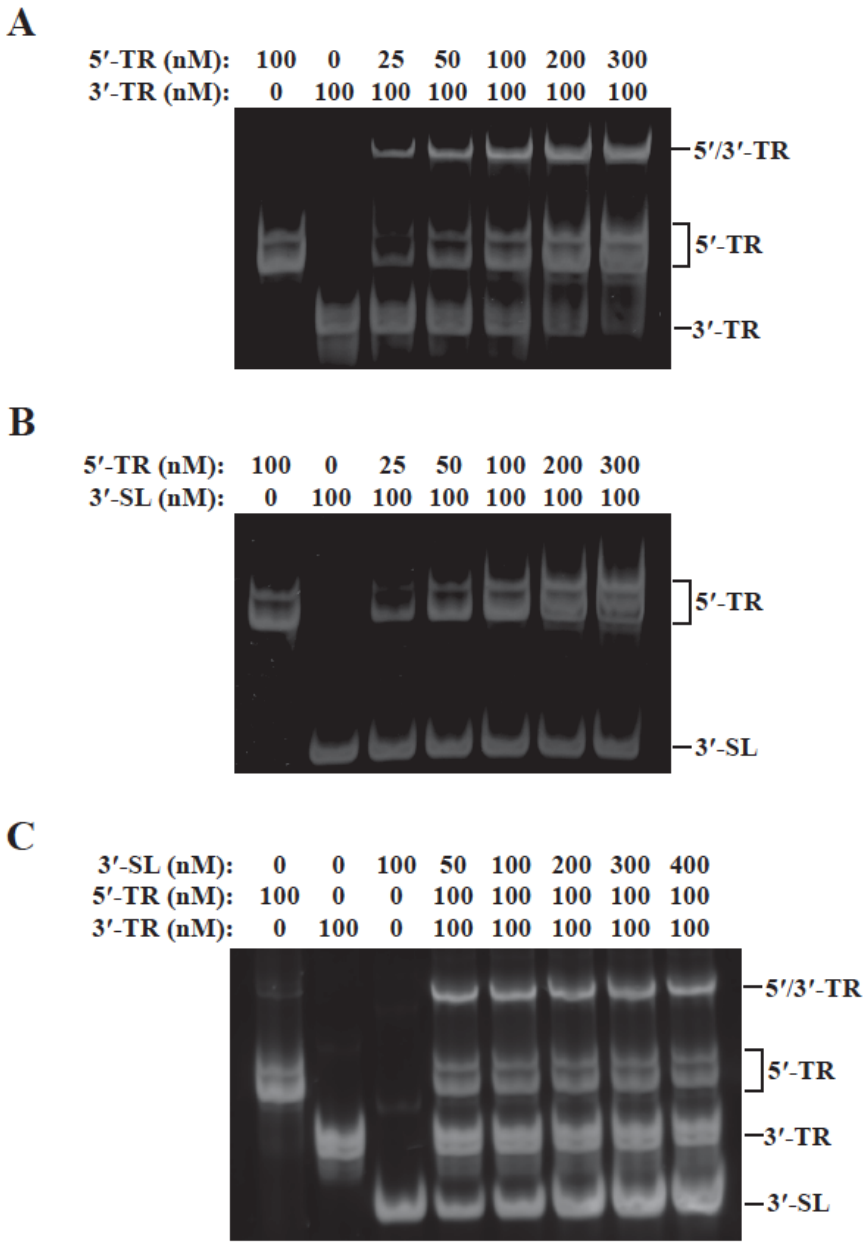

Figure 4.1 5'-TR and 3'-TR of WNV interact to form 5'/3'-TR RNA complex. Electrophoretic mobility shift assay on an 8 % TBE gel. **(A)** 3'-TR at 100 nM with increasing concentration of 5′-TR (0 to 300 nM) shows the formation of 5'/3'-TR complex (top band). (**B)** Higher order species are absent on the EMSA performed with 3′-SL at 100 nM with increasing concentration of 5'-TR (0 to 300 nM from lane 3 to 7). **C.** Competition assay showing the result of addition of 3'-SL (0 to 400 nM) to a mixture of 5'-TR and 3'-TR (both terminal regions at 100 nM). Increasing concentration of 3'-SL do not change the amount of 5'/3'-TR complex (top band). Deo, S. *et al.* (2015) J. Structural Biol. doi:10.1016/j.jsb.2015.04.005

TR were added to 3'-TR and complex formation was monitored using native electrophoretic mobility shift assays (EMSA) as a higher molecular weight species (**Figure 4.1A**, lanes 3-7). Next, we produced a truncated version of the 3'-TR (3'-SL; nt -1 to -79) that lacks one of the two regions required for base pairing with the 5'-TR. No complex formation between the 5'-TR and 3'-SL was observed, confirming the importance of the 12 nt 3'-CS region to panhandle formation (**Figure 4.1B**). In competition experiments, the 3'-SL was unable to disrupt complex formation between the full 5'-TR and 3'-TR, confirming the specificity of the interaction (**Figure 4.1C**). Quantitative characterization of complex formation was then performed using isothermal titration calorimetry (ITC) of either the 3'-TR or 3'-SL into a sample cell containing 5'-TR. Clear complex formation was observed between the 5'-TR and 3'-TR, with an observed K_D of 32±1 nM (**Figure 4.2A**). Enthalpy (ΔH= -58±1 kcal/mol) and entropy (ΔS= -165±5 cal/mol•deg) measurements for complex formation are consistent with a predominantly electrostatic, as opposed to hydrophobic, mode of interaction. Consistent with EMSA results, no detectable complex formation between 3'-SL and 5'-TR was observed (**Figure 4.2B**). A stoichiometry of 0.4:1 (3'-TR:5'-TR) was determined by ITC, which we hypothesized may reflect interaction of the 3'-TR with only one of the observed 5'-TR conformations. To test this hypothesis and to further characterize the 5'/3'-TR complex, we used SEC to purify it away from unbound 5'-TR and 3'-TR under equimolar conditions (**Figure 4.2C**). While the complex eluted as a single peak consistent with the observed increase in molecular weight studied by EMSA,

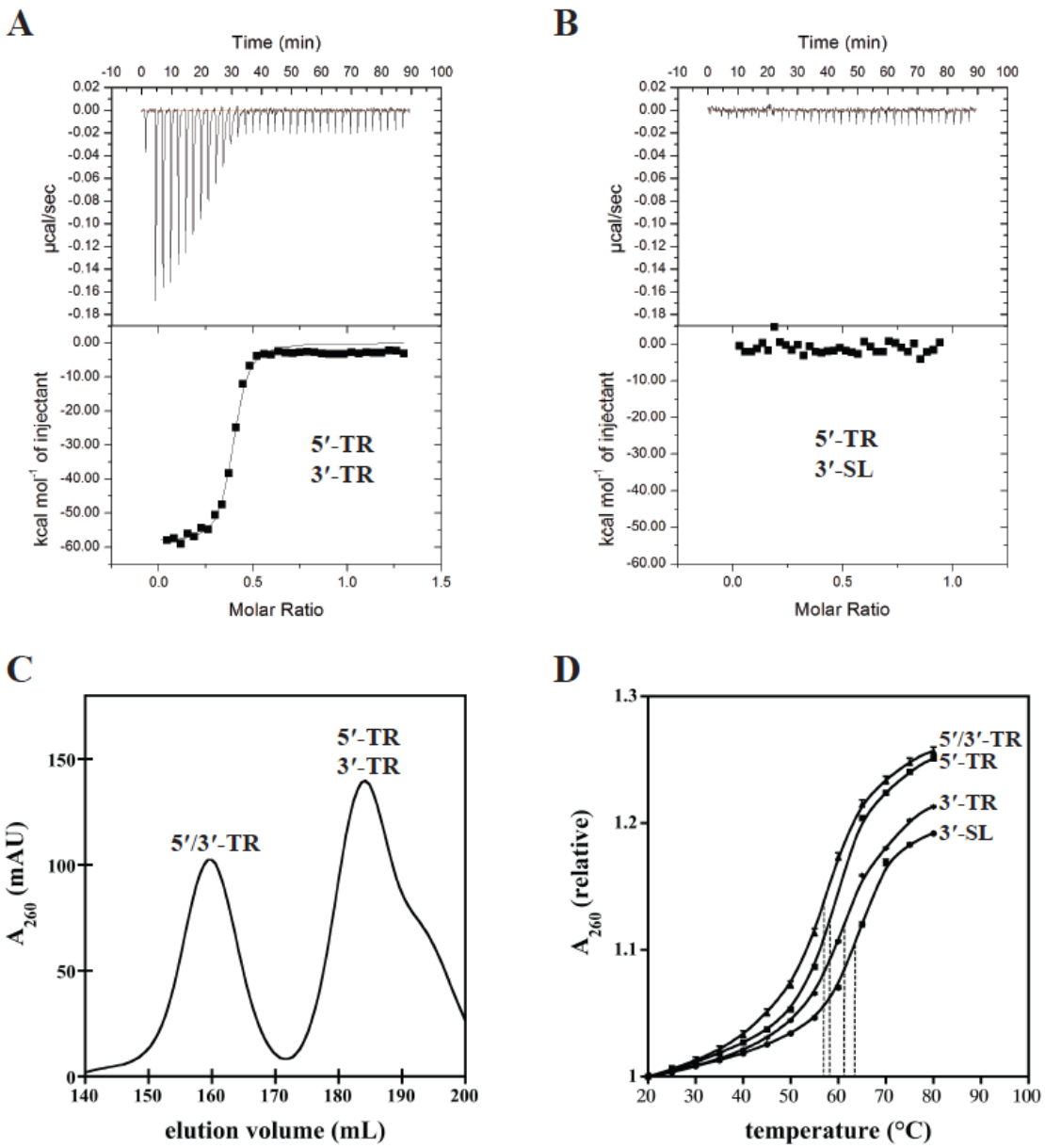

Figure 4.2 Biophysical characterization of complex formation between 5'-TR and 3'-TR. (A) Isothermal titration calorimetry showing interaction between 5'-TR (7.9 µM) in the sample cell and 3'-TR (72.4 µM). (**B)** ITC experiment with 3'-SL (62 µM) titrated into sample cell containing 5'-TR (8.84 µM). **(C)** SEC trace showing the 5'/3'-TR complex elution before the mixture of free 5'-TR and 3'-TR. (**D)** UV spectrometry melting curve measured at every 5 °C interval (temperature range 20 °C to 80 °C) of 3'-TR, 3'-SL, 5'-TR and 5'/3'-TR. Experiments were performed in triplicate and the standard deviation is shown as error bars. Deo, S. *et al.* (2015) J. Structural Biol. doi:10.1016/j.jsb.2015.04.005

significant amounts of the 5'-TR and 3'-TR remained uncomplexed. The area under the elution profile suggests qualitatively that 38% exists in the 5'/3'-TR complex,which is in good agreement with stoichiometry values obtained by ITC. To determine whether 5'/3'-TR complex formation offered a significant increase in stability relative to the individual terminal regions, thermal denaturation curves measuring hyperchromicity changes via UV spectrophotometry were performed (**Figure 4.2D**). The midpoint transition (*Tm)* calculated from the fit to the curves demonstrates similar stabilities of the 5'/3'-TR (57 °C), 5'-TR (58 °C), and 3'-TR (61 °C), suggesting that the 5'/3'-TR complex and individually structured terminal regions have similar stabilities. Interestingly, the 3'-SL had the highest *Tm* (63 °C) despite being the smallest construct and having the fewest predicted base pairs.

4.2.1.2 The 3'-TR of WNV adopts an extended dsRNA conformation in solution

RNase probing and NMR experiments are consistent with the predicted secondary structure for the 3'-TR [296,302]. The three-dimensional structure of this RNA region is unknown, including the potential interaction between dsRNA stem loop regions. We therefore *in vitro* transcribed and purified 3'-TR and 3'-SL to determine their solution structure by SAXS and computational modeling. Dynamic light scattering (DLS) analysis at multiple concentrations confirmed that the sample was monodisperse and that no self-association was detected over the concentration range employed for SAXS studies (**Figure 4.3A, Table 4.1**). SAXS data for each RNA was acquired at multiple concentrations and merged (**Figure 4.3B**) to generate the corresponding pair distribution function *P(r)* plot and determine the maximum

particle dimension (D_{max}) and radius of gyration (r_G) (**Figure 4.3C, Table 4.1**). The *P(r)* plots indicate that the 3'-TR and 3'-SL adopt an extended shape in solution with

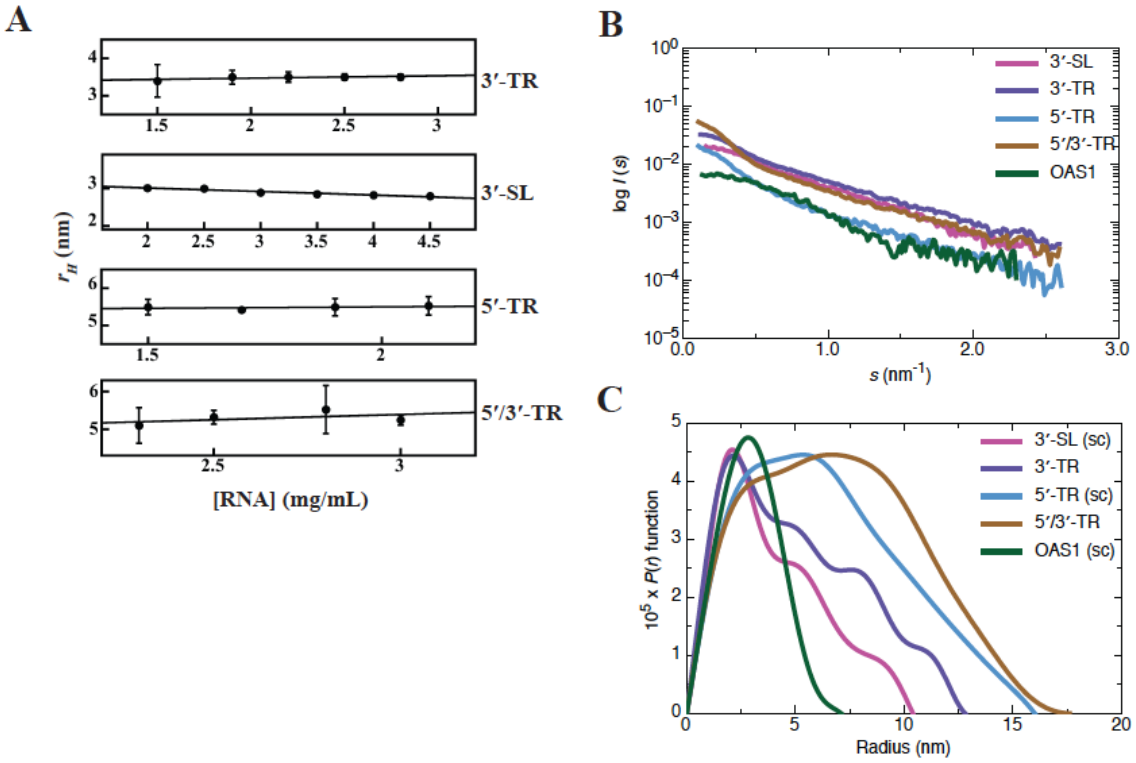

Figure 4.3 Dynamic light scattering and small angle X-ray scattering of 3'-SL, 5' and 3'-TR RNAs, 5'/3'-TR and OAS1. A. DLS measurements of 3'-TR (1.5-2.8 mg/mL), 3'-SL (2.0-4.5 mg/mL), 5'-TR (1.5-2.1 mg/mL) and 5'/3'-TR (2.2-3.0 mg/mL) at multiple concentrations to check for concentration dependence. **B.** Merged small angle X-ray scattering data obtained at multiple concentrations of 3'-TR (1.5, 2.0, 2.5 and 3.0 mg/mL), 3'-SL (1.6, 2.0 and 2.2 mg/mL), 5'/3'-TR (2.0, 2.5, 3.0, 3.5, 4.0 and 4.5 mg/mL) and previously published OAS1 and 5'-TR [211]. **C.** GNOM analysis of merged SAXS data generating pair distribution functions *P(r)* plotted against the particle radius. The D_{max} for RNA is measure in nm between the two points its *P(r)* plot meets the X-axis. Deo, S. *et al.* (2015) J. Structural Biol. doi:10.1016/j.jsb.2015.04.005

similar defined structural features corresponding to the observed shoulders in the plot. The major differences between them are that the 3'-TR has a modestly larger

D_{max} relative to the 3'-SL (12.8 nm vs. 10.4 nm), and that the shoulder centered at approximately 8.5 nm in the 3'-TR is absent in the 3'-SL. These differences likely reflect the removal of the short stem loop (3'-SS, nt -80 to -95) and single-stranded region at the 5'-end of the RNA (**Figure 1.5B**). Using D_{max} and r_G values as constraints, individual *ab initio* shape reconstructions of 3'-TR and 3'-SL were performed and had excellent agreement between the experimental scattering data and the calculated scattering data (χ value ~1.0) (**Table 4.1**). The averaged filtered model obtained from 20 individual *ab initio* models for the 3'-TR and 3'-SL are shown in **Figures 4.4A and 4.4B** respectively, with each demonstrating high similarity amongst individual models as evidenced by a very low normalized spatial discrepancy (NSD) (**Table 4.1**). Both RNAs adopt an extended conformation in solution, consistent with a conformationally restricted structure. Hydrodynamic properties (r_H, r_G and D_{max}) of individual RNA were calculated based on the *ab initio* models, and excellent agreement was found with the experimentally determined hydrodynamic properties (**Table 4.1**).

Table 4.1 Experimental and predicted hydrodynamic parameters in 50 mM Tris and 100 mM NaCl, pH 7.0.
Deo, S. *et al.* (2015) J. Structural Biol. doi:10.1016/j.jsb.2015.04.005

	3′-TR		3′-SL		5′-TR[d]		5′/3′-TR	
	Exp	DAMMIF[c]	Exp.	DAMMIF[c]	Exp.	DAMMIF[c]	Exp.	DAMMIF[c]
r_H (nm)[a]	3.46±0.06	3.62±0.02	3.18±0.03	3.22±0.02	5.10±0.02	5.00±0.02	5.30±0.17	5.13±0.07
r_G (nm)[b]	4.15±0.03	4.18±0.01	3.27±0.03	3.34±0.02	5.10±0.01	5.10±0.01	5.54±0.03	5.52±0.01
D_{max} (nm)[b]	12.80	14.00±0.01	10.40	11.00±0.01	16.00	16.80±0.01	17.60	17.80±0.01
χ	-	1.0	-	1.0	-	1.0	-	1.05
NSD	-	0.70±0.06	-	0.55±0.07	-	1.10±0.06	-	1.28±0.05

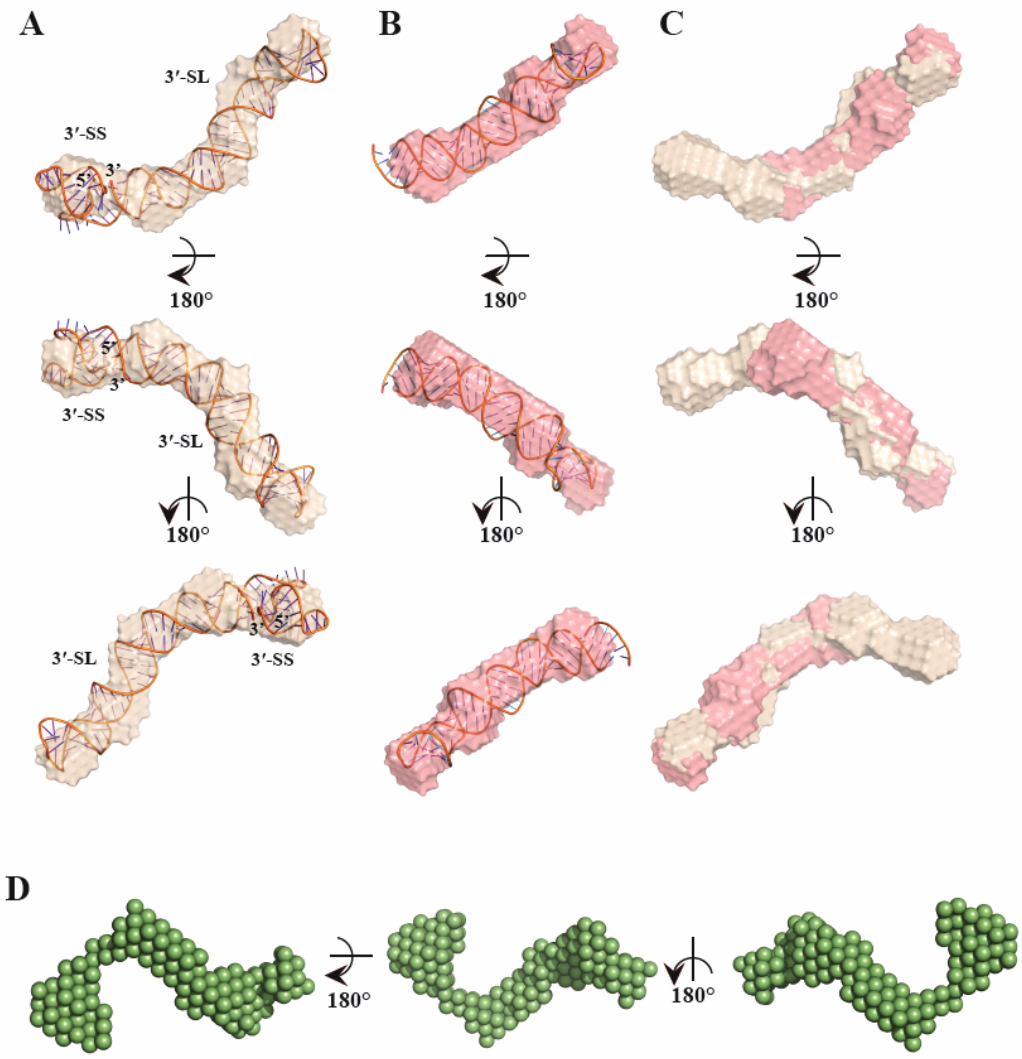

Figure 4.4 *Ab initio* and *3D* structure prediction of 3'-TR and 3'-SL: DAMMIF software was used to generate multiple *ab initio* models utilizing SAXS data as described in materials and methods. These *ab initio* models were averaged to obtain a single representative model. **(A)** Averaged (filtered) *ab initio* model of 3'-TR (center) rotated 180° on its X-axis (top) and Y-axis (bottom). This model is co-axially stacked on its computational model in a full-atom representation. **(B)** Averaged (filtered) *ab initio* model of 3'-SL (center) rotated 180° on its X-axis (top) and Y-axis (bottom). Co-axial stacking of 3'-SL full-atom structural model on its filtered *ab initio* model shown here. **(C)** Superimposed averaged *ab initio* models of 3'-SL and 3'-TR (center) rotated 180° on its X-axis (top) and Y-axis (bottom). **(D)** Averaged (filtered) *ab initio* model of 5'/3'-TR (center) rotated 180° on its X-axis (left) and Y-axis (right). Deo, S. *et al* (2015) J. Structural Biol. doi:10.1016/j.jsb. 2015.04.005

In particular, the good agreement between SAXS and DLS experiments with respect to r_H measurements were obtained.

Computational modeling using the SAXS data as restraints allowed generation of 3D structural models for both the 3'-TR and 3'-SL RNAs (**Figure 4.4A, B**). The 3'-TR stacks the base of the 3'-SL and 3'-SS hairpins in close proximity, created a bent and extended predominantly A-RNA helical structure. Both regions required for genome cyclization through panhandle formation with the 5'-TR, the 3'-CS and 3'-UAR, are involved in complex secondary dsRNA structures including helix formation as seen in this conformation. Modeling of the 3'-SL structure in isolation suggests that it adopts a single dsRNA helix in solution with similar features to the 3'-SL in the context of the 3'-TR construct. Confirming this observation, excellent superposition of the average solution conformation of the 3'-SL on the corresponding region in the 3'-TR RNA was observed, providing greater confidence on tertiary structure models obtained (**Figure 4.4C**).

4.2.1.3 5'/3'-TR complex adopts multiple conformations in solution

Solution conformations of purified 5'/3'-TR complex were determined using an identical approach as outlined for the 3'-TR constructs. DLS experiments performed at multiple concentrations presented sample monodispersity and absence of RNA self-association over the concentration range used for SAXS (**Figure 4.4A, Table 4.1**). SAXS data from multiple concentrations were merged (**Figure 4.3B**) and a pair distribution function *P(r)* lacking definition was obtained (**Figure 4.3C**). A D_{max} of 17.60 nm was obtained for the 5'/3'-TR, which is significantly larger than the 3'-TR

while only modestly larger than the 5'-TR (**Table 4.1**). *Ab initio* shape reconstruction was performed and the goodness of fit parameter (χ value) of ~ 1.05 was obtained for each individual model, signifying excellent agreement between the experimental scattering data and the calculated scattering data. Multiple models

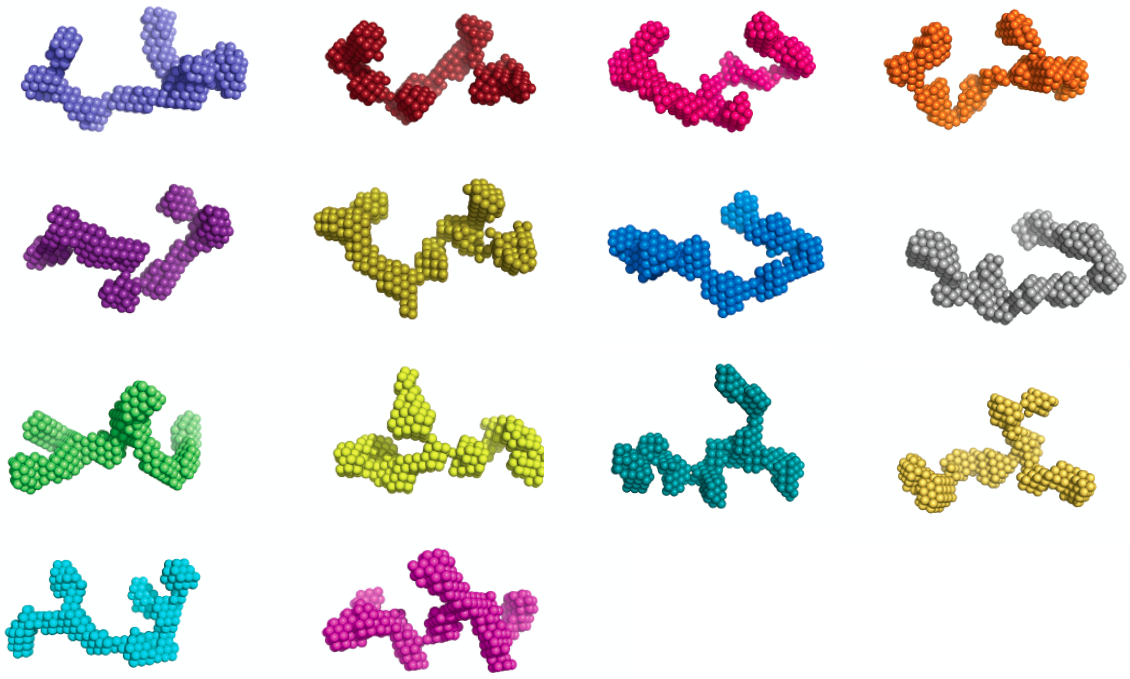

Figure 4.5 Individual *ab initio* models of 5'/3'-TR RNA: Models are generated by DAMMIF using SAXS data. All these *ab initio* models share the same SAXS generated parameters for example D_{max} and r_G but the flexibility in the 5'/3'-TR RNA is evident from fact that the RNA have multiple conformations. This leads to considerable loss of resolution of its solution conformation when averaging multiple ab initio models of the TR RNA complex. Deo, S. *et al.* (2015) J. Structural Biol. doi:10.1016/j.jsb. 2015.04.005

calculated from the same *P(r)* plot displayed a variety of conformations in solution, with distinct protrusions likely corresponding to stem loop structures (**Figure 4.5**). While many of the individual models looked alike by the naked eye, the averaged filtered model adopted an elongated conformation that lacked common structural features, and had an NSD parameter (1.28 ± 0.05) consistent with a lack of full convergence of individual models (**Figure 4.4C**). Given the single peak by SEC and a single band by native gel electrophoresis, we conclude that the 5'/3'-TR exists in dynamic equilibrium between multiple conformations in solution. Comparison between model-based and experimentally determined hydrodynamic properties (r_H, r_G and D_{max}) of the 5'/3'-TR RNA were in reasonable agreement (**Table 4.1**).

4.2.1.4 OAS1 is activated by the 5'/3'-TR, 3'-TR and 3'-SL RNAs

We have demonstrated that the WNV 5'-TR is capable of activating the catalytic activity of OAS1 *in vitro* [211]. We next investigated whether the 3'-TR, 3'-SL, and 5'/3'-TR complex could achieve similar levels of recombinant OAS1 activation using a colorimetric assay that correlates the detection of pyrophosphate (PPi) with the production of 2-5(A) chains. Time courses of buffered reactions containing OAS1, ATP, and Mg^{2+} were incubated in the presence of 5'-TR, 3'-TR, 3'-SL, 5'/3'-TR, polyinosinic-polycytidylic acid (poly I:C, a positive control synthetic dsRNA activator of OAS1), or a single-stranded RNA (ssRNA) negative control (**Figure 4.6A**). As expected, ssRNA demonstrated no significant stimulation of OAS1 activity and poly I:C demonstrated potent OAS1 activation. The 5'/3'-TR activates OAS1 to a similar extent as the 5'-TR RNA, achieving approximately 60% of the level achieved by poly

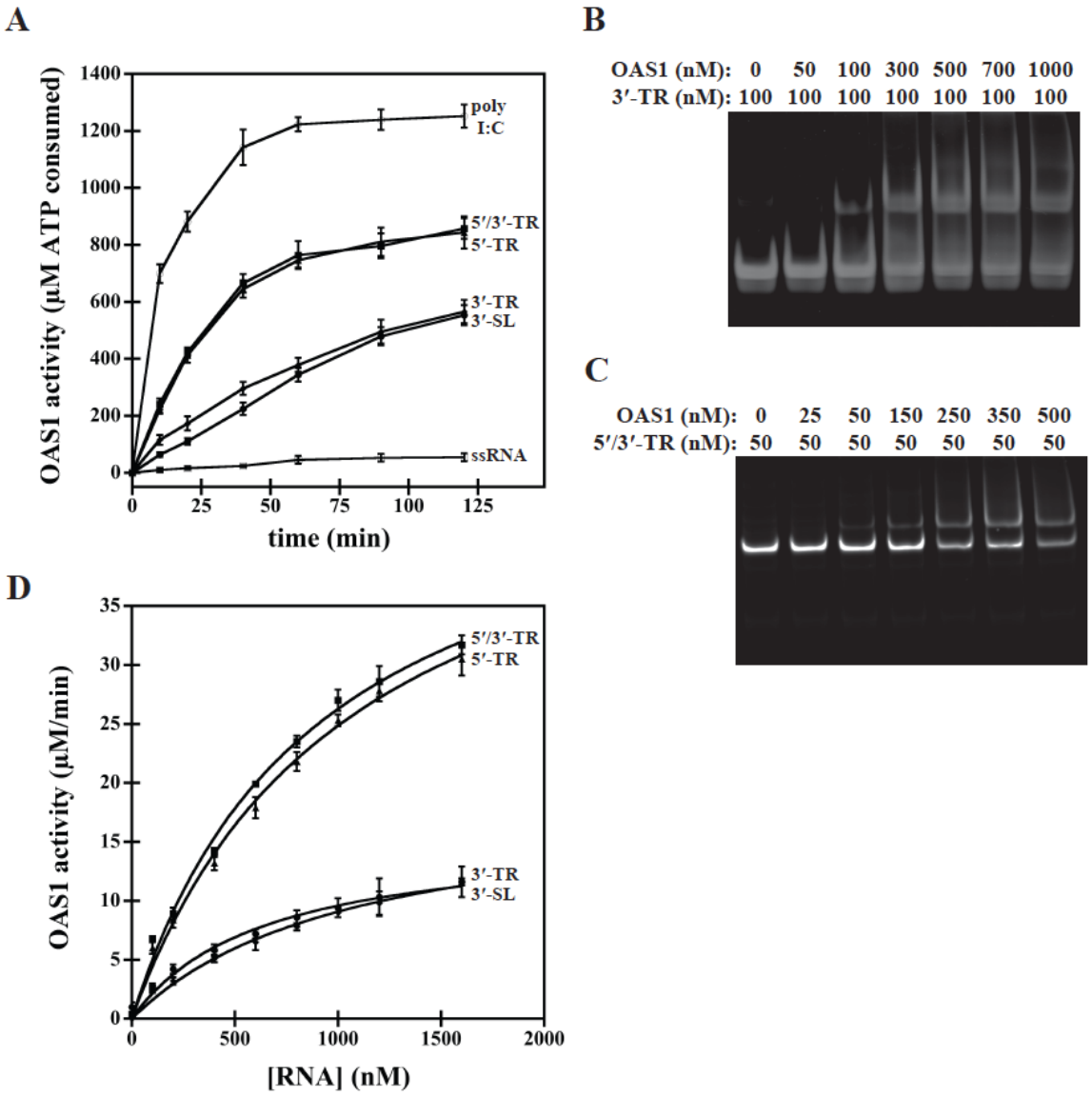

Figure 4.6 3'-TR and 5'/3'-TR binds and activated OAS1: (A) OAS1 activation assay performed with purified OAS1 (300 nM) and RNA (300 nM), incubated in the presence of ATP (2 mM) and $MgCl_2$ (5 mM) at 37°C, quenched at multiple time points (0, 20, 40, 60, 80 and 120 minutes). 2'-5'-A chain formation was quantitated by PP_i detection. Errors represent the standard deviation from at least 3 replicates, and ssRNA represents a single-stranded negative control. **(B)** EMSA of OAS1 (0 to 1000 nM) forming a higher order complex with 3'-TR (100 nM). The top band that emerges with addition of increased amount of OAS1 represents OAS1+3'-TR. **(C)** EMSA of OAS1 (0 to 500 nM) forming a higher order complex (top band) with 5'/3'-TR (50 nM). All EMSAs: 8 % native TBE gels were used and stained with Sybr Gold (Invitrogen, USA) to visualize RNA-containing species. **(D)** Enzymatic activity of OAS1 (400 nM) *vs* RNA concentration using linear regression analysis of the initial

velocity to determine OAS1 activity and the error in the analysis represented as error bars. Deo, S. *et al.* (2015) J. Structural Biol. doi:10.1016/j.jsb.2015.04.005

I:C at all time points observed (on a per mass basis). We found that the 3'-TR and 3'-SL can activate OAS1 to a level that is approximately 25% of the level achieved by poly I:C and significantly above the ssRNA control, although at earlier time points a modest difference between the two constructs can be seen. Direct quantitative comparison of RNAs to the poly I:C control should be treated with caution given the extremely large size and heterogeneity of poly I:C (~ 90 to 1400 kDa) relative to the RNAs examined. EMSAs confirm that a direct RNA-OAS1 interaction is observed, consistent with complex formation with an approximate K_D in the hundreds of nM range (**Figure 4.6B, 4.6C**).

Table 4.2 Comparison of kinetic parameters (K_{app} and V_{max}) of enzymatic activity of wild type OAS1 when activated by terminal regions of the WNV genome.
Deo, S. *et al.* (2015) J. Structural Biol. doi:10.1016/j.jsb.2015.04.005

RNA	K_{app} (nM)	V_{max} (μM/min)	R_{fit}
3′-TR	633 ± 127	16 ± 2	0.990
3′-SL	1079 ± 159	19 ± 2	0.996
5′-TR	905 ± 117	50 ± 3	0.997
5′/3′-TR	1068 ± 139	51 ± 4	0.997

To quantitatively determine kinetic parameters and binding affinities, dose-response experiments in which initial reaction velocities of OAS1-catalyzed PPi production were determined under increasing RNA concentrations for 5'/3'-TR, 5'-TR, 3'-TR and 3'-SL RNAs. Curve fitting the initial reaction velocities plotted against dsRNA concentration enabled determination of the apparent dissociation constant (K_{app}), a measure of affinity, and the maximum reaction velocity (V_{max}), a measure of catalytic potential (**Figure 4.6D**). The summary of the determined kinetic parameters for each RNA molecule, and a measure of the quality of the fit to the data (R_{fit}) is presented in **Table 4.2**. 5'/3'-TR and 5'-TR demonstrate potent stimulation of OAS1 activity with measured V_{max} values of 50±3 and 51±4 μM/min respectively. The 3'-TR and 3'-SL both activated OAS1 to a similar level (V_{max} values of 16±2 and 19±2 μM/min respectively) which represent an approximate of 30 % when compared to either 5'/3'-TR or 5'-TR. Each of the four RNAs examined exhibited reasonably similar K_{app} values between 600-1100 nM, although the modest difference between the 3'-TR (633±127 nM) and 3'-SL (1079±159 nM) was observed. Taken together, these results suggest that the 3'-SL region of the 3'-TR is sufficient for activation of OAS1. Additionally, genome cyclization alone through formation of the 5'/3'-TR is not sufficient to prevent OAS1 activation *in vitro*. In the absence of other binding partners, therefore, OAS1 can interact with each of the terminal regions in isolation or their base-paired complex with qualitatively similar affinities.

4.2.1.5 SAXS data is consistent with OAS1 binding the 3'-SL dsRNA helix in the 3′-TR.

Since the kinetic data indicated that the 3'-SL was sufficient for OAS1 activation and solution conformations of the free 3'-SL superimposed nicely on the full 3'-TR, I

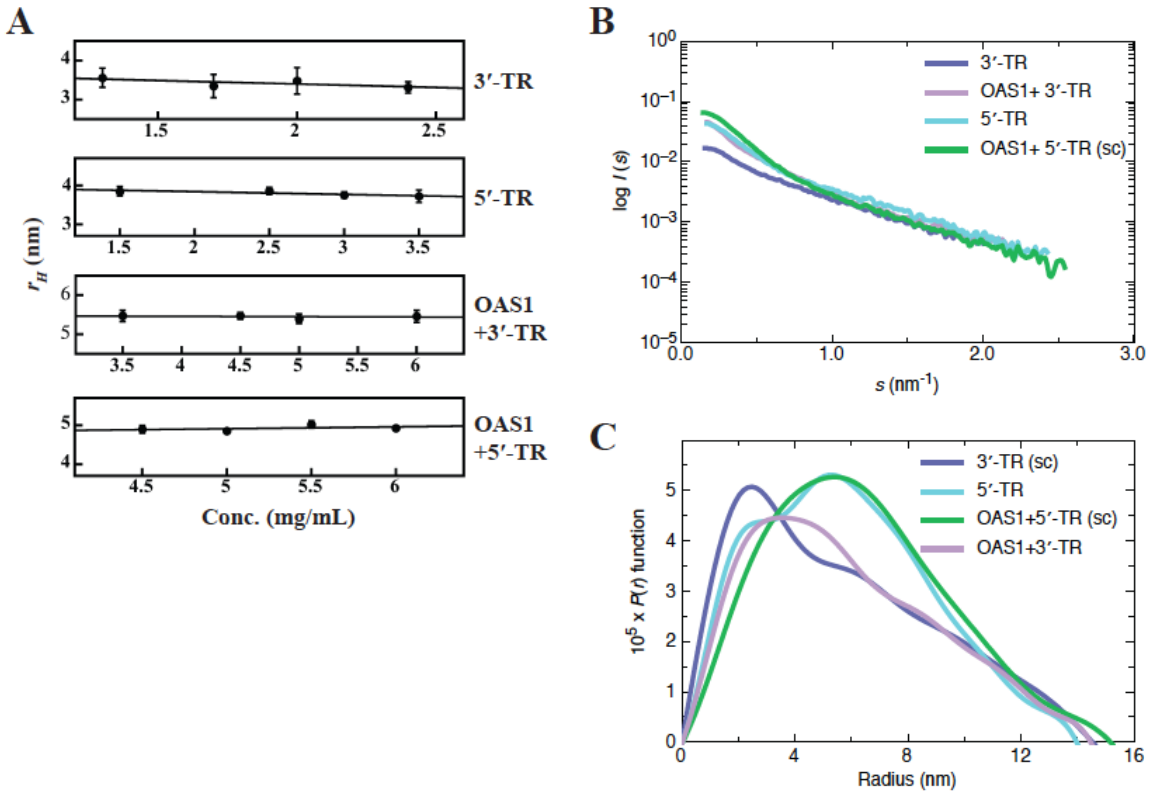

Figure 4.7 Dynamic light scattering and small angle X-ray scattering in pH 7.5 TNE buffer with Tris (50 mM), NaCl (40 mM), EDTA (1 mM). (A) DLS measurements of 3'-TR (1.2-2.4 mg/mL), 5'-TR (1.5-3.5 mg/mL), OAS1+3'-TR (3.5-6 mg/mL) and OAS1+5'-TR (4.5-6 mg/mL) at multiple concentration to check for concentration dependence. **(B)** Merged scattering data obtained at multiple concentrations of 3'-TR (1.5, 2.0 and 2.9 mg/mL), 5'-TR (2.5 and 3.5 mg/mL), OAS1+3'-TR (3.0, 4.0 and 5.0 mg/mL) and OAS1+5'-TR (3.0, 4.0 and 5.0 mg/mL). **(C)** GNOM analysis of merged SAXS data of 3'-TR, 5'-TR, OAS1+3'-TR and OAS1+5'-TR generating pair distribution functions plotted against the particle radius. Deo, S. *et al.* (2015) J. Structural Biol. doi:10.1016/j.jsb.2015.04.005

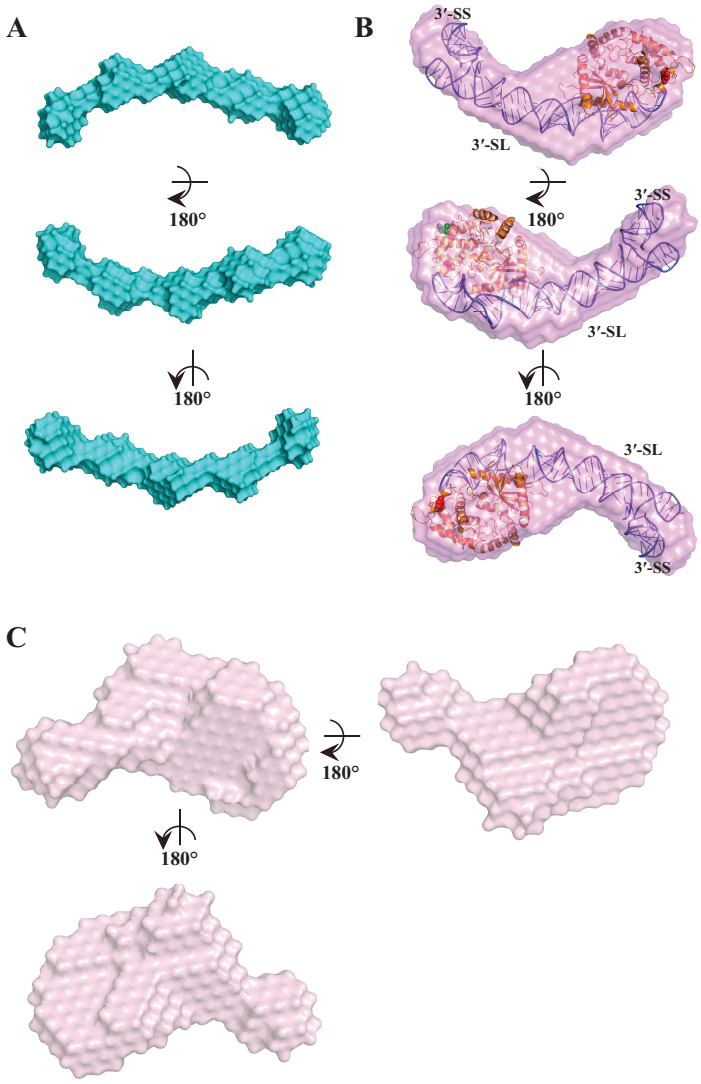

Figure 4.8 *Ab initio* modeling of 3'-TR, OAS1+3'-TR and OAS1+5'-TR in TNE buffer with Tris (50 mM), NaCl (40 mM), EDTA (1 mM): DAMMIF software was used to generate multiple *ab initio* models utilizing SAXS data as described in materials and methods. These *ab initio* models were averaged to obtain a single representative model. **A.** Averaged *ab initio* model of 3'-TR (center) rotated 180° on its X-axis (top) and Y-axis (bottom). **B.** Averaged *ab initio* model of OAS1+3'-TR (center) with the computationally determined structure superimposed on the SAXS envelope. The 3'-SL and 3'-SS have been indicated. This is rotated 180° on its X-axis (top) and Y-axis (bottom). **C.** Representative single model of OAS1+5'-TR (center) with OAS1 high-resolution structure (Donovan et al. 2013) superimposed on the SAXS envelope. This is rotated 180° on its X-axis (top) and Y-axis (bottom). Deo, S. *et al.* (2015) J. Structural Biol. doi:10.1016/j.jsb.2015.04.005

hypothesized that OAS1 interacts with the 3'-TR via the dsRNA region in the 3'-SL. To test this hypothesis, I attempted to purify both OAS1+3'-TR and OAS1+3'-SL complexes by SEC. Unfortunately, well behaved samples OAS1+3'-SL complex suited for further structural studies could not be purified. However, OAS1+3'-TR complex could be purified under buffer conditions similar to those used to detect complex by EMSA (50 mM Tris pH 7.5, 40 mM NaCl and 1mM EDTA). DLS measurements at multiple concentrations for both the free 3'-TR and OAS1+3'-TR complex detected monodisperse samples with no appreciable self-association, indicating their suitability for further analysis (**Figure 4.7A**). Merged SAXS measurements for free 3'-TR at multiple concentrations was used to determine the D_{max} and r_G values (**Figure 4.7B, 4.7C; Table 4.3**). These results are consistent with those reported for the 3'-TR in a similar buffer (**Table 4.1**), although both parameters indicate that a slightly more elongated conformation was established under conditions required for complex formation. The average filtered model from twenty 3'-TR *ab initio* models superimposed nicely (NSD=0.66±0.04) (**Figure 4.8A**), and presented a similar overall shape to the same RNA in buffer containing 50 mM Tris and 100 mM NaCl (pH 7.0) (**Figure 4.4A**).

SAXS analysis of the OAS1+3'-TR complex, as expected, resulted in a perturbation of the *P(r)* plot relative to the free RNA (**Figure 4.7A, 4.7B**). The averaged filtered model from twenty individual *ab initio* calculations was self-consistent (NSD=1.00±0.04), and presented distinct structural distortions from the free RNA (**Figure 4.8B**). Computational modeling of the complex using SAXS envelopes as a restraint localize OAS1 on the 3'-TR (**Figure 4.8B**). Model validity

was confirmed by the reasonable agreement between model and experimentally determined parameters (**Table 4.3**).

4.2.1.6 OAS1 binding does not significantly perturb the global conformation of the 5'-TR

OAS1+5'-TR complex purification was optimized for buffer conditions (50 mM Tris pH 7.5, 40 mM NaCl and 1mM EDTA), and we therefore attempted to investigate its structural features by SAXS. For comparison purposes we also investigated the 5'-TR in isolation under identical buffer conditions. Both species eluted as a single peak by SEC, and DLS measurements confirmed no self-association across a range of concentrations (**Figure 4.7A**). The *P(r)* plots obtained from the merged raw scattering data for both OAS1+5'-TR and 5'-TR show very similar broad bell-shaped curves with an elongated shoulder at larger radii (**Figure 4.7B, 4.7C**). Despite the

Table 4.3 Experimental and predicted hydrodynamic parameters in 50 mM Tris, 40 mM NaCl and 1 mM EDTA, pH 7.5

Deo, S. *et al.* (2015) J. Structural Biol. doi:10.1016/j.jsb.2015.04.005

	3′-TR		OAS1+3′-TR		5′-TR		OAS1+5′-TR	
	Exp.	DAMMI	Exp.	DAMMI	Exp.	DAMMI	Exp.	DAMMI
r_H (nm)[a]	3.43±0.11	3.96±0.08	5.45±0.0	4.57±0.04	4.01±0.0	4.56±0.06	4.92±0.0	5.47±0.05
r_G (nm)[b]	4.60±0.04	4.50±0.02	4.68±0.0	4.73±0.08	4.60±0.0	4.64±0.05	5.00±0.0	4.90±0.01
D_{max}	14.60	15.60±0.0	14.50	15.2±0.1	14.00	15.00±0.0	15.20	15.30±0.1
χ	-	0.94	-	0.82	-	1.0	-	1.0
NSD	-	0.66±0.04	-	1.00±0.04	-	1.30±0.05	-	0.88±0.04

[a] Experimentally determined from DLS data, with error obtained from linear regression analysis.
[b] Experimentally determined from *P(r)* analysis by GNOM.
[c] Model-based parameters calculated from HYDROPRO, with errors obtained as the standard deviation from 20 models.

presence of OAS1 in the complex, free and bound 5'-TR presented reasonably similar D_{max} and r_G values (**Table 4.3**), strongly suggesting that the global conformation of the 5'-TR likely remains intact upon OAS1 binding. *Ab initio* models of the free 5'-TR were generated and, as observed previously in section 3.2.1.2 and Figure 3.2 [211], two distinct conformational subpopulations were observed (data not shown). Not surprisingly therefore, a comparatively poor NSD value was obtained (1.30 ± 0.05). A better superposition of the OAS1+5'-TR *ab initio* models was observed (NSD = 0.88 ± 0.04) for the average filtered model, which unfortunately lacked sufficient structural features to determine the binding site of OAS1 with a high degree of confidence (**Figure 4.8C**). However, the high-resolution structure and a SAXS envelope for free OAS1 presented in section 3.2.1.1 (**Figure 3.1**) shared proper dimensions with a disc-shaped protrusion from the complex [211].

4.2.2 DISCUSSION

Variability in the long 3'-UTR sequence amongst *Flaviviridae* family members is usually seen in the region immediately following the stop codon whereas the terminal region, which forms two distinct stem loops, is more highly conserved [300,301,390,391]. Therefore, we used a combination of SAXS and computational modeling to determine the solution conformation of the highly conserved 3'-terminal region (3'-TR) from WNV (**Figure 1.5**). The 3'-TR RNA adopts an elongated shape, in which the two stem-loops (3'-SL and 3'-SS) interact in a kinked orientation relative to each other. Excellent superposition of individual SAXS models (NSD =

0.70 $\pm$ 0.06) reflects the remarkably constrained structure of this RNA in solution. Thermal denaturation results support this observation, as the 3'-TR has a marginally higher melting temperature than the substantially larger 5'-TR (**Figure 4.2D**). The extended conformation is consistent with previous NMR studies that did not detect any extensive tertiary interactions between the 3'-SL and 3'-SS [302]. Similar features were observed for the 3'-SL alone, indicating that the longer stem-loop likely adopts a defined dsRNA stem-loop regardless of whether the shorter stem loop is present (3'-SS). Computational modeling using SAXS data as constraints enabling visualization of the individual stem loops within the SAXS envelope. In this conformation, both elements required for interaction with the 5'-TR (3'-CS and 3'-UAR) are constrained within dsRNA segments, indicating that significant conformational changes would be required for genome circularization. We expect that the 3'-TR will adopt similar structural features amongst *Flaviviridae* members given the relatively high conservation of this region.

Studies linking SNPs in the human OAS1 gene to susceptibility to WNV infection have previously been reported [331,332], and the importance of OAS enzymes in the recognition of viral dsRNA and subsequent amplification of the initial interferon-mediated innate immune response is well established [186,387,388]. We have demonstrated the recognition of the WNV 5'-TR by and activation of human OAS1 (p42 isotype) *in vitro* (section 3.2.1.3) [211], and that the same isotype is effective at combating Dengue virus infection via an RNase L dependent pathway is noteworthy [244]. Using a combination of EMSAs and enzyme kinetics, we have quantitatively demonstrated that in addition to the 5'-TR, the 3'-

TR is capable of human OAS1 activation *in vitro* (**Figure 4.6**). OAS1 interacts with the 3'-TR with a K_{app} of 633 ± 127 nM, which is consistent with affinities for other short viral RNAs [212]. Truncation of the 3'-TR to the 3'-SL (removal of the 3'-SS: -78 to -111) only modestly reduces the affinity for OAS1 (K_{app}=1079 ±1 59 nM), suggesting that the 3'-SL is sufficient for OAS1 activation**.** The moderately reduced affinity of the 3'-SL does not affect it's activation potential as both 3'-TR and 3'-SL stimulate OAS1 activation to similar levels relative to ssRNA. SAXS experiments on the OAS1+3'-TR complex, albeit low resolution, are consistent with OAS1 recognition of the dsRNA-containing 3'-SL (**Figure 4.8**). As the 3'-SL contains approximately 30 bp, this region is more than sufficient in length given the previously reported OAS1-dsRNA structure [222]. That the dsRNA regions in the 3'-SL are significantly interrupted by bulge/non-canonical base pairs is significant, as this suggests that OAS1 can tolerate imperfectly base paired regions. Previous reports have indicated a similar binding site in the 3'-SL for eukaryotic translation elongation factor-1 alpha [302,392], highlighting the potential importance of this highly conserved region in the WNV genome to protein binding. We are currently investigating whether the three-dimensional structural features determined for the WNV 3'-TR are a conserved feature recognized by OAS enzymes in other *flaviviridae* genomes.

Complementary base pairing between two regions (5'/3'-UAR and 5'/3'-CS) in both the 5'-TR RNA and 3'-TR RNA is thought to be required for WNV genome cyclization by creating a panhandle structure [301,303,305,307]. The panhandle formation maximizes efficiency of *in vitro* RNA synthesis by the RNA-dependent

RNA polymerase [393]. We quantitatively confirmed these results by demonstrating purification of the complex formed between the two terminal regions (5'/3'-TR) with an observed K_D of 32 ± 1 nM, and that this interaction requires the 3'-CS element for proper panhandle formation (**Figure 4.1, 4.2**). SAXS experiments suggest that the panhandle adopts multiple conformations consistent with a dynamic interaction (**Figure 4.4D, 4.5**), which prevented definition of specific structural features. The *ab initio* models generated were of high quality individually (χ = 1.05), but had high variation amongst the models (NSD = 1.28 ± 0.05). A stoichiometry of 0.4:1 for 5'-TR:3'-TR is obtained from ITC (**Figure 4.2A**), and is supported qualitatively by SEC (**Figure 4.2C**). We believe these ITC and SEC data reflect the previous observation that the 5'-TR exists as a mixture of two distinct sub-populations [211], with only one potentially capable of interaction with OAS1. While the mechanism of panhandle formation is not well understood, complex formation was possible using purified RNAs at room temperature in the absence of any other factors, suggesting that the terminal regions in isolation are capable of seeding panhandle formation. These results confirm a previous study that demonstrated interaction between the 3'-TR (nt -1 to -111) and 5'-TR (nt 1-190) using a radiolabeled 3'-TR probe [301]. While protein binding factors may shift the equilibrium in a biological environment, melting curve analysis revealed no significant thermal stability advantage when comparing the 5'-TR free or base paired to the 3'-TR, indicating the potentially low thermal barrier for interconversion between the two forms (**Figure 4.2D**). Whether this observation holds for other mosquito-borne flaviviruses remains an open question, but based on

the secondary structure conservation we expect this behavior to represent a more general trend.

While the formation of the 5'/3'-TR structure brings about major structural changes (**Figure 4.3C**), *in vitro* OAS1 activation on par with a potent activator (5'-TR) was observed (**Figure 4.6**). Although, there is a possibility that the 5'/3'-TR may revert back to its components (individual 5' and 3'TR RNAs), it been observed that the complex remains considerably intact even weeks after being purified. In addition, its logical to assume that if the TR RNAs are not in the complex form (5'/3'-TR), we should expect higher activation because the reactions would contain equimolar activators of OAS1, the 5' and 3'-TR. OAS1 appears to poorly discriminate between the 5'-TR and the panhandle conformation, and is particularly interesting given that stem loops II and III from the 5'-TR (which are required for OAS1 activation [211] are fully unwound to form the 5'/3'-TR complex [301]. Kinetic experiments indicated a K_{app} of 1068 $\pm$ 139 for the OAS1 interaction with 5'/3'-TR, which is within error of the OAS1 interaction with the 5'-TR alone, and EMSAs roughly confirm the affinity of the interaction. Unfortunately, SAXS experiments failed to identify the site(s) of interaction between OAS1 and the panhandle structure, as individual models were not consistent in the shape with each other (data not shown). Taken together, the data suggest that panhandle formation between the 5'-TR and 3'-TR is not sufficient, in isolation, to protect recognition by OAS1, a potential mechanism of evasion of the innate immune response.

CHAPTER 5: SUMMARY AND FUTURE DIRECTIONS

5.1 OVERVIEW

The link between OAS1 and WNV infection has been discussed in detail in the introductory chapter (Chapter 1). Experimental procedures and methods including sample preparation have been covered in the Materials and Methods section (Chapter 2). The results obtained and the discussions correlating the finding to the current knowledge have been broadly covered (chapter 3 and 4). This chapter will present a summary of my results, and future directions of the research based on my findings.

5.2 RESEARCH SUMMARY

The OAS/RNase L pathway plays a key role in the antiviral response against both RNA and DNA viruses, which are also targeted as their transcription products and/or replicative intermediates can form dsRNAs [237,238,241,242]. Two OAS1 isoforms and OAS3 have been directly implicated in antiviral response against Dengue virus (family: *flaviviridae*, a ssRNA virus) [244]. Higher activity of OAS enzymes is demonstrated after trial vaccination against Yellow fever (member of *flaviviridae*) [245]. Chronic infection to Hepatitis C virus, another member of *flaviviridae* family also highlights a link to a SNP in OAS1 gene [246]. In horses, SNPs in both the *OAS1* gene and *RNase L* gene have been implicated in higher susceptibility to WNV [328]. Two different SNPs in the *OAS1* gene have been reported to be a host genetic risk factor in humans in the initial phase of infection

with WNV [331,332]. OAS1 has been shown to reduce WNV infection by restricting the ability of WNV to accumulate viral RNA [334]. Human OAS1 isotypes p42 and p46 also have been shown in human cell lines to block viral replication of Dengue virus, which belongs to family *Flaviviridae.* The antiviral effects of these OAS1 isotypes are accomplished in an RNase L dependent manner [244]. These results strongly suggest that in humans, the antiviral response to WNV has credible links with the host OAS1.

I sought to investigate any tenable connection between dsRNA secondary structures in the WNV genome and OAS1 activation. The 5' and 3'-TR including the untranslated regions of WNV genome are rich in stable secondary structures. The 5' and 3'-TR of WNV interact with viral and cellular protein including NS5, La protein and eEF1A, which shows them to be important and plausible targets for RNA-protein interaction [294-299]. Our investigation revealed that the 5'-TR is a binding partner and activator of OAS1 *in vitro* to a level approaching Poly I:C, the most potent activator of OAS1, an approximately 200-fold enhancement compared to ssRNA (**Figure 3.4, Table 3.2**) [211]. The minimum length based on the number of stem loops needed for high affinity binding to and activation of OAS1 comparable to the full 5'-TR is the SLI+II and SLII+III, respectively. This shows that an OAS1 activator has unknown features beyond the simple explanation of being activated by dsRNA. Studying the dsRNA structures and imperfections in SLI+II and SLII+III may give insight into how one of these long complex dsRNA structures can act as an activator while the other only binds strongly but is a poor activator. *In vitro* experiments presented in this thesis demonstrated that the 5'-TR of WNV has OAS1

recognized PAMPs. This may be true for 5'-TR of other flaviviruses as viruses of this genus show comparable and conserved secondary structures.

In addition to the 5'-TR, the 3'-TR is also capable of human OAS1 activation *in vitro* (**Figure 4.6**). OAS1 interacts with the 3'-TR and truncation of the 3'-TR to the 3'-SL (removal of the 3'-SS: -78 to -111) only modestly reduces the affinity for OAS1 suggesting that the 3'-SL is sufficient for OAS1 activation**.** The moderately reduced affinity of the 3'-SL does not affect it's activation potential as both 3'-TR and 3'-SL stimulate OAS1 activation to similar levels relative to ssCCHF. Both the 3'-TR and 3'-SL are poor activators of OAS1 compared to either Poly I:C or 5'-TR. Moderate OAS1 activation by 3'-TR comparable to Poly I:C may apply to other flaviviruses as they contain conserved secondary structures in the genomic 3' terminal region [211].

The data suggest that panhandle formation between the 5'-TR and 3'-TR is not sufficient, in isolation, to protect recognition by OAS1, a potential mechanism of evasion of the innate immune response. Purification of the complex formed between the two terminal regions (5'/3'-TR) was achieved with an observed K_D of 32 ± 1 nM, and this interaction requires the 3'-CS element for proper panhandle formation (**Figure 4.2A, 4.2B**) [394]. Complex formation between 5'-TR and 3'-TR was possible using purified RNAs at room temperature in the absence of any other factors. Melting curve analysis revealed no significant thermal stability advantage when comparing the 5'-TR free or base paired to the 3'-TR, indicating the potentially low thermal barrier for interconversion between the two forms. The spontaneity of this panhandle formation may be a key to rapid increase in viral titer by providing a template required for production of genomes for viral progenies [394]. SAXS

experiments suggest that the panhandle adopts multiple conformations consistent with a dynamic interaction (**Figure 4.4D**)**.** A stoichiometry of 0.4:1 for 5'-TR:3'-TR is obtained from ITC (**Figure 4.2A**), and is supported qualitatively by SEC (**Figure 4.2C**). We believe these ITC and SEC data reflect the previous observation that the 5'-TR exists as a mixture of two distinct sub-populations [211]. While the formation of the 5'/3'-TR structure brings about major structural changes (**Figure 4.3C**), *in vitro* OAS1 activation on par with a potent activator (5'-TR) [211] was observed (**Figure 4.6D**). This suggests that the panhandle structure doesn't escape OAS1 recognition and hence provide no advantage in sequestering recognition by host innate immunity. Whether this panhandle structure in other flaviviruses demonstrates similar OAS1 activation potential comparable to WNV remains to be studied but based on the secondary structure similarity in these terminal region RNAs and panhandle formation across members of this family it's plausible that they activate OAS1.

Although SAXS represents a low-resolution approach, the results presented are the first direct structural observation of the 5'-TR from the WNV genome. The determined SAXS models of the 5'-TR RNA suggest an inherently flexible molecule in solution that appears to adopt two conformations (**Figure 3.2B, 3.2C, 3.2D**). One subset of these conformations presented three distinct protrusions (that likely correspond to SLI, SLII, and SLIII respectively), whereas the remaining models lack domain resolution probably owing to dynamic equilibrium between these conformations [211]. Given that genome cyclization with complimentary regions in the 3'-TR would require unwinding of both SLII and SLIII in the 5'-TR, it is enticing

to speculate that our observed conformations represent the "structured" and "partially unwound" 5'-TR conformations.

We used a combination of SAXS and computational modeling to determine the solution conformation of the highly conserved amongst flaviviral 3'-terminal region (3'-TR) from WNV (**Figure 4.4**) [394]. The 3'-TR RNA adopts an elongated shape, in which the two stem-loops (3'-SL and 3'-SS) interact in a kinked orientation relative to each other. Thermal denaturation results support this observation, as the 3'-TR has a marginally higher melting temperature than the substantially larger 5'-TR (**Figure 4.2D**). Similar features were observed for the 3'-SL alone, indicating that the longer stem-loop likely adopts a defined dsRNA stem-loop regardless of whether the shorter stem loop is present (3'-SS) [394]. SAXS data used as constraints enabled computational modeling resulting in clear visualization of individual stem loops connected by a short single-stranded linker within the SAXS envelope. Solution conformation of OAS1+3'-TR complex generated from SAXS data are consistent with OAS1 recognition of the dsRNA-containing 3'-SL (**Figure 4.7**) [394].

We studied two point mutations in OAS1 at R195 and K199 within the RNA binding domain on the basic tract opposite the active site [217,222]. These mutations did not impact the overall structure of OAS1 as determined by SAXS experiments (**Figure 3.5A**) [211]. As expected, these mutants show no detectable affinity for WNV 5'-TR, nor do they activate the catalytic activity of OAS1 (**Table 3.3**).

5.3 FUTURE DIRECTIONS

In this thesis I present detailed biochemical and low-resolution structural aspects of the terminal region RNAs of WNV and their interaction with OAS1. The findings presented contribute to our understanding of viral PAMPs and their recognition by cellular PRRs. OAS1, a PRR of viral dsRNA PAMPs has demonstrated *in vitro* the ability to recognize imperfect dsRNAs that may contain loops and bulges. Available secondary structural information on these TR RNAs of WNV genome suggests imperfections including loops and non-canonical base pairing [301,302]. This would make perfect sense, as the PRRs should have the ability to recognize a wider range of PAMPs so as to be able to initiate an optimal antiviral innate immune response. Along with the results I have obtained, the study undertaken has certainly evoked interesting questions that could be the focus of future studies. Research in following directions are suggested:

(I) As the structural features of the WNV 5'-TR RNA appears to be conserved amongst other *Flaviviridae* family members at the secondary structural level [296,298,299], the stem-loop recognition at the 5'-TR observed in this study by OAS1 may possibly represent a general feature of OAS enzymes. The 3'-TR (nt -1 to -111) at the distal end of the long 3'-untranslated region of WNV contains a long (3'-SL, nt -1 to – 79) and a short (3'-SS, nt -80 to -95) stem loop (**Figure 1.5B**). The 3'-TRs of *flaviviridae* members appears to be conserved [296,300-302]. It will be interesting to investigate whether the important features determined from SAXS and *in silico* modeling, for the TRs of WNV are a conserved feature recognized by

OAS enzymes in other Flaviviral genomes including important pathogenic ones (DENV, YFV and JEV).

(II) WNV TR RNAs are also recognized by an important dsRNA pattern recognition receptor, RIG-I, enabling induction of the antiviral response [258]. The *in vitro* studies presented in this thesis have shown that these terminal region RNAs can activate OAS1. It will be interesting to study how these terminal regions of the WNV genome interact with other dsRNA recognizing PRRs. We are currently investigating the interaction of TR RNAs of WNV genome with PKR, an important PRR recognizing viral dsRNA PAMPs.

(III) Melting curve analysis revealed no significant thermal stability advantage when comparing the 5'-TR free or base paired to the 3'-TR, indicating the potentially low thermal barrier for interconversion between the two forms. Whether this observation holds for other mosquito-borne flaviviruses remains an open question. Based on the secondary structure conservation among flaviviruses, we expect this behavior to be replicated by other members of this family of viruses, but this will be another aspect to be further investigated.

(IV) Considering 5'-TR and 3'-TR complex formation to mimic genome circularization, both elements required for interaction with the 5'-TR (3'-CS and 3'-UAR) are constrained within dsRNA segments in its free form, indicating that significant conformational changes would be required for genome circularization.

Our data suggest that panhandle formation between the 5'-TR and 3'-TR is not sufficient, in isolation, to protect recognition by OAS1, a potential mechanism of evasion of the innate immune response. Further studies on the OAS1 activation potential of the 5'-TR and 3'-TR complex of other *flaviviridae* family members *in vitro* is required. Focusing on *in vivo* studies to complement and validate these *in vitro* activation results are necessary.

(V) OAS1 is suggested to function as a tetramer to polymerize 2'-5'-A chains [204,205]. Results presented previously [212] and in this thesis are not consistent with this hypothesis, including examining OAS1 by SAXS and DLS over a range of concentrations. Use of SEC to purify the TR RNA+OAS1 complex lacked any peak that could represent a tetramer of OAS1. However, we haven't examined OAS1 self-association by changing the conditions including the presence/absence of $MgCl_2$, ATP, non-hydrolyzable ATP analogues and dsRNA. Therefore, repeating the experiments using AUC, size exclusion chromatography fitted with multi-angle light scattering device (SEC-MALS), DLS and SAXS may be needed to obtain further information on the OAS1 tetramerization hypothesis.

(VI) In this thesis I have focused on OAS1 and its interaction with the TR RNAs of WNV. Similar studies could be undertaken to investigate how these TR RNAs interact with other members of the OAS family of proteins, namely OAS2 and OAS3 isoforms. A combination of *in vivo* and *in vitro* approaches will be useful in establishing the interaction, if any, of the TR RNAs of WNV with OAS2 and OAS3.

Post-transcriptional modifications are thought to be important for these two proteins [184,185,224], which means to obtain functional proteins we need to express these proteins preferably in mammalian cells. I succeeded in overexpressing OAS1 in HEK 293T cells and perform experiments to study its interaction with 5'-TR (**Figure 3.6 A and 3.6B**). The level of overexpressed OAS1 in HEK 293T cells was much higher than the basal level OAS1 present in these cells (data not shown). A similar approach could be undertaken to not only over express OAS2 and OAS3 but also investigate their interaction with the TR RNAs of the WNV genome.

(VII) Obtaining high-resolution structure of the terminal region RNAs of the WNV genome and its complex with OAS1 is crucial in understanding the three dimensional structure at the molecular level. Although the high-resolution structure of OAS1 with a synthetic, perfectly dsRNA is available, how viral RNA ligand with imperfect dsRNA structure interacts with OAS1 is still not clear. This provides valid reasons to attempt crystalizing OAS1+TR RNA (of WNV genome) complex.

REFERENCES

1. Kindt TJO, B. A.; Goldsby, R. A. (2006) Kuby Immunology, Sixth Edition. 8.
2. Wardemann H, Nussenzweig MC (2007) B-cell self-tolerance in humans. Adv Immunol 95: 83-110.
3. Ausubel FM (2005) Are innate immune signaling pathways in plants and animals conserved? Nat Immunol 6: 973-979.
4. Goodbourn S, Didcock L, Randall RE (2000) Interferons: cell signalling, immune modulation, antiviral response and virus countermeasures. J Gen Virol 81: 2341-2364.
5. Akira S, Uematsu S, Takeuchi O (2006) Pathogen recognition and innate immunity. Cell 124: 783-801.
6. Janeway CAJW, M. et al. (2001) The Immune System in Health and Diseases. New York: Garland Science.
7. Schoggins JW, Rice CM (2011) Interferon-stimulated genes and their antiviral effector functions. Curr Opin Virol 1: 519-525.
8. Parkin J, Cohen B (2001) An overview of the immune system. Lancet 357: 1777-1789.
9. Platanias LC (2005) Mechanisms of type-I- and type-II-interferon-mediated signalling. Nat Rev Immunol 5: 375-386.
10. Grandvaux N, Servant MJ, tenOever B, Sen GC, Balachandran S, et al. (2002) Transcriptional profiling of interferon regulatory factor 3 target genes: direct involvement in the regulation of interferon-stimulated genes. J Virol 76: 5532-5539.
11. Kawai T, Akira S (2006) Innate immune recognition of viral infection. Nat Immunol 7: 131-137.
12. Langevin C, Aleksejeva E, Passoni G, Palha N, Levraud JP, et al. (2013) The antiviral innate immune response in fish: evolution and conservation of the IFN system. J Mol Biol 425: 4904-4920.
13. Pietretti D, Wiegertjes GF (2014) Ligand specificities of Toll-like receptors in fish: indications from infection studies. Dev Comp Immunol 43: 205-222.
14. Green TJ, Montagnani C (2013) Poly I:C induces a protective antiviral immune response in the Pacific oyster (Crassostrea gigas) against subsequent challenge with Ostreid herpesvirus (OsHV-1 muvar). Fish Shellfish Immunol 35: 382-388.
15. Robalino J, Browdy CL, Prior S, Metz A, Parnell P, et al. (2004) Induction of antiviral immunity by double-stranded RNA in a marine invertebrate. J Virol 78: 10442-10448.
16. Wang PH, Weng SP, He JG (2014) Nucleic acid-induced antiviral immunity in invertebrates: An evolutionary perspective. Dev Comp Immunol.
17. Lewis SH, Obbard DJ (2014) Recent insights into the evolution of innate viral sensing in animals. Curr Opin Microbiol 20: 170-175.
18. Takeuchi O, Akira S (2008) RIG-I-like antiviral protein in flies. Nat Immunol 9: 1327-1328.

19. Kingsolver MB, Huang Z, Hardy RW (2013) Insect antiviral innate immunity: pathways, effectors, and connections. J Mol Biol 425: 4921-4936.
20. Qin H, Wilson CA, Lee SJ, Zhao X, Benveniste EN (2005) LPS induces CD40 gene expression through the activation of NF-kappaB and STAT-1alpha in macrophages and microglia. Blood 106: 3114-3122.
21. Fitzgerald DC, Meade KG, McEvoy AN, Lillis L, Murphy EP, et al. (2007) Tumour necrosis factor-alpha (TNF-alpha) increases nuclear factor kappaB (NFkappaB) activity in and interleukin-8 (IL-8) release from bovine mammary epithelial cells. Vet Immunol Immunopathol 116: 59-68.
22. Lin R, Genin P, Mamane Y, Hiscott J (2000) Selective DNA binding and association with the CREB binding protein coactivator contribute to differential activation of alpha/beta interferon genes by interferon regulatory factors 3 and 7. Mol Cell Biol 20: 6342-6353.
23. Marie I, Durbin JE, Levy DE (1998) Differential viral induction of distinct interferon-alpha genes by positive feedback through interferon regulatory factor-7. EMBO J 17: 6660-6669.
24. Sato M, Suemori H, Hata N, Asagiri M, Ogasawara K, et al. (2000) Distinct and essential roles of transcription factors IRF-3 and IRF-7 in response to viruses for IFN-alpha/beta gene induction. Immunity 13: 539-548.
25. Ye J, Ortaldo JR, Conlon K, Winkler-Pickett R, Young HA (1995) Cellular and molecular mechanisms of IFN-gamma production induced by IL-2 and IL-12 in a human NK cell line. J Leukoc Biol 58: 225-233.
26. Barnes B, Lubyova B, Pitha PM (2002) On the role of IRF in host defense. J Interferon Cytokine Res 22: 59-71.
27. Kim TK, Maniatis T (1997) The mechanism of transcriptional synergy of an in vitro assembled interferon-beta enhanceosome. Mol Cell 1: 119-129.
28. Lin R, Heylbroeck C, Genin P, Pitha PM, Hiscott J (1999) Essential role of interferon regulatory factor 3 in direct activation of RANTES chemokine transcription. Mol Cell Biol 19: 959-966.
29. Wathelet MG, Lin CH, Parekh BS, Ronco LV, Howley PM, et al. (1998) Virus infection induces the assembly of coordinately activated transcription factors on the IFN-beta enhancer in vivo. Mol Cell 1: 507-518.
30. Sato M, Tanaka N, Hata N, Oda E, Taniguchi T (1998) Involvement of the IRF family transcription factor IRF-3 in virus-induced activation of the IFN-beta gene. FEBS Lett 425: 112-116.
31. Hiscott J (2007) Convergence of the NF-kappaB and IRF pathways in the regulation of the innate antiviral response. Cytokine Growth Factor Rev 18: 483-490.
32. Sun Z, Andersson R (2002) NF-kappaB activation and inhibition: a review. Shock 18: 99-106.
33. Sadler AJ, Williams BR (2008) Interferon-inducible antiviral effectors. Nat Rev Immunol 8: 559-568.
34. Darnell JE, Jr., Kerr IM, Stark GR (1994) Jak-STAT pathways and transcriptional activation in response to IFNs and other extracellular signaling proteins. Science 264: 1415-1421.

35. Shuai K, Liu B (2003) Regulation of JAK-STAT signalling in the immune system. Nat Rev Immunol 3: 900-911.
36. Darnell JE, Jr. (1997) STATs and gene regulation. Science 277: 1630-1635.
37. Levy DE, Darnell JE, Jr. (2002) Stats: transcriptional control and biological impact. Nat Rev Mol Cell Biol 3: 651-662.
38. Leonard WJ, O'Shea JJ (1998) Jaks and STATs: biological implications. Annu Rev Immunol 16: 293-322.
39. Stetson DB, Medzhitov R (2006) Type I interferons in host defense. Immunity 25: 373-381.
40. Leaman DW, Chawla-Sarkar M, Jacobs B, Vyas K, Sun Y, et al. (2003) Novel growth and death related interferon-stimulated genes (ISGs) in melanoma: greater potency of IFN-beta compared with IFN-alpha2. J Interferon Cytokine Res 23: 745-756.
41. Der SD, Zhou A, Williams BR, Silverman RH (1998) Identification of genes differentially regulated by interferon alpha, beta, or gamma using oligonucleotide arrays. Proc Natl Acad Sci U S A 95: 15623-15628.
42. Samuel CE (2001) Antiviral actions of interferons. Clinical Microbiology Reviews 14: 778-809.
43. Basagoudanavar SH, Thapa RJ, Nogusa S, Wang J, Beg AA, et al. (2011) Distinct roles for the NF-kappa B RelA subunit during antiviral innate immune responses. J Virol 85: 2599-2610.
44. Peters KL, Smith HL, Stark GR, Sen GC (2002) IRF-3-dependent, NFkappa B- and JNK-independent activation of the 561 and IFN-beta genes in response to double-stranded RNA. Proc Natl Acad Sci U S A 99: 6322-6327.
45. Nakaya T, Sato M, Hata N, Asagiri M, Suemori H, et al. (2001) Gene induction pathways mediated by distinct IRFs during viral infection. Biochem Biophys Res Commun 283: 1150-1156.
46. Hata N, Sato M, Takaoka A, Asagiri M, Tanaka N, et al. (2001) Constitutive IFN-alpha/beta signal for efficient IFN-alpha/beta gene induction by virus. Biochem Biophys Res Commun 285: 518-525.
47. Schmitz F, Heit A, Guggemoos S, Krug A, Mages J, et al. (2007) Interferon-regulatory-factor 1 controls Toll-like receptor 9-mediated IFN-beta production in myeloid dendritic cells. Eur J Immunol 37: 315-327.
48. Negishi H, Fujita Y, Yanai H, Sakaguchi S, Ouyang X, et al. (2006) Evidence for licensing of IFN-gamma-induced IFN regulatory factor 1 transcription factor by MyD88 in Toll-like receptor-dependent gene induction program. Proc Natl Acad Sci U S A 103: 15136-15141.
49. Zhang SY, Boisson-Dupuis S, Chapgier A, Yang K, Bustamante J, et al. (2008) Inborn errors of interferon (IFN)-mediated immunity in humans: insights into the respective roles of IFN-alpha/beta, IFN-gamma, and IFN-lambda in host defense. Immunological Reviews 226: 29-40.
50. Dupuis S, Dargemont C, Fieschi C, Thomassin N, Rosenzweig S, et al. (2001) Impairment of mycobacterial but not viral immunity by a germline human STAT1 mutation. Science 293: 300-303.

51. Chapgier A, Boisson-Dupuis S, Jouanguy E, Vogt G, Feinberg J, et al. (2006) Novel STAT1 alleles in otherwise healthy patients with mycobacterial disease. PLoS Genet 2: e131.
52. Altare F, Lammas D, Revy P, Jouanguy E, Doffinger R, et al. (1998) Inherited interleukin 12 deficiency in a child with bacille Calmette-Guerin and Salmonella enteritidis disseminated infection. J Clin Invest 102: 2035-2040.
53. Picard C, Fieschi C, Altare F, Al-Jumaah S, Al-Hajjar S, et al. (2002) Inherited interleukin-12 deficiency: IL12B genotype and clinical phenotype of 13 patients from six kindreds. Am J Hum Genet 70: 336-348.
54. Altare F, Durandy A, Lammas D, Emile JF, Lamhamedi S, et al. (1998) Impairment of mycobacterial immunity in human interleukin-12 receptor deficiency. Science 280: 1432-1435.
55. de Jong R, Altare F, Haagen IA, Elferink DG, Boer T, et al. (1998) Severe mycobacterial and Salmonella infections in interleukin-12 receptor-deficient patients. Science 280: 1435-1438.
56. Jouanguy E, Lamhamedi-Cherradi S, Altare F, Fondaneche MC, Tuerlinckx D, et al. (1997) Partial interferon-gamma receptor 1 deficiency in a child with tuberculoid bacillus Calmette-Guerin infection and a sibling with clinical tuberculosis. J Clin Invest 100: 2658-2664.
57. Dorman SE, Picard C, Lammas D, Heyne K, van Dissel JT, et al. (2004) Clinical features of dominant and recessive interferon gamma receptor 1 deficiencies. Lancet 364: 2113-2121.
58. Dorman SE, Holland SM (1998) Mutation in the signal-transducing chain of the interferon-gamma receptor and susceptibility to mycobacterial infection. J Clin Invest 101: 2364-2369.
59. Vogt G, Bustamante J, Chapgier A, Feinberg J, Boisson Dupuis S, et al. (2008) Complementation of a pathogenic IFNGR2 misfolding mutation with modifiers of N-glycosylation. J Exp Med 205: 1729-1737.
60. Malathi K, Dong B, Gale M, Jr., Silverman RH (2007) Small self-RNA generated by RNase L amplifies antiviral innate immunity. Nature 448: 816-819.
61. Ransohoff RM, Brown MA (2012) Innate immunity in the central nervous system. J Clin Invest 122: 1164-1171.
62. Takeda K, Akira S (2005) Toll-like receptors in innate immunity. Int Immunol 17: 1-14.
63. Barbalat R, Ewald SE, Mouchess ML, Barton GM (2011) Nucleic acid recognition by the innate immune system. Annu Rev Immunol 29: 185-214.
64. Lemaitre B, Nicolas E, Michaut L, Reichhart JM, Hoffmann JA (1996) The dorsoventral regulatory gene cassette spatzle/Toll/cactus controls the potent antifungal response in Drosophila adults. Cell 86: 973-983.
65. Takeda K, Kaisho T, Akira S (2003) Toll-like receptors. Annu Rev Immunol 21: 335-376.
66. Kawai T, Akira S (2011) Toll-like receptors and their crosstalk with other innate receptors in infection and immunity. Immunity 34: 637-650.
67. Akira S, Takeda K (2004) Toll-like receptor signalling. Nat Rev Immunol 4: 499-511.

68. Bowie A, O'Neill LA (2000) The interleukin-1 receptor/Toll-like receptor superfamily: signal generators for pro-inflammatory interleukins and microbial products. J Leukoc Biol 67: 508-514.
69. Boehme KW, Guerrero M, Compton T (2006) Human cytomegalovirus envelope glycoproteins B and H are necessary for TLR2 activation in permissive cells. J Immunol 177: 7094-7102.
70. Compton T, Kurt-Jones EA, Boehme KW, Belko J, Latz E, et al. (2003) Human cytomegalovirus activates inflammatory cytokine responses via CD14 and Toll-like receptor 2. J Virol 77: 4588-4596.
71. Georgel P, Jiang Z, Kunz S, Janssen E, Mols J, et al. (2007) Vesicular stomatitis virus glycoprotein G activates a specific antiviral Toll-like receptor 4-dependent pathway. Virology 362: 304-313.
72. Hutchens MA, Luker KE, Sonstein J, Nunez G, Curtis JL, et al. (2008) Protective effect of Toll-like receptor 4 in pulmonary vaccinia infection. PLoS Pathog 4: e1000153.
73. Lund J, Sato A, Akira S, Medzhitov R, Iwasaki A (2003) Toll-like receptor 9-mediated recognition of Herpes simplex virus-2 by plasmacytoid dendritic cells. J Exp Med 198: 513-520.
74. Hemmi H, Takeuchi O, Kawai T, Kaisho T, Sato S, et al. (2000) A Toll-like receptor recognizes bacterial DNA. Nature 408: 740-745.
75. Alexopoulou L, Holt AC, Medzhitov R, Flavell RA (2001) Recognition of double-stranded RNA and activation of NF-kappaB by Toll-like receptor 3. Nature 413: 732-738.
76. Diebold SS, Kaisho T, Hemmi H, Akira S, Reis e Sousa C (2004) Innate antiviral responses by means of TLR7-mediated recognition of single-stranded RNA. Science 303: 1529-1531.
77. Heil F, Hemmi H, Hochrein H, Ampenberger F, Kirschning C, et al. (2004) Species-specific recognition of single-stranded RNA via toll-like receptor 7 and 8. Science 303: 1526-1529.
78. Akira S (2006) TLR signaling. Curr Top Microbiol Immunol 311: 1-16.
79. Kawai T, Akira S (2010) The role of pattern-recognition receptors in innate immunity: update on Toll-like receptors. Nat Immunol 11: 373-384.
80. Yamamoto M, Sato S, Mori K, Hoshino K, Takeuchi O, et al. (2002) Cutting edge: a novel Toll/IL-1 receptor domain-containing adapter that preferentially activates the IFN-beta promoter in the Toll-like receptor signaling. J Immunol 169: 6668-6672.
81. Kawai T, Sato S, Ishii KJ, Coban C, Hemmi H, et al. (2004) Interferon-alpha induction through Toll-like receptors involves a direct interaction of IRF7 with MyD88 and TRAF6. Nat Immunol 5: 1061-1068.
82. Hemmi H, Kaisho T, Takeuchi O, Sato S, Sanjo H, et al. (2002) Small anti-viral compounds activate immune cells via the TLR7 MyD88-dependent signaling pathway. Nat Immunol 3: 196-200.
83. Oliveira-Nascimento L, Massari P, Wetzler LM (2012) The Role of TLR2 in Infection and Immunity. Front Immunol 3: 79.
84. Lester SN, Li K (2014) Toll-like receptors in antiviral innate immunity. J Mol Biol 426: 1246-1264.

85. Hoebe K, Du X, Georgel P, Janssen E, Tabeta K, et al. (2003) Identification of Lps2 as a key transducer of MyD88-independent TIR signalling. Nature 424: 743-748.
86. Tabeta K, Georgel P, Janssen E, Du X, Hoebe K, et al. (2004) Toll-like receptors 9 and 3 as essential components of innate immune defense against mouse cytomegalovirus infection. Proc Natl Acad Sci U S A 101: 3516-3521.
87. Reinert LS, Harder L, Holm CK, Iversen MB, Horan KA, et al. (2012) TLR3 deficiency renders astrocytes permissive to herpes simplex virus infection and facilitates establishment of CNS infection in mice. J Clin Invest 122: 1368-1376.
88. Hardarson HS, Baker JS, Yang Z, Purevjav E, Huang CH, et al. (2007) Toll-like receptor 3 is an essential component of the innate stress response in virus-induced cardiac injury. Am J Physiol Heart Circ Physiol 292: H251-258.
89. Wang N, Liang Y, Devaraj S, Wang J, Lemon SM, et al. (2009) Toll-like receptor 3 mediates establishment of an antiviral state against hepatitis C virus in hepatoma cells. J Virol 83: 9824-9834.
90. Tsai YT, Chang SY, Lee CN, Kao CL (2009) Human TLR3 recognizes dengue virus and modulates viral replication in vitro. Cell Microbiol 11: 604-615.
91. Diebold SS (2008) Recognition of viral single-stranded RNA by Toll-like receptors. Adv Drug Deliv Rev 60: 813-823.
92. Beignon AS, McKenna K, Skoberne M, Manches O, DaSilva I, et al. (2005) Endocytosis of HIV-1 activates plasmacytoid dendritic cells via Toll-like receptor-viral RNA interactions. J Clin Invest 115: 3265-3275.
93. Wang JP, Liu P, Latz E, Golenbock DT, Finberg RW, et al. (2006) Flavivirus activation of plasmacytoid dendritic cells delineates key elements of TLR7 signaling beyond endosomal recognition. J Immunol 177: 7114-7121.
94. Town T, Bai F, Wang T, Kaplan AT, Qian F, et al. (2009) Toll-like receptor 7 mitigates lethal West Nile encephalitis via interleukin 23-dependent immune cell infiltration and homing. Immunity 30: 242-253.
95. Takahashi K, Asabe S, Wieland S, Garaigorta U, Gastaminza P, et al. (2010) Plasmacytoid dendritic cells sense hepatitis C virus-infected cells, produce interferon, and inhibit infection. Proc Natl Acad Sci U S A 107: 7431-7436.
96. Krug A, Luker GD, Barchet W, Leib DA, Akira S, et al. (2004) Herpes simplex virus type 1 activates murine natural interferon-producing cells through toll-like receptor 9. Blood 103: 1433-1437.
97. Samuelsson C, Hausmann J, Lauterbach H, Schmidt M, Akira S, et al. (2008) Survival of lethal poxvirus infection in mice depends on TLR9, and therapeutic vaccination provides protection. J Clin Invest 118: 1776-1784.
98. Sutherland DB, Ranasinghe C, Regner M, Phipps S, Matthaei KI, et al. (2011) Evaluating vaccinia virus cytokine co-expression in TLR GKO mice. Immunol Cell Biol 89: 706-715.
99. Murawski MR, Bowen GN, Cerny AM, Anderson LJ, Haynes LM, et al. (2009) Respiratory syncytial virus activates innate immunity through Toll-like receptor 2. J Virol 83: 1492-1500.

100. Yoneyama M, Kikuchi M, Matsumoto K, Imaizumi T, Miyagishi M, et al. (2005) Shared and unique functions of the DExD/H-box helicases RIG-I, MDA5, and LGP2 in antiviral innate immunity. J Immunol 175: 2851-2858.
101. Sun Z, Ren H, Liu Y, Teeling JL, Gu J (2011) Phosphorylation of RIG-I by casein kinase II inhibits its antiviral response. J Virol 85: 1036-1047.
102. Hiscott J, Lin R, Nakhaei P, Paz S (2006) MasterCARD: a priceless link to innate immunity. Trends Mol Med 12: 53-56.
103. Yoneyama M, Kikuchi M, Natsukawa T, Shinobu N, Imaizumi T, et al. (2004) The RNA helicase RIG-I has an essential function in double-stranded RNA-induced innate antiviral responses. Nat Immunol 5: 730-737.
104. Cui S, Eisenacher K, Kirchhofer A, Brzozka K, Lammens A, et al. (2008) The C-terminal regulatory domain is the RNA 5'-triphosphate sensor of RIG-I. Mol Cell 29: 169-179.
105. Takahasi K, Yoneyama M, Nishihori T, Hirai R, Kumeta H, et al. (2008) Nonself RNA-sensing mechanism of RIG-I helicase and activation of antiviral immune responses. Mol Cell 29: 428-440.
106. Meylan E, Curran J, Hofmann K, Moradpour D, Binder M, et al. (2005) Cardif is an adaptor protein in the RIG-I antiviral pathway and is targeted by hepatitis C virus. Nature 437: 1167-1172.
107. Liu S, Cai X, Wu J, Cong Q, Chen X, et al. (2015) Phosphorylation of innate immune adaptor proteins MAVS, STING, and TRIF induces IRF3 activation. Science 347: aaa2630.
108. Kato H, Takeuchi O, Sato S, Yoneyama M, Yamamoto M, et al. (2006) Differential roles of MDA5 and RIG-I helicases in the recognition of RNA viruses. Nature 441: 101-105.
109. Loo YM, Fornek J, Crochet N, Bajwa G, Perwitasari O, et al. (2008) Distinct RIG-I and MDA5 signaling by RNA viruses in innate immunity. J Virol 82: 335-345.
110. Ablasser A, Bauernfeind F, Hartmann G, Latz E, Fitzgerald KA, et al. (2009) RIG-I-dependent sensing of poly(dA:dT) through the induction of an RNA polymerase III-transcribed RNA intermediate. Nat Immunol 10: 1065-1072.
111. Chiu YH, Macmillan JB, Chen ZJ (2009) RNA polymerase III detects cytosolic DNA and induces type I interferons through the RIG-I pathway. Cell 138: 576-591.
112. McCartney SA, Thackray LB, Gitlin L, Gilfillan S, Virgin HW, et al. (2008) MDA-5 recognition of a murine norovirus. PLoS Pathog 4: e1000108.
113. Roth-Cross JK, Bender SJ, Weiss SR (2008) Murine coronavirus mouse hepatitis virus is recognized by MDA5 and induces type I interferon in brain macrophages/microglia. J Virol 82: 9829-9838.
114. Satoh T, Kato H, Kumagai Y, Yoneyama M, Sato S, et al. (2010) LGP2 is a positive regulator of RIG-I- and MDA5-mediated antiviral responses. Proc Natl Acad Sci U S A 107: 1512-1517.
115. Venkataraman T, Valdes M, Elsby R, Kakuta S, Caceres G, et al. (2007) Loss of DExD/H box RNA helicase LGP2 manifests disparate antiviral responses. J Immunol 178: 6444-6455.
116. Takahasi K, Kumeta H, Tsuduki N, Narita R, Shigemoto T, et al. (2009) Solution structures of cytosolic RNA sensor MDA5 and LGP2 C-terminal domains:

identification of the RNA recognition loop in RIG-I-like receptors. J Biol Chem 284: 17465-17474.
117. Geddes K, Magalhaes JG, Girardin SE (2009) Unleashing the therapeutic potential of NOD-like receptors. Nat Rev Drug Discov 8: 465-479.
118. Franchi L, Park JH, Shaw MH, Marina-Garcia N, Chen G, et al. (2008) Intracellular NOD-like receptors in innate immunity, infection and disease. Cell Microbiol 10: 1-8.
119. Werts C, Girardin SE, Philpott DJ (2006) TIR, CARD and PYRIN: three domains for an antimicrobial triad. Cell Death Differ 13: 798-815.
120. Petrilli V, Dostert C, Muruve DA, Tschopp J (2007) The inflammasome: a danger sensing complex triggering innate immunity. Curr Opin Immunol 19: 615-622.
121. Benko S, Philpott DJ, Girardin SE (2008) The microbial and danger signals that activate Nod-like receptors. Cytokine 43: 368-373.
122. Martinon F, Burns K, Tschopp J (2002) The inflammasome: a molecular platform triggering activation of inflammatory caspases and processing of proIL-beta. Mol Cell 10: 417-426.
123. Fritz JH, Ferrero RL, Philpott DJ, Girardin SE (2006) Nod-like proteins in immunity, inflammation and disease. Nat Immunol 7: 1250-1257.
124. Bass BL, Weintraub H (1988) An unwinding activity that covalently modifies its double-stranded RNA substrate. Cell 55: 1089-1098.
125. Hundley HA, Bass BL (2010) ADAR editing in double-stranded UTRs and other noncoding RNA sequences. Trends Biochem Sci 35: 377-383.
126. Nishikura K (2010) Functions and regulation of RNA editing by ADAR deaminases. Annu Rev Biochem 79: 321-349.
127. Samuel CE (2012) ADARs: viruses and innate immunity. Curr Top Microbiol Immunol 353: 163-195.
128. Doyle M, Jantsch MF (2002) New and old roles of the double-stranded RNA-binding domain. J Struct Biol 140: 147-153.
129. Herbert A, Alfken J, Kim YG, Mian IS, Nishikura K, et al. (1997) A Z-DNA binding domain present in the human editing enzyme, double-stranded RNA adenosine deaminase. Proc Natl Acad Sci U S A 94: 8421-8426.
130. Koeris M, Funke L, Shrestha J, Rich A, Maas S (2005) Modulation of ADAR1 editing activity by Z-RNA in vitro. Nucleic Acids Res 33: 5362-5370.
131. Patterson JB, Samuel CE (1995) Expression and regulation by interferon of a double-stranded-RNA-specific adenosine deaminase from human cells: evidence for two forms of the deaminase. Mol Cell Biol 15: 5376-5388.
132. Poulsen H, Nilsson J, Damgaard CK, Egebjerg J, Kjems J (2001) CRM1 mediates the export of ADAR1 through a nuclear export signal within the Z-DNA binding domain. Mol Cell Biol 21: 7862-7871.
133. Li Z, Wolff KC, Samuel CE (2010) RNA adenosine deaminase ADAR1 deficiency leads to increased activation of protein kinase PKR and reduced vesicular stomatitis virus growth following interferon treatment. Virology 396: 316-322.

134. Wong TC, Ayata M, Ueda S, Hirano A (1991) Role of biased hypermutation in evolution of subacute sclerosing panencephalitis virus from progenitor acute measles virus. J Virol 65: 2191-2199.
135. Ward SV, George CX, Welch MJ, Liou LY, Hahm B, et al. (2011) RNA editing enzyme adenosine deaminase is a restriction factor for controlling measles virus replication that also is required for embryogenesis. Proc Natl Acad Sci U S A 108: 331-336.
136. Rueda P, Garcia-Barreno B, Melero JA (1994) Loss of conserved cysteine residues in the attachment (G) glycoprotein of two human respiratory syncytial virus escape mutants that contain multiple A-G substitutions (hypermutations). Virology 198: 653-662.
137. Martinez I, Melero JA (2002) A model for the generation of multiple A to G transitions in the human respiratory syncytial virus genome: predicted RNA secondary structures as substrates for adenosine deaminases that act on RNA. J Gen Virol 83: 1445-1455.
138. Sharmeen L, Bass B, Sonenberg N, Weintraub H, Groudine M (1991) Tat-dependent adenosine-to-inosine modification of wild-type transactivation response RNA. Proc Natl Acad Sci U S A 88: 8096-8100.
139. Suspene R, Petit V, Puyraimond-Zemmour D, Aynaud MM, Henry M, et al. (2011) Double-stranded RNA adenosine deaminase ADAR-1-induced hypermutated genomes among inactivated seasonal influenza and live attenuated measles virus vaccines. J Virol 85: 2458-2462.
140. Cattaneo R, Billeter MA (1992) Mutations and A/I hypermutations in measles virus persistent infections. Curr Top Microbiol Immunol 176: 63-74.
141. Kumar M, Carmichael GG (1997) Nuclear antisense RNA induces extensive adenosine modifications and nuclear retention of target transcripts. Proc Natl Acad Sci U S A 94: 3542-3547.
142. Gandy SZ, Linnstaedt SD, Muralidhar S, Cashman KA, Rosenthal LJ, et al. (2007) RNA editing of the human herpesvirus 8 kaposin transcript eliminates its transforming activity and is induced during lytic replication. J Virol 81: 13544-13551.
143. Schoggins JW, Wilson SJ, Panis M, Murphy MY, Jones CT, et al. (2011) A diverse range of gene products are effectors of the type I interferon antiviral response. Nature 472: 481-485.
144. George CX, Gan Z, Liu Y, Samuel CE (2011) Adenosine deaminases acting on RNA, RNA editing, and interferon action. J Interferon Cytokine Res 31: 99-117.
145. Samuel CE (2001) Antiviral actions of interferons. Clin Microbiol Rev 14: 778-809, table of contents.
146. Clerzius G, Gelinas JF, Daher A, Bonnet M, Meurs EF, et al. (2009) ADAR1 interacts with PKR during human immunodeficiency virus infection of lymphocytes and contributes to viral replication. J Virol 83: 10119-10128.
147. Wong SK, Lazinski DW (2002) Replicating hepatitis delta virus RNA is edited in the nucleus by the small form of ADAR1. Proc Natl Acad Sci U S A 99: 15118-15123.

148. Sato S, Cornillez-Ty C, Lazinski DW (2004) By inhibiting replication, the large hepatitis delta antigen can indirectly regulate amber/W editing and its own expression. J Virol 78: 8120-8134.
149. Peisley A, Hur S (2013) Multi-level regulation of cellular recognition of viral dsRNA. Cell Mol Life Sci 70: 1949-1963.
150. Hunt K, Ehrenfeld E (1971) Cytoplasm poliovirus-infected HeLa cells inhibit cell-free hemoglobin sythesis. Nature 230: 91-94.
151. Kerr IM, Brown RE, Ball LA (1974) Increased sensitivity of cell-free protein synthesis to double-stranded RNA after interferon treatment. Nature 250: 57-59.
152. Freidman RM, Metz DH, Esteban M, Towell DR, Ball LA, et al. (1972) Mechanism of interferon action: inhibition of viral messenger ribonucleic acid translations in L-cell extracts. J Virol 10: 1184-1998.
153. Roberts WK, Clemens MJ, Kerr IM (1976) Interferon-induced inhibition of protein synthesis in L-cell extracts: an ATP-dependent step in the activation of an inhibitor by double-stranded RNA. Proc Natl Acad Sci U S A 73: 3136-3140.
154. Metz DH, Esteban M (1972) Interferon inhibits viral protein synthesis in L cells infected with vaccinia virus. Nature 238: 385-388.
155. Roberts WK, Hovanessian A, Brown RE, Clemens MJ, Kerr IM (1976) Interferon-mediated protein kinase and low-molecular-weight inhibitor of protein synthesis. Nature 264: 477-480.
156. Hovanessian AG, Brown RE, Kerr IM (1977) Synthesis of low molecular weight inhibitor of protein synthesis with enzyme from interferon-treated cells. Nature 268: 537-540.
157. Kerr IM, Brown RE, Hovanessian AG (1977) Nature of inhibitor of cell-free protein synthesis formed in response to interferon and double-stranded RNA. Nature 268: 540-542.
158. Garcia MA, Gil J, Ventoso I, Guerra S, Domingo E, et al. (2006) Impact of protein kinase PKR in cell biology: from antiviral to antiproliferative action. Microbiol Mol Biol Rev 70: 1032-1060.
159. Chong KL, Feng L, Schappert K, Meurs E, Donahue TF, et al. (1992) Human p68 kinase exhibits growth suppression in yeast and homology to the translational regulator GCN2. EMBO J 11: 1553-1562.
160. Nanduri S, Carpick BW, Yang Y, Williams BR, Qin J (1998) Structure of the double-stranded RNA-binding domain of the protein kinase PKR reveals the molecular basis of its dsRNA-mediated activation. EMBO J 17: 5458-5465.
161. Majumdar R, Maitra U (2005) Regulation of GTP hydrolysis prior to ribosomal AUG selection during eukaryotic translation initiation. EMBO J 24: 3737-3746.
162. Taylor SS, Haste NM, Ghosh G (2005) PKR and eIF2alpha: integration of kinase dimerization, activation, and substrate docking. Cell 122: 823-825.
163. Dey M, Cao C, Dar AC, Tamura T, Ozato K, et al. (2005) Mechanistic link between PKR dimerization, autophosphorylation, and eIF2alpha substrate recognition. Cell 122: 901-913.

164. Su Q, Wang S, Baltzis D, Qu LK, Wong AH, et al. (2006) Tyrosine phosphorylation acts as a molecular switch to full-scale activation of the eIF2alpha RNA-dependent protein kinase. Proc Natl Acad Sci U S A 103: 63-68.
165. Sudhakar A, Ramachandran A, Ghosh S, Hasnain SE, Kaufman RJ, et al. (2000) Phosphorylation of serine 51 in initiation factor 2 alpha (eIF2 alpha) promotes complex formation between eIF2 alpha(P) and eIF2B and causes inhibition in the guanine nucleotide exchange activity of eIF2B. Biochemistry 39: 12929-12938.
166. Hershey JW (1991) Translational control in mammalian cells. Annu Rev Biochem 60: 717-755.
167. Dar AC, Dever TE, Sicheri F (2005) Higher-order substrate recognition of eIF2alpha by the RNA-dependent protein kinase PKR. Cell 122: 887-900.
168. Kimball SR, Jefferson LS (2004) Amino acids as regulators of gene expression. Nutr Metab (Lond) 1: 3.
169. Walsh D, Mohr I (2011) Viral subversion of the host protein synthesis machinery. Nat Rev Microbiol 9: 860-875.
170. Schulz O, Pichlmair A, Rehwinkel J, Rogers NC, Scheuner D, et al. (2010) Protein kinase R contributes to immunity against specific viruses by regulating interferon mRNA integrity. Cell Host Microbe 7: 354-361.
171. Bergmann M, Garcia-Sastre A, Carnero E, Pehamberger H, Wolff K, et al. (2000) Influenza virus NS1 protein counteracts PKR-mediated inhibition of replication. J Virol 74: 6203-6206.
172. Noguchi T, Satoh S, Noshi T, Hatada E, Fukuda R, et al. (2001) Effects of mutation in hepatitis C virus nonstructural protein 5A on interferon resistance mediated by inhibition of PKR kinase activity in mammalian cells. Microbiol Immunol 45: 829-840.
173. Chinsangaram J, Koster M, Grubman MJ (2001) Inhibition of L-deleted foot-and-mouth disease virus replication by alpha/beta interferon involves double-stranded RNA-dependent protein kinase. J Virol 75: 5498-5503.
174. Yeung MC, Chang DL, Camantigue RE, Lau AS (1999) Inhibitory role of the host apoptogenic gene PKR in the establishment of persistent infection by encephalomyocarditis virus in U937 cells. Proc Natl Acad Sci U S A 96: 11860-11865.
175. Samuel MA, Whitby K, Keller BC, Marri A, Barchet W, et al. (2006) PKR and RNase L contribute to protection against lethal West Nile Virus infection by controlling early viral spread in the periphery and replication in neurons. J Virol 80: 7009-7019.
176. Chen CW, Tsay YG, Wu HL, Lee CH, Chen DS, et al. (2002) The double-stranded RNA-activated kinase, PKR, can phosphorylate hepatitis D virus small delta antigen at functional serine and threonine residues. J Biol Chem 277: 33058-33067.
177. Gorchakov R, Frolova E, Williams BR, Rice CM, Frolov I (2004) PKR-dependent and -independent mechanisms are involved in translational shutoff during Sindbis virus infection. J Virol 78: 8455-8467.

178. Iwasaki A (2012) A virological view of innate immune recognition. Annu Rev Microbiol 66: 177-196.
179. Zhou A, Hassel BA, Silverman RH (1993) Expression cloning of 2-5A-dependent RNAase: a uniquely regulated mediator of interferon action. Cell 72: 753-765.
180. Kerr IM, Brown RE (1978) pppA2'p5'A2'p5'A: an inhibitor of protein synthesis synthesized with an enzyme fraction from interferon-treated cells. Proc Natl Acad Sci U S A 75: 256-260.
181. Hovanessian AG, Kerr IM (1979) The (2'-5') oligoadenylate (pppA2'-5'A2'-5'A) synthetase and protein kinase(s) from interferon-treated cells. Eur J Biochem 93: 515-526.
182. Witt PL, Marie I, Robert N, Irizarry A, Borden EC, et al. (1993) Isoforms p69 and p100 of 2',5'-oligoadenylate synthetase induced differentially by interferons in vivo and in vitro. J Interferon Res 13: 17-23.
183. Witt PL, Spear GT, Helgeson DO, Lindstrom MJ, Smalley RV, et al. (1990) Basal and interferon-induced 2',5'-oligoadenylate synthetase in human monocytes, lymphocytes, and peritoneal macrophages. J Interferon Res 10: 393-402.
184. Chebath J, Benech P, Hovanessian A, Galabru J, Revel M (1987) Four different forms of interferon-induced 2',5'-oligo(A) synthetase identified by immunoblotting in human cells. J Biol Chem 262: 3852-3857.
185. Hovanessian AG, Laurent AG, Chebath J, Galabru J, Robert N, et al. (1987) Identification of 69-kd and 100-kd forms of 2-5A synthetase in interferon-treated human cells by specific monoclonal antibodies. EMBO J 6: 1273-1280.
186. Hovanessian AG, Justesen J (2007) The human 2'-5'oligoadenylate synthetase family: unique interferon-inducible enzymes catalyzing 2'-5' instead of 3'-5' phosphodiester bond formation. Biochimie 89: 779-788.
187. Hovnanian A, Rebouillat D, Mattei MG, Levy ER, Marie I, et al. (1998) The human 2',5'-oligoadenylate synthetase locus is composed of three distinct genes clustered on chromosome 12q24.2 encoding the 100-, 69-, and 40-kDa forms. Genomics 52: 267-277.
188. Hovnanian A, Rebouillat D, Levy ER, Mattei MG, Hovanessian AG (1999) The human 2',5'-oligoadenylate synthetase-like gene (OASL) encoding the interferon-induced 56-kDa protein maps to chromosome 12q24.2 in the proximity of the 2',5'-OAS locus. Genomics 56: 362-363.
189. Marie I, Hovanessian AG (1992) The 69-kDa 2-5A synthetase is composed of two homologous and adjacent functional domains. J Biol Chem 267: 9933-9939.
190. Rebouillat D, Marie I, Hovanessian AG (1998) Molecular cloning and characterization of two related and interferon-induced 56-kDa and 30-kDa proteins highly similar to 2'-5' oligoadenylate synthetase. Eur J Biochem 257: 319-330.
191. Benech P, Mory Y, Revel M, Chebath J (1985) Structure of two forms of the interferon-induced (2'-5') oligo A synthetase of human cells based on cDNAs and gene sequences. EMBO J 4: 2249-2256.
192. Ghosh SK, Kusari J, Bandyopadhyay SK, Samanta H, Kumar R, et al. (1991) Cloning, sequencing, and expression of two murine 2'-5'-oligoadenylate synthetases. Structure-function relationships. J Biol Chem 266: 15293-15299.

193. Kristiansen H, Gad HH, Eskildsen-Larsen S, Despres P, Hartmann R (2011) The oligoadenylate synthetase family: an ancient protein family with multiple antiviral activities. J Interferon Cytokine Res 31: 41-47.
194. Saunders ME, Gewert DR, Tugwell ME, McMahon M, Williams BR (1985) Human 2-5A synthetase: characterization of a novel cDNA and corresponding gene structure. EMBO J 4: 1761-1768.
195. Wathelet M, Moutschen S, Cravador A, DeWit L, Defilippi P, et al. (1986) Full-length sequence and expression of the 42 kDa 2-5A synthetase induced by human interferon. FEBS Lett 196: 113-120.
196. Marie I, Rebouillat D, Hovanessian AG (1999) The expression of both domains of the 69/71 kDa 2',5' oligoadenylate synthetase generates a catalytically active enzyme and mediates an anti-viral response. Eur J Biochem 262: 155-165.
197. Edwalds-Gilbert G, Veraldi KL, Milcarek C (1997) Alternative poly(A) site selection in complex transcription units: means to an end? Nucleic Acids Res 25: 2547-2561.
198. Rebouillat D, Hovnanian A, Marie I, Hovanessian AG (1999) The 100-kDa 2',5'-oligoadenylate synthetase catalyzing preferentially the synthesis of dimeric pppA2'p5'A molecules is composed of three homologous domains. J Biol Chem 274: 1557-1565.
199. Benech P, Merlin G, Revel M, Chebath J (1985) 3' end structure of the human (2'-5') oligo A synthetase gene: prediction of two distinct proteins with cell type-specific expression. Nucleic Acids Res 13: 1267-1281.
200. Hartmann R, Olsen HS, Widder S, Jorgensen R, Justesen J (1998) p59OASL, a 2'-5' oligoadenylate synthetase like protein: a novel human gene related to the 2'-5' oligoadenylate synthetase family. Nucleic Acids Res 26: 4121-4128.
201. Guo X, Li X, Xu Y, Sun T, Yang G, et al. (2012) Identification of OASL d, a splice variant of human OASL, with antiviral activity. Int J Biochem Cell Biol 44: 1133-1138.
202. Torralba S, Sojat J, Hartmann R (2008) 2'-5' oligoadenylate synthetase shares active site architecture with the archaeal CCA-adding enzyme. Cell Mol Life Sci 65: 2613-2620.
203. Holm L, Sander C (1995) DNA polymerase beta belongs to an ancient nucleotidyltransferase superfamily. Trends Biochem Sci 20: 345-347.
204. Marie I, Svab J, Robert N, Galabru J, Hovanessian AG (1990) Differential expression and distinct structure of 69- and 100-kDa forms of 2-5A synthetase in human cells treated with interferon. J Biol Chem 265: 18601-18607.
205. Hovanessian AG (2007) On the discovery of interferon-inducible, double-stranded RNA activated enzymes: the 2'-5'oligoadenylate synthetases and the protein kinase PKR. Cytokine Growth Factor Rev 18: 351-361.
206. Sarkar SN, Miyagi M, Crabb JW, Sen GC (2002) Identification of the substrate-binding sites of 2'-5'-oligoadenylate synthetase. J Biol Chem 277: 24321-24330.

207. Ghosh A, Sarkar SN, Guo W, Bandyopadhyay S, Sen GC (1997) Enzymatic activity of 2'-5'-oligoadenylate synthetase is impaired by specific mutations that affect oligomerization of the protein. J Biol Chem 272: 33220-33226.
208. Justesen J, Ferbus D, Thang MN (1980) Elongation mechanism and substrate specificity of 2',5'-oligoadenylate synthetase. Proc Natl Acad Sci U S A 77: 4618-4622.
209. Sarkar SN, Ghosh A, Wang HW, Sung SS, Sen GC (1999) The nature of the catalytic domain of 2'-5'-oligoadenylate synthetases. J Biol Chem 274: 25535-25542.
210. Marie I, Blanco J, Rebouillat D, Hovanessian AG (1997) 69-kDa and 100-kDa isoforms of interferon-induced (2'-5')oligoadenylate synthetase exhibit differential catalytic parameters. Eur J Biochem 248: 558-566.
211. Deo S, Patel TR, Dzananovic E, Booy EP, Zeid K, et al. (2014) Activation of 2' 5'-oligoadenylate synthetase by stem loops at the 5'-end of the West Nile virus genome. PLoS One 9: e92545.
212. Meng H, Deo S, Xiong S, Dzananovic E, Donald LJ, et al. (2012) Regulation of the interferon-inducible 2'-5'-oligoadenylate synthetases by adenovirus VA(I) RNA. J Mol Biol 422: 635-649.
213. Hartmann R, Norby PL, Martensen PM, Jorgensen P, James MC, et al. (1998) Activation of 2'-5' oligoadenylate synthetase by single-stranded and double-stranded RNA aptamers. J Biol Chem 273: 3236-3246.
214. Perelygin AA, Lear TL, Zharkikh AA, Brinton MA (2005) Structure of equine 2'-5'oligoadenylate synthetase (OAS) gene family and FISH mapping of OAS genes to ECA8p15-->p14 and BTA17q24-->q25. Cytogenet Genome Res 111: 51-56.
215. Perelygin AA, Zharkikh AA, Scherbik SV, Brinton MA (2006) The mammalian 2'-5' oligoadenylate synthetase gene family: evidence for concerted evolution of paralogous Oas1 genes in Rodentia and Artiodactyla. J Mol Evol 63: 562-576.
216. Kakuta S, Shibata S, Iwakura Y (2002) Genomic structure of the mouse 2',5'-oligoadenylate synthetase gene family. J Interferon Cytokine Res 22: 981-993.
217. Hartmann R, Justesen J, Sarkar SN, Sen GC, Yee VC (2003) Crystal structure of the 2'-specific and double-stranded RNA-activated interferon-induced antiviral protein 2'-5'-oligoadenylate synthetase. Mol Cell 12: 1173-1185.
218. Yamamoto A, Iwata A, Koh Y, Kawai S, Murayama S, et al. (1998) Two types of chicken 2',5'-oligoadenylate synthetase mRNA derived from alleles at a single locus. Biochim Biophys Acta 1395: 181-191.
219. Pari M, Kuusksalu A, Lopp A, Reintamm T, Justesen J, et al. (2007) Expression and characterization of recombinant 2',5'-oligoadenylate synthetase from the marine sponge Geodia cydonium. FEBS J 274: 3462-3474.
220. Kjaer KH, Poulsen JB, Reintamm T, Saby E, Martensen PM, et al. (2009) Evolution of the 2'-5'-oligoadenylate synthetase family in eukaryotes and bacteria. J Mol Evol 69: 612-624.
221. Pari M, Kuusksalu A, Lopp A, Kjaer KH, Justesen J, et al. (2014) Enzymatically active 2',5'-oligoadenylate synthetases are widely distributed among Metazoa, including protostome lineage. Biochimie 97: 200-209.

222. Donovan J, Dufner M, Korennykh A (2013) Structural basis for cytosolic double-stranded RNA surveillance by human oligoadenylate synthetase 1. Proc Natl Acad Sci U S A 110: 1652-1657.
223. Sarkar SN, Kessler SP, Rowe TM, Pandey M, Ghosh A, et al. (2005) Natural mutations in a 2'-5' oligoadenylate synthetase transgene revealed residues essential for enzyme activity. Biochemistry 44: 6837-6843.
224. Besse S, Rebouillat D, Marie I, Puvion-Dutilleul F, Hovanessian AG (1998) Ultrastructural localization of interferon-inducible double-stranded RNA-activated enzymes in human cells. Exp Cell Res 239: 379-392.
225. Floyd-Smith G, Slattery E, Lengyel P (1981) Interferon action: RNA cleavage pattern of a (2'-5')oligoadenylate--dependent endonuclease. Science 212: 1030-1032.
226. Kubota K, Nakahara K, Ohtsuka T, Yoshida S, Kawaguchi J, et al. (2004) Identification of 2'-phosphodiesterase, which plays a role in the 2-5A system regulated by interferon. J Biol Chem 279: 37832-37841.
227. Knight M, Cayley PJ, Silverman RH, Wreschner DH, Gilbert CS, et al. (1980) Radioimmune, radiobinding and HPLC analysis of 2-5A and related oligonucleotides from intact cells. Nature 288: 189-192.
228. Rebouillat D, Hovanessian AG (1999) The human 2',5'-oligoadenylate synthetase family: interferon-induced proteins with unique enzymatic properties. J Interferon Cytokine Res 19: 295-308.
229. Ibsen MS, Gad HH, Thavachelvam K, Boesen T, Despres P, et al. (2014) The 2'-5' oligoadenylate synthetase 3 (OAS3) enzyme potently synthesizes the 2'-5' oligoadenylates required for RNase L activation. J Virol.
230. Dong B, Xu L, Zhou A, Hassel BA, Lee X, et al. (1994) Intrinsic molecular activities of the interferon-induced 2-5A-dependent RNase. J Biol Chem 269: 14153-14158.
231. Han Y, Donovan J, Rath S, Whitney G, Chitrakar A, et al. (2014) Structure of human RNase L reveals the basis for regulated RNA decay in the IFN response. Science 343: 1244-1248.
232. Huang H, Zeqiraj E, Dong B, Jha BK, Duffy NM, et al. (2014) Dimeric structure of pseudokinase RNase L bound to 2-5A reveals a basis for interferon-induced antiviral activity. Mol Cell 53: 221-234.
233. Malathi K, Saito T, Crochet N, Barton DJ, Gale M, Jr., et al. (2010) RNase L releases a small RNA from HCV RNA that refolds into a potent PAMP. RNA 16: 2108-2119.
234. Castelli JC, Hassel BA, Maran A, Paranjape J, Hewitt JA, et al. (1998) The role of 2'-5' oligoadenylate-activated ribonuclease L in apoptosis. Cell Death Differ 5: 313-320.
235. Zhou A, Paranjape J, Brown TL, Nie H, Naik S, et al. (1997) Interferon action and apoptosis are defective in mice devoid of 2',5'-oligoadenylate-dependent RNase L. EMBO J 16: 6355-6363.
236. Diaz-Guerra M, Rivas C, Esteban M (1997) Activation of the IFN-inducible enzyme RNase L causes apoptosis of animal cells. Virology 236: 354-363.
237. Silverman RH (2007) Viral encounters with 2',5'-oligoadenylate synthetase and RNase L during the interferon antiviral response. J Virol 81: 12720-12729.

238. Silverman RH, Skehel JJ, James TC, Wreschner DH, Kerr IM (1983) rRNA cleavage as an index of ppp(A2'p)nA activity in interferon-treated encephalomyocarditis virus-infected cells. J Virol 46: 1051-1055.
239. Zhou A, Paranjape JM, Hassel BA, Nie H, Shah S, et al. (1998) Impact of RNase L overexpression on viral and cellular growth and death. J Interferon Cytokine Res 18: 953-961.
240. Kristiansen H, Scherer CA, McVean M, Iadonato SP, Vends S, et al. (2010) Extracellular 2'-5' oligoadenylate synthetase stimulates RNase L-independent antiviral activity: a novel mechanism of virus-induced innate immunity. J Virol 84: 11898-11904.
241. Chebath J, Benech P, Revel M, Vigneron M (1987) Constitutive expression of (2'-5') oligo A synthetase confers resistance to picornavirus infection. Nature 330: 587-588.
242. Flodstrom-Tullberg M, Hultcrantz M, Stotland A, Maday A, Tsai D, et al. (2005) RNase L and double-stranded RNA-dependent protein kinase exert complementary roles in islet cell defense during coxsackievirus infection. J Immunol 174: 1171-1177.
243. Maitra RK, Silverman RH (1998) Regulation of human immunodeficiency virus replication by 2',5'-oligoadenylate-dependent RNase L. J Virol 72: 1146-1152.
244. Lin RJ, Yu HP, Chang BL, Tang WC, Liao CL, et al. (2009) Distinct antiviral roles for human 2',5'-oligoadenylate synthetase family members against dengue virus infection. J Immunol 183: 8035-8043.
245. Bonnevie-Nielsen V, Larsen ML, Frifelt JJ, Michelsen B, Lernmark A (1989) Association of IDDM and attenuated response of 2',5'-oligoadenylate synthetase to yellow fever vaccine. Diabetes 38: 1636-1642.
246. Knapp S, Yee LJ, Frodsham AJ, Hennig BJ, Hellier S, et al. (2003) Polymorphisms in interferon-induced genes and the outcome of hepatitis C virus infection: roles of MxA, OAS-1 and PKR. Genes Immun 4: 411-419.
247. Bonnevie-Nielsen V, Martensen PM, Justesen J, Kyvik KO, Kristensen B, et al. (2000) The antiviral 2',5'-oligoadenylate synthetase is persistently activated in type 1 diabetes. Clin Immunol 96: 11-18.
248. Arnold RS, Makarova NV, Osunkoya AO, Suppiah S, Scott TA, et al. (2010) XMRV infection in patients with prostate cancer: novel serologic assay and correlation with PCR and FISH. Urology 75: 755-761.
249. Ireland DD, Stohlman SA, Hinton DR, Kapil P, Silverman RH, et al. (2009) RNase L mediated protection from virus induced demyelination. PLoS Pathog 5: e1000602.
250. Li XL, Ezelle HJ, Kang TJ, Zhang L, Shirey KA, et al. (2008) An essential role for the antiviral endoribonuclease, RNase-L, in antibacterial immunity. Proc Natl Acad Sci U S A 105: 20816-20821.
251. Rayamajhi M, Humann J, Penheiter K, Andreasen K, Lenz LL (2010) Induction of IFN-alphabeta enables Listeria monocytogenes to suppress macrophage activation by IFN-gamma. J Exp Med 207: 327-337.
252. Shahangian A, Chow EK, Tian X, Kang JR, Ghaffari A, et al. (2009) Type I IFNs mediate development of postinfluenza bacterial pneumonia in mice. J Clin Invest 119: 1910-1920.

253. Dugan JW, Albor A, David L, Fowlkes J, Blackledge MT, et al. (2009) Nucleotide oligomerization domain-2 interacts with 2'-5'-oligoadenylate synthetase type 2 and enhances RNase-L function in THP-1 cells. Mol Immunol 47: 560-566.
254. Mitra A, Higgins DW, Langenberg WG, Nie H, Sengupta DN, et al. (1996) A mammalian 2-5A system functions as an antiviral pathway in transgenic plants. Proc Natl Acad Sci U S A 93: 6780-6785.
255. Sperling J, Chebath J, Arad-Dann H, Offen D, Spann P, et al. (1991) Possible involvement of (2'5')oligoadenylate synthetase activity in pre-mRNA splicing. Proc Natl Acad Sci U S A 88: 10377-10381.
256. Hornung V, Ellegast J, Kim S, Brzozka K, Jung A, et al. (2006) 5'-Triphosphate RNA is the ligand for RIG-I. Science 314: 994-997.
257. Schmidt A, Schwerd T, Hamm W, Hellmuth JC, Cui S, et al. (2009) 5'-triphosphate RNA requires base-paired structures to activate antiviral signaling via RIG-I. Proc Natl Acad Sci U S A 106: 12067-12072.
258. Shipley JG, Vandergaast R, Deng L, Mariuzza RA, Fredericksen BL (2012) Identification of multiple RIG-I-specific pathogen associated molecular patterns within the West Nile virus genome and antigenome. Virology 432: 232-238.
259. Schlee M, Roth A, Hornung V, Hagmann CA, Wimmenauer V, et al. (2009) Recognition of 5' triphosphate by RIG-I helicase requires short blunt double-stranded RNA as contained in panhandle of negative-strand virus. Immunity 31: 25-34.
260. Saito T, Owen DM, Jiang F, Marcotrigiano J, Gale M, Jr. (2008) Innate immunity induced by composition-dependent RIG-I recognition of hepatitis C virus RNA. Nature 454: 523-527.
261. Kato H, Takeuchi O, Mikamo-Satoh E, Hirai R, Kawai T, et al. (2008) Length-dependent recognition of double-stranded ribonucleic acids by retinoic acid-inducible gene-I and melanoma differentiation-associated gene 5. J Exp Med 205: 1601-1610.
262. Pichlmair A, Schulz O, Tan CP, Rehwinkel J, Kato H, et al. (2009) Activation of MDA5 requires higher-order RNA structures generated during virus infection. J Virol 83: 10761-10769.
263. Leonard JN, Ghirlando R, Askins J, Bell JK, Margulies DH, et al. (2008) The TLR3 signaling complex forms by cooperative receptor dimerization. Proc Natl Acad Sci U S A 105: 258-263.
264. Li K, Li NL, Wei D, Pfeffer SR, Fan M, et al. (2012) Activation of chemokine and inflammatory cytokine response in hepatitis C virus-infected hepatocytes depends on Toll-like receptor 3 sensing of hepatitis C virus double-stranded RNA intermediates. Hepatology 55: 666-675.
265. Lund JM, Alexopoulou L, Sato A, Karow M, Adams NC, et al. (2004) Recognition of single-stranded RNA viruses by Toll-like receptor 7. Proc Natl Acad Sci U S A 101: 5598-5603.
266. Tian B, Bevilacqua PC, Diegelman-Parente A, Mathews MB (2004) The double-stranded-RNA-binding motif: interference and much more. Nat Rev Mol Cell Biol 5: 1013-1023.

267. Stefl R, Xu M, Skrisovska L, Emeson RB, Allain FH (2006) Structure and specific RNA binding of ADAR2 double-stranded RNA binding motifs. Structure 14: 345-355.
268. Stefl R, Oberstrass FC, Hood JL, Jourdan M, Zimmermann M, et al. (2010) The solution structure of the ADAR2 dsRBM-RNA complex reveals a sequence-specific readout of the minor groove. Cell 143: 225-237.
269. Gan J, Tropea JE, Austin BP, Court DL, Waugh DS, et al. (2006) Structural insight into the mechanism of double-stranded RNA processing by ribonuclease III. Cell 124: 355-366.
270. McKenna SA, Kim I, Liu CW, Puglisi JD (2006) Uncoupling of RNA binding and PKR kinase activation by viral inhibitor RNAs. J Mol Biol 358: 1270-1285.
271. Kim I, Liu CW, Puglisi JD (2006) Specific recognition of HIV TAR RNA by the dsRNA binding domains (dsRBD1-dsRBD2) of PKR. J Mol Biol 358: 430-442.
272. Dzananovic E, Patel TR, Deo S, McEleney K, Stetefeld J, et al. (2013) Recognition of viral RNA stem-loops by the tandem double-stranded RNA binding domains of PKR. RNA 19: 333-344.
273. Peisley A, Hur S (2012) Multi-level regulation of cellular recognition of viral dsRNA. Cell Mol Life Sci.
274. Nallagatla SR, Hwang J, Toroney R, Zheng X, Cameron CE, et al. (2007) 5'-triphosphate-dependent activation of PKR by RNAs with short stem-loops. Science 318: 1455-1458.
275. Desai SY, Sen GC (1997) Effects of varying lengths of double-stranded RNA on binding and activation of 2'-5'-oligoadenylate synthetase. J Interferon Cytokine Res 17: 531-536.
276. Kodym R, Kodym E, Story MD (2009) 2'-5'-Oligoadenylate synthetase is activated by a specific RNA sequence motif. Biochem Biophys Res Commun 388: 317-322.
277. Nilsen TW, Maroney PA, Robertson HD, Baglioni C (1982) Heterogeneous nuclear RNA promotes synthesis of (2',5')oligoadenylate and is cleaved by the (2',5')oligoadenylate-activated endoribonuclease. Mol Cell Biol 2: 154-160.
278. Molinaro RJ, Jha BK, Malathi K, Varambally S, Chinnaiyan AM, et al. (2006) Selection and cloning of poly(rC)-binding protein 2 and Raf kinase inhibitor protein RNA activators of 2',5'-oligoadenylate synthetase from prostate cancer cells. Nucleic Acids Res 34: 6684-6695.
279. Zhang K, Nicholson AW (1997) Regulation of ribonuclease III processing by double-helical sequence antideterminants. Proc Natl Acad Sci U S A 94: 13437-13441.
280. Ryter JM, Schultz SC (1998) Molecular basis of double-stranded RNA-protein interactions: structure of a dsRNA-binding domain complexed with dsRNA. EMBO J 17: 7505-7513.
281. Doyle M, Jantsch MF (2003) Distinct in vivo roles for double-stranded RNA-binding domains of the Xenopus RNA-editing enzyme ADAR1 in chromosomal targeting. J Cell Biol 161: 309-319.
282. Saunders LR, Barber GN (2003) The dsRNA binding protein family: critical roles, diverse cellular functions. FASEB J 17: 961-983.

283. Pabo CO, Sauer RT (1984) Protein-DNA recognition. Annu Rev Biochem 53: 293-321.
284. Diebold SS, Massacrier C, Akira S, Paturel C, Morel Y, et al. (2006) Nucleic acid agonists for Toll-like receptor 7 are defined by the presence of uridine ribonucleotides. Eur J Immunol 36: 3256-3267.
285. Anderson BR, Muramatsu H, Jha BK, Silverman RH, Weissman D, et al. (2011) Nucleoside modifications in RNA limit activation of 2'-5'-oligoadenylate synthetase and increase resistance to cleavage by RNase L. Nucleic Acids Res 39: 9329-9338.
286. Kohler A, Hurt E (2007) Exporting RNA from the nucleus to the cytoplasm. Nat Rev Mol Cell Biol 8: 761-773.
287. Asnis DS, Conetta R, Teixeira AA, Waldman G, Sampson BA (2000) The West Nile virus outbreak of 1999 in New York: the Flushing Hospital experience. (vol 30, pg 413, 2000). Clinical Infectious Diseases 30: 841-841.
288. Ceausu E, Erscoiu S, Calistru P, Ispas D, Dorobat O, et al. (1997) Clinical manifestations in the West Nile virus outbreak. Rom J Virol 48: 3-11.
289. Calisher CH (2000) West Nile virus in the New World: appearance, persistence, and adaptation to a new econiche--an opportunity taken. Viral Immunol 13: 411-414.
290. undetermined (2007).
291. Brinton MA (2001) Host factors involved in West Nile virus replication. West Nile Virus: Detection, Surveillance, and Control 951: 207-219.
292. Brinton MA (2002) The molecular biology of West Nile virus: A new invader of the Western hemisphere. Annual Review of Microbiology 56: 371-402.
293. Chambers TJ, Hahn CS, Galler R, Rice CM (1990) Flavivirus Genome Organization, Expression, and Replication. Annual Review of Microbiology 44: 649-688.
294. Ivanyi-Nagy R, Darlix JL (2012) Core protein-mediated 5'-3' annealing of the West Nile virus genomic RNA in vitro. Virus Res 167: 226-235.
295. Markoff L (2003) 5 '- and 3 '-noncoding regions in flavivirus RNA. Flaviviruses: Structure, Replication and Evolution 59: 177-228.
296. Zhang B, Dong H, Stein DA, Iversen PL, Shi PY (2008) West Nile virus genome cyclization and RNA replication require two pairs of long-distance RNA interactions. Virology 373: 1-13.
297. Borisevich V, Seregin A, Nistler R, Mutabazi D, Yamshchikov V (2006) Biological properties of chimeric West Nile viruses. Virology 349: 371-381.
298. Lodeiro MF, Filomatori CV, Gamarnik AV (2009) Structural and functional studies of the promoter element for dengue virus RNA replication. J Virol 83: 993-1008.
299. Polacek C, Foley JE, Harris E (2009) Conformational changes in the solution structure of the dengue virus 5' end in the presence and absence of the 3' untranslated region. J Virol 83: 1161-1166.
300. Brinton MA, Fernandez AV, Dispoto JH (1986) The 3'-nucleotides of flavivirus genomic RNA form a conserved secondary structure. Virology 153: 113-121.
301. Dong H, Zhang B, Shi PY (2008) Terminal structures of West Nile virus genomic RNA and their interactions with viral NS5 protein. Virology 381: 123-135.

302. Davis WG, Basu M, Elrod EJ, Germann MW, Brinton MA (2013) Identification of cis-acting nucleotides and a structural feature in West Nile virus 3'-terminus RNA that facilitate viral minus strand RNA synthesis. J Virol 87: 7622-7636.
303. Villordo SM, Gamarnik AV (2009) Genome cyclization as strategy for flavivirus RNA replication. Virus Res 139: 230-239.
304. Friebe P, Harris E (2010) Interplay of RNA elements in the dengue virus 5' and 3' ends required for viral RNA replication. J Virol 84: 6103-6118.
305. Friebe P, Shi PY, Harris E (2011) The 5' and 3' downstream AUG region elements are required for mosquito-borne flavivirus RNA replication. J Virol 85: 1900-1905.
306. You S, Padmanabhan R (1999) A novel in vitro replication system for Dengue virus. Initiation of RNA synthesis at the 3'-end of exogenous viral RNA templates requires 5'- and 3'-terminal complementary sequence motifs of the viral RNA. J Biol Chem 274: 33714-33722.
307. Lo MK, Tilgner M, Bernard KA, Shi PY (2003) Functional analysis of mosquito-borne flavivirus conserved sequence elements within 3' untranslated region of West Nile virus by use of a reporting replicon that differentiates between viral translation and RNA replication. J Virol 77: 10004-10014.
308. Alvarez DE, Lodeiro MF, Filomatori CV, Fucito S, Mondotte JA, et al. (2006) Structural and functional analysis of dengue virus RNA. Novartis Found Symp 277: 120-132; discussion 132-125, 251-123.
309. Alvarez DE, Lodeiro MF, Luduena SJ, Pietrasanta LI, Gamarnik AV (2005) Long-range RNA-RNA interactions circularize the dengue virus genome. J Virol 79: 6631-6643.
310. Davis WG, Blackwell JL, Shi PY, Brinton MA (2007) Interaction between the cellular protein eEF1A and the 3'-terminal stem-loop of West Nile virus genomic RNA facilitates viral minus-strand RNA synthesis. J Virol 81: 10172-10187.
311. Davidson AD (2009) Chapter 2. New insights into flavivirus nonstructural protein 5. Adv Virus Res 74: 41-101.
312. Polacek C, Friebe P, Harris E (2009) Poly(A)-binding protein binds to the non-polyadenylated 3' untranslated region of dengue virus and modulates translation efficiency. J Gen Virol 90: 687-692.
313. Vashist S, Bhullar D, Vrati S (2011) La protein can simultaneously bind to both 3'- and 5'-noncoding regions of Japanese encephalitis virus genome. DNA Cell Biol 30: 339-346.
314. Wolin SL, Cedervall T (2002) The La protein. Annu Rev Biochem 71: 375-403.
315. Brinton MA (2014) Replication cycle and molecular biology of the West Nile virus. Viruses 6: 13-53.
316. Samuel MA, Diamond MS (2005) Alpha/beta interferon protects against lethal West Nile virus infection by restricting cellular tropism and enhancing neuronal survival. J Virol 79: 13350-13361.
317. Daffis S, Samuel MA, Suthar MS, Gale M, Jr., Diamond MS (2008) Toll-like receptor 3 has a protective role against West Nile virus infection. J Virol 82: 10349-10358.

318. Fredericksen BL, Keller BC, Fornek J, Katze MG, Gale M, Jr. (2008) Establishment and maintenance of the innate antiviral response to West Nile Virus involves both RIG-I and MDA5 signaling through IPS-1. J Virol 82: 609-616.
319. Liu WJ, Chen HB, Wang XJ, Huang H, Khromykh AA (2004) Analysis of adaptive mutations in Kunjin virus replicon RNA reveals a novel role for the flavivirus nonstructural protein NS2A in inhibition of beta interferon promoter-driven transcription. J Virol 78: 12225-12235.
320. Fredericksen BL, Gale M, Jr. (2006) West Nile virus evades activation of interferon regulatory factor 3 through RIG-I-dependent and -independent pathways without antagonizing host defense signaling. J Virol 80: 2913-2923.
321. Keller BC, Fredericksen BL, Samuel MA, Mock RE, Mason PW, et al. (2006) Resistance to alpha/beta interferon is a determinant of West Nile virus replication fitness and virulence. Journal of Virology 80: 9424-9434.
322. Wilson JR, de Sessions PF, Leon MA, Scholle F (2008) West Nile virus nonstructural protein 1 inhibits TLR3 signal transduction. J Virol 82: 8262-8271.
323. Arjona A, Ledizet M, Anthony K, Bonafe N, Modis Y, et al. (2007) West Nile virus envelope protein inhibits dsRNA-induced innate immune responses. J Immunol 179: 8403-8409.
324. Morrey JD, Day CW, Julander JG, Blatt LM, Smee DF, et al. (2004) Effect of interferon-alpha and interferon-inducers on West Nile virus in mouse and hamster animal models. Antivir Chem Chemother 15: 101-109.
325. Daffis S, Suthar MS, Gale M, Jr., Diamond MS (2009) Measure and countermeasure: type I IFN (IFN-alpha/beta) antiviral response against West Nile virus. J Innate Immun 1: 435-445.
326. Taguchi T, Nagano-Fujii M, Akutsu M, Kadoya H, Ohgimoto S, et al. (2004) Hepatitis C virus NS5A protein interacts with 2',5'-oligoadenylate synthetase and inhibits antiviral activity of IFN in an IFN sensitivity-determining region-independent manner. J Gen Virol 85: 959-969.
327. Washenberger CL, Han JQ, Kechris KJ, Jha BK, Silverman RH, et al. (2007) Hepatitis C virus RNA: dinucleotide frequencies and cleavage by RNase L. Virus Res 130: 85-95.
328. Rios JJ, Perelygin AA, Long MT, Lear TL, Zharkikh AA, et al. (2007) Characterization of the equine 2'-5' oligoadenylate synthetase 1 (OAS1) and ribonuclease L (RNASEL) innate immunity genes. BMC Genomics 8: 313.
329. Tag-El-Din-Hassan HT, Sasaki N, Moritoh K, Torigoe D, Maeda A, et al. (2012) The chicken 2'-5' oligoadenylate synthetase A inhibits the replication of West Nile virus. Jpn J Vet Res 60: 95-103.
330. Sangster MY, Urosevic N, Mansfield JP, Mackenzie JS, Shellam GR (1994) Mapping the Flv locus controlling resistance to flaviviruses on mouse chromosome 5. J Virol 68: 448-452.
331. Lim JK, Lisco A, McDermott DH, Huynh L, Ward JM, et al. (2009) Genetic variation in OAS1 is a risk factor for initial infection with West Nile virus in man. PLoS Pathog 5: e1000321.

332. Bigham AW, Buckingham KJ, Husain S, Emond MJ, Bofferding KM, et al. (2011) Host genetic risk factors for West Nile virus infection and disease progression. PLoS One 6: e24745.
333. Cai Y, Chen Q, Zhou W, Chu C, Ji W, et al. (2014) Association analysis of polymorphisms in OAS1 with susceptibility and severity of hand, foot and mouth disease. Int J Immunogenet.
334. Kajaste-Rudnitski A, Mashimo T, Frenkiel MP, Guenet JL, Lucas M, et al. (2006) The 2',5'-oligoadenylate synthetase 1b is a potent inhibitor of West Nile virus replication inside infected cells. J Biol Chem 281: 4624-4637.
335. Yakub I, Lillibridge KM, Moran A, Gonzalez OY, Belmont J, et al. (2005) Single nucleotide polymorphisms in genes for 2'-5'-oligoadenylate synthetase and RNase L inpatients hospitalized with West Nile virus infection. J Infect Dis 192: 1741-1748.
336. Bonnevie-Nielsen V, Field LL, Lu S, Zheng DJ, Li M, et al. (2005) Variation in antiviral 2',5'-oligoadenylate synthetase (2'5'AS) enzyme activity is controlled by a single-nucleotide polymorphism at a splice-acceptor site in the OAS1 gene. Am J Hum Genet 76: 623-633.
337. Duronio RJ, Jackson-Machelski E, Heuckeroth RO, Olins PO, Devine CS, et al. (1990) Protein N-myristoylation in Escherichia coli: reconstitution of a eukaryotic protein modification in bacteria. Proc Natl Acad Sci U S A 87: 1506-1510.
338. McKenna SA, Kim I, Puglisi EV, Lindhout DA, Aitken CE, et al. (2007) Purification and characterization of transcribed RNAs using gel filtration chromatography. Nat Protoc 2: 3270-3277.
339. Huth JR, Bewley CA, Jackson BM, Hinnebusch AG, Clore GM, et al. (1997) Design of an expression system for detecting folded protein domains and mapping macromolecular interactions by NMR. Protein Sci 6: 2359-2364.
340. Davis GD, Elisee C, Newham DM, Harrison RG (1999) New fusion protein systems designed to give soluble expression in Escherichia coli. Biotechnol Bioeng 65: 382-388.
341. Hammarstrom M, Hellgren N, van Den Berg S, Berglund H, Hard T (2002) Rapid screening for improved solubility of small human proteins produced as fusion proteins in Escherichia coli. Protein Sci 11: 313-321.
342. Costa S, Almeida A, Castro A, Domingues L (2014) Fusion tags for protein solubility, purification and immunogenicity in Escherichia coli: the novel Fh8 system. Front Microbiol 5: 63.
343. Waugh DS (2005) Making the most of affinity tags. Trends Biotechnol 23: 316-320.
344. Waugh DS (2011) An overview of enzymatic reagents for the removal of affinity tags. Protein Expr Purif 80: 283-293.
345. Sarkar SNP, M.; Sen, G.C. (2005) Assays for the interferon-induced enzyme 2', 5' oligoadenylate synthetases. Methods Mol Med 2: 7.
346. Hassel BA, Ts'o PO (1994) A sensitive assay for the IFN-regulated 2-5A synthetase enzyme. J Virol Methods 50: 323-334.

347. Kuusksalu A, Subbi J, Pehk T, Reintamm T, Muller WE, et al. (1998) Identification of the reaction products of (2'-5')oligoadenylate synthetase in the marine sponge. Eur J Biochem 257: 420-426.
348. Suzuki H, Buonamassa DT (1992) Determination of the level of the core of 2',5'-oligoadenylates by high performance liquid chromatography. Biomed Chromatogr 6: 35-38.
349. Miele MB, Liu DK, Kan NC (1991) Fractionation and characterization of 2',5'-oligoadenylates by polyacrylamide gel electrophoresis: an alternative method for assaying 2',5'-oligoadenylate synthetase. J Interferon Res 11: 33-40.
350. Tong WB, Zhang CY, Feng BF, Tao QM (1998) Establishment of a nonradioactive assay for 2'-5' oligoadenylate synthetase and its application in chronic hepatitis C patients receiving interferon-alpha. World J Gastroenterol 4: 70-73.
351. Justesen J, Kjeldgaard NO (1992) Spectrophotometric pyrophosphate assay of 2',5'-oligoadenylate synthetase. Anal Biochem 207: 90-93.
352. Putnins RF, Yamada EW (1975) Colorimetric determination of inorganic pyrophosphate by a manual or automated method. Anal Biochem 68: 185-195.
353. Berg JMT, J . L . and Stryer, L . Enzymes: Basic Concepts and Kinetics. Biochemistry. New York: W. H. Freeman. pp. 305-320.
354. Segel IH (1976) Enzyme Kinetics. New York: John Wiley & sons.
355. Patel TR, Morris GA, de la Torre JG, Ortega A, Mischnick P, et al. (2008) Molecular flexibility of methylcelluloses of differing degree of substitution by combined sedimentation and viscosity analysis. Macromol Biosci 8: 1108-1115.
356. Dam J, Schuck P (2004) Calculating sedimentation coefficient distributions by direct modeling of sedimentation velocity concentration profiles. Numerical Computer Methods, Pt E 384: 185-212.
357. Schuck P (1998) Sedimentation analysis of noninteracting and self-associating solutes using numerical solutions to the Lamm equation. Biophysical Journal 75: 1503-1512.
358. Laue T (1992) Computer-aided interpretation of analytical sedimentation data for proteins. In: Harding SE, Rowe AJ, Horton JC, editors. Analytical Ultracentrifugation in Biochemistry and Polymer Science: Royal Society of Chemistry. pp. 90-125.
359. Puglisi JD, Tinoco I, Jr. (1989) Absorbance melting curves of RNA. Methods Enzymol 180: 304-325.
360. Berne BJP, R . (2000) Dynamic Light Scattering. New York: Dover publisher.
361. Patel TR, Morris GA, Zwolanek D, Keene DR, Li J, et al. (2010) Nano-structure of the laminin gamma-1 short arm reveals an extended and curved multidomain assembly. Matrix Biol 29: 565-572.
362. Hura GL, Menon AL, Hammel M, Rambo RP, Poole FL, 2nd, et al. (2009) Robust, high-throughput solution structural analyses by small angle X-ray scattering (SAXS). Nat Methods 6: 606-612.

363. Glatter OK, O. (1982) Small Angle X-ray scattering. Academic Press Inc (London) LTD: 14.
364. Putnam CD, Hammel M, Hura GL, Tainer JA (2007) X-ray solution scattering (SAXS) combined with crystallography and computation: defining accurate macromolecular structures, conformations and assemblies in solution. Q Rev Biophys 40: 191-285.
365. Pauw BR (2014) Everything SAXS:small-angle scattering pattern collection and correction. J Phys Condens Matter 26: 239501.
366. Konarev PV, Volkov VV, Sokolova AV, Koch MHJ, Svergun DI (2003) PRIMUS: a Windows PC-based system for small-angle scattering data analysis. Journal of Applied Crystallography 36: 1277-1282.
367. Vachette P, Koch MH, Svergun DI (2003) Looking behind the beamstop: X-ray solution scattering studies of structure and conformational changes of biological macromolecules. Methods Enzymol 374: 584-615.
368. Svergun DI (1999) Restoring low resolution structure of biological macromolecules from solution scattering using simulated annealing (vol 76, pg 2879, 1999). Biophysical Journal 77: 2896-2896.
369. Koch MH, Vachette P, Svergun DI (2003) Small-angle scattering: a view on the properties, structures and structural changes of biological macromolecules in solution. Q Rev Biophys 36: 147-227.
370. Svergun DI (1992) Determination of the Regularization Parameter in Indirect-Transform Methods Using Perceptual Criteria. Journal of Applied Crystallography 25: 495-503.
371. Schnablegger HS, Y. (2011) The SAXS Guide. Austria: Anton Paar GmbH. 98 p.
372. Franke D, Svergun DI (2009) DAMMIF, a program for rapid ab-initio shape determination in small-angle scattering. Journal of Applied Crystallography 42: 342-346.
373. Kirkpatrick S, Gelatt CD, Jr., Vecchi MP (1983) Optimization by simulated annealing. Science 220: 671-680.
374. Kozin MaS, D. (2001) Automated matching of high- and low-resolution structural models , . J Appl Cryst 34: 9.
375. Petoukhov MV, Svergun DI (2005) Global rigid body modeling of macromolecular complexes against small-angle scattering data. Biophys J 89: 1237-1250.
376. Patel TR, Reuten R, Xiong S, Meier M, Winzor DJ, et al. (2012) Determination of a molecular shape for netrin-4 from hydrodynamic and small angle X-ray scattering measurements. Matrix Biol 31: 135-140.
377. Volkov VV, Svergun DI (2003) Uniqueness of ab initio shape determination in small-angle scattering. Journal of Applied Crystallography 36: 860-864.
378. de la Torre JG, Huertas ML, Carrasco B (2000) Calculation of hydrodynamic properties of globular proteins from their atomic-level structure. Biophysical Journal 78: 719-730.
379. Dzananovic E, Patel TR, Deo S, McEleney K, Stetefeld J, et al. (in press) Recognition of viral RNA stem loops by the tandem double-stranded RNA binding domains of PKR. RNA.

380. Laue TM, Shah BD, Ridgeway TM, Pelletier SL (1992) Computer-aided interpretation of analytical sedimentation data for proteins. In: Harding SE, Rowe AJ, Horton JC, editors. Analytical Ultracentrifugation in Biochemistry and Polymer Science. Cambridge, United Kingdom: Royal Society of Chemistry. pp. 90-125.
381. Gasteiger E HC, Gattiker A, Duvaud S, Wilkins MR, Appel RD, Bairoch A (2005) Protein Identification and Analysis Tools on the ExPASy Server. In: Walker JM, editor. The Proteomics Protocols Handbook: Humana Press. pp. 571-607.
382. Adams PD, Afonine PV, Bunkoczi G, Chen VB, Davis IW, et al. (2010) PHENIX: a comprehensive Python-based system for macromolecular structure solution. Acta Crystallogr D Biol Crystallogr 66: 213-221.
383. Winn MD, Ballard CC, Cowtan KD, Dodson EJ, Emsley P, et al. (2011) Overview of the CCP4 suite and current developments. Acta Crystallogr D Biol Crystallogr 67: 235-242.
384. Bradford MM (1976) A rapid and sensitive method for the quantitation of microgram quantities of protein utilizing the principle of protein-dye binding. Anal Biochem 72: 248-254.
385. Bonifacino JSDA, E.C.; Springer, T.A. (2001) Current protocols in Molecular biology. New York: John Wiley.
386. Schmittgen TD, Livak KJ (2008) Analyzing real-time PCR data by the comparative C(T) method. Nat Protoc 3: 1101-1108.
387. Diamond MS (2009) Mechanisms of evasion of the type I interferon antiviral response by flaviviruses. J Interferon Cytokine Res 29: 521-530.
388. Player MR, Torrence PF (1998) The 2-5A system: modulation of viral and cellular processes through acceleration of RNA degradation. Pharmacol Ther 78: 55-113.
389. Han Y, Whitney G, Donovan J, Korennykh A (2012) Innate Immune Messenger 2-5A Tethers Human RNase L into Active High-Order Complexes. Cell Rep 2: 902-913.
390. Wallner G, Mandl CW, Kunz C, Heinz FX (1995) The flavivirus 3'-noncoding region: extensive size heterogeneity independent of evolutionary relationships among strains of tick-borne encephalitis virus. Virology 213: 169-178.
391. Mandl CW, Holzmann H, Kunz C, Heinz FX (1993) Complete genomic sequence of Powassan virus: evaluation of genetic elements in tick-borne versus mosquito-borne flaviviruses. Virology 194: 173-184.
392. Blackwell JL, Brinton MA (1997) Translation elongation factor-1 alpha interacts with the 3' stem-loop region of West Nile virus genomic RNA. J Virol 71: 6433-6444.
393. You S, Falgout B, Markoff L, Padmanabhan R (2001) In vitro RNA synthesis from exogenous dengue viral RNA templates requires long range interactions between 5'- and 3'-terminal regions that influence RNA structure. J Biol Chem 276: 15581-15591.
394. Deo S, Patel TR, Chojnowski G, Koul A, Dzananovic E, et al. (2015) Characterization of the termini of the West Nile virus genome and their

interactions with the small isoform of the 2' 5'-oligoadenylate synthetase family. J Struct Biol 190: 236-249.